Leakage of ionizing radiation from the nearby galaxy Tololo 1247-232

U. Christoffer Fremling
Department of Astronomy, Stockholm University
SE-106 91 Stockholm, Sweden

Supervisor: Erik Zackrisson

June 6, 2013

ABSTRACT

We present a multiwavelength follow-up study of the star forming galaxy Tol 1247-232. Thus far, Haro 11 and Tol 1247-232 are the only two galaxies in the local universe with measurable Lyman Continuum (LyC) leakage. However, the absolute LyC escape fraction previously calculated for Tol 1247-232 can be improved using the total dust-extinction corrected Hα flux of the galaxy as a measure of the intrinsically produced LyC photons.

We have obtained Hα, Hβ, [OIII]λ5007 narrow band and BVRI broad band imaging with the ESO NTT/EMMI, and J, H, and Ks near infrared broad band imaging with the NOT/NOTCam. We utilise the obtained Hα, and Hβ images to construct a map of the dust absorption in Tol 1247-232. We correct the total Hα flux using the obtained extinction map, and estimate the absolute LyC escape fraction, $f_{esc}^{LyC} \approx 4.9 \pm_{1.1}^{1.2}$ %.

We further show that utilising a resolved extinction map as compared to an average extinction calculated using integrated Hα and Hβ fluxes results in a systematic lowering of the calculated escape fraction. However, in the case of Tol 1247-232 the impact of a resolved extinction map on the calculated f_{esc}^{LyC} is small, and other mechanisms that are more difficult to quantify, such as dust absorption of the intrinsic LyC photons, diminish the potential benefit in accuracy from using a resolved extinction map.

We construct a map of the ionization level in the galaxy using [OIII]λ5007 and Hβ images, confirming the previous placement of the galaxy at the top end of the SFR regime in the Baldwin, Phillips & Terlevich (BPT) diagram, limiting the possible contribution from an AGN. The same level of ionization can be achieved by other strongly ionizing sources, such as a large concentration of Wolf-Rayet stars in the galaxy.

We also present integrated BVRI photometry of Tol 1247-232, and construct B-V, V-R and V-I colour maps. The NIR data, calibrated against previous NIR photometry of Tol 1247-232 in 2MASS, is used to construct V-J, J-H and H-Ks colour maps. All of the obtained integrated colours and colour maps are discussed, and qualitatively compared to spectral synthesis models.

Contents

1. Introduction

This project is focused on investigating the properties of the starburst galaxy Tol 1247-232. This galaxy, and Haro 11 are currently the only two galaxies in the local universe with directly detected Lyman continuum (LyC) photon leakage (Bergvall et al. 2006; Hayes et al. 2007; Leitet et al. 2011; Leitet et al. 2013). LyC photons are photons able to ionize hydrogen, i.e. they have energies equal to or higher than the energy difference of 13.6 eV between the ground state and ionization for the hydrogen atom. In terms of wavelengths, λ, this means that LyC photons have $\lambda \leq 91.2$ nm or 912 Å.

LyC leakage, which refers to the escape of LyC photons of stellar origin from galaxies[1], is currently thought to be the biggest contributing factor to the cosmic reionization in the standard hot Big Bang (ΛCDM) model. In general terms, the cosmic reionization is, after recombination, the second major phase-change of hydrogen in the universe. The reionization starts when the first ionizing sources, see e.g. Wise (2012), appear and begin producing photons capable of ionizing the surrounding medium, and it ends when basically all of the intergalactic medium (IGM) is ionized. The reionization era has been empirically constrained to redshifts between z≈6 to z≈14 (Zahn et al. 2011). See also e.g. Finlator (2012), for a review on the current state of research on the reionization era.

Observationally, it has been shown that ionizing emission from Active Galactic Nuclei (AGNs) is enough to keep the IGM ionized in the local low-z universe, e.g. Cowie et al. (2009). However, already at z > 3, the AGN contribution is unable to account for the observationally inferred ionizing flux required to reproduce the $Ly\alpha$ forest structure in the IGM (Meiksin 2005). Thus, as the redshift surpasses z = 3, other sources for the hydrogen ionizing flux such as LyC leaking galaxies are needed. The needed leakage can be estimated for redshifts relevant to the reionization, and Bunker et al. (2010) show that, if galaxies are the only source of the ionizing photons, the observationally estimated star formation rate density at $z \approx 7-10$ would not produce enough ionizing photons unless the

[1]Note that using this terminology, a galaxy is distinct from an AGN. When we talk about LyC leakage, or escape, from galaxies it is implied that the leaking ionizing photons are solely produced by the stars in the galaxy, and not by some other mechanism, such as an AGN, even if the presence of an AGN could cause a high leakage of ionizing photons. In practice, this means that while studying LyC leakage from galaxies, galaxies with AGN activity are usually excluded.

fraction (f_{esc}^{LyC})[1] of escaping LyC photons compared to the intrinsic LyC flux produced by the stellar population is very high, i.e. over 50%. However, we should note that this value is still up for debate. In a more recent study by Finkelstein et al. (2012) it is found that the observable galaxies at $z \sim 6$ are enough for the reionization of the universe at that redshift if $f_{esc}^{LyC} \sim 20\%$. However, for higher redshifts ($z \sim 7 - 8$) escape fractions over 50% are still needed. Further, Bouwens et al. (2012) argue that low luminosity galaxies play a very important role, and under certain assumptions, a lower escape fraction of 20% could be enough. However, the amount of low luminosity galaxies that are present in the high redshift universe is currently not very accurately constrained.

Direct measurement of LyC leakage, i.e. the flux emitted at $\lambda \leq 912$ A, is not possible for galaxies in the reionization era, due to the dense Lyα forest of neutral hydrogen clumps in the line of sight. It is in fact shown by Bolton & Haehnelt (2013) that observations are constrained to redshifts under z $\sim$ 4 - 5, due to the increasing probability for LyC absorbers in the line of sight. The same conclusion is also reached by Inoue & Iwata (2008). Direct detections of LyC leakage have been made. However, with the exception of Haro 11, and now Tol 1247-232, all of the direct detections have been made in objects at z $\sim$ 3. Perhaps most notably, Shapley et al. (2006) (S06) observe a small sample of Luminous Blue Galaxies (LGBs) at z$\sim$ 3, and show high leakage in around 10% of the galaxies in the sample, resulting in an average escape fraction of LBGs at z = 3 that easily can contribute enough LyC leakage to keep the IGM ionized at that redshift (Cowie et al. 2009). One of the leakers in S06 has been confirmed in a later survey by Iwata et al. (2009), however, null detections on three of the strongest sources previously detected in S06 were also made in the same survey. A range of other LyC detections, and non-detections exist, see Bergvall et al. (2013) for a more comprehensive review of all available f_{esc}^{LyC} data. Still, we should note that possible complications with the z = 3 detections exist. Vanzella et al. (2010) show that approximately one third of the current detections have a 50% probability to be contaminated by foreground objects. Additionally, the recent z $\sim$ 3 survey by Boutsia et al. (2011) show a much lower average escape fraction ($f_{esc}^{LyC} \sim 5\%$) than previous surveys. If this average f_{sec} is taken as the average of all galaxies at z = 3, it would not be enough to keep the IGM ionized. Regardless, the current consensus appears to be that along the two LyC detections (Haro 11, and Tol 1247-232) in the local

[1]Throughout this work we adopt the usage of the *absolute escape fraction*, f_{esc}^{LyC}, defined as the ratio of leaking/observed flux density of LyC photons over the intrinsic LyC flux density produced by the stellar population in the galaxy in question. See also Section 7.2 for a further explanation and definition of f_{esc}^{LyC}.

universe, there indeed does appear to be a number of LyC leaking galaxies at z $\sim$ 3. However, the absolute value for the individual escape fraction of the leaking objects, and the estimated average escape fraction at z $\geq$ 3 is still very uncertain. Further, to explain the reionization, an increasing trend in f_{esc}^{LyC} toward higher redshifts appears to be needed (Cowie et al. 2009; Meiksin 2005; Bunker et al. 2010).

Incidentally, both models (Razoumov & Sommer-Larsen 2007) and the existing observations can be interpreted as exhibiting an increase in f_{esc}^{LyC} toward higher redshifts. A very crude estimate using the data collected in Bergvall et al. (2013) shows an increase in the average value of f_{esc}^{LyC} from $f_{esc}^{LyC} \sim 3\%$ at z $\sim$ 0 to $f_{esc}^{LyC} \sim 20\%$ at z $\sim$ 3. Still, accurately determining the trend depends strongly on obtaining more direct detections of LyC leakage preferably at a wider range of redshifts than what is currently available. In fact, since the only direct detections at z $<$ 3 are the already mentioned galaxies Haro 11, and Tol 1247-232, this follow up study of Tol 1247-232 becomes increasingly important. Assuming that the underlying mechanism through which the LyC escape takes place remains the same with increasing redshift, the study of local galaxies exhibiting LyC escape should provide valuable insight, and could come with implications for tracing the LyC escape of galaxies also towards high redshifts. We briefly discuss the typical model scenario required for LyC to be able to take place in Section 1.1. See also Hayes et al. (2007) for a discussion about the importance of the study of local spatially resolved LyC leaking galaxies.

The detection of leakage in Tol 1247-232 is shown by Leitet et al. (2013) using archival data from the Far Ultraviolet Spectroscopic Explorer (FUSE), and an estimated LyC photon escape fraction (f_{esc}^{LyC}) is calculated by comparing the emitted flux at 900 Å and 1500 Å. However, this method is generally used for galaxies at higher redshifts, and quite a few assumptions about the properties of Tol 1247-232 were also made to arrive at the reported result, $f_{esc}^{LyC} \sim 2.4\%$. Generally the properties of Tol 1247-232 are assumed to be very similar or identical to the properties of the first local LyC leaker, Haro 11, which of course might not be the case.

The main goal of this project is to use the directly measured total Hα flux from Tol 1247-232 to estimate the total ionizing flux produced by the stellar population and recalculate the escape fraction. The method that is used in this work, further described in Section 7.2, was developed by Bergvall et al. (2006), and is well suited for nearby galaxies for which Hα data easily can be obtained. However, an accurate estimate of the total Hα flux requires detailed information about the dust absorption in the galaxy. We have obtained narrow band imaging in Hα and Hβ, allowing us to construct an extinction map

of the galaxy, and subsequently estimate the total Hα flux (see Section 6.2). However, the subsequent conversion from total Hα flux to intrinsic LyC photon production is not trivial. In addition to the Hα emission being affected by the dust in the galaxy, the intrinsic LyC photons can also be absorbed by the dust even before ionizing the neutral hydrogen. This leads to a possible systematic underestimation of the intrinsic LyC flux, unless the effect of the LyC dust absorption is taken into account. We investigate this effect further in Section 7.1 using infrared measurements from IRAS, based on techniques by Inoue et al. (2000) and Hirashita et al. (2003).

We have also obtained [OIII]λ5007 narrow band imaging to map the ionization level in the galaxy, and to confirm the placement of the galaxy in the SFR regime of the Baldwin, Phillips & Terlevich (BPT) diagram. The BPT diagram relates the ionization level in the galaxy measured by the ratio between the [OIII] and Hβ emission lines to the observed metallicity. The BPT diagram and previous work on Tol1247-232 in X-ray and radio frequencies are discussed in Section 8. For possible future SED fitting and analysis we have additionally obtained BVRIHJKs broad band images. We do not perform a complete SED fit here, but instead qualitatively discuss, in Section 9, the measured broad band magnitudes and colours with the help of the Zackrisson et al. (2011) spectral synthesis models. Additionally, a substantial part of this project has consisted of the reduction and calibration of data from ESO NTT/EMMI and NOT/NOTCam, thus Section 3 is fully dedicated to explaining the data reduction procedures.

1.1. A model for LyC leakage

To enable significant leakage of LyC photons, we first need a strong source of said photons. Since we are interested in LyC leakage from the stellar populations in galaxies, we limit ourselves to the stars as the ionizing sources. Further, stellar atmosphere models and evolutionary synthesis show that, to produce cosmologically meaningful amounts of LyC photons in terms of reionization potential, we need large amounts of young, hot and massive stars (Vacca et al. 1996; Robertson et al. 2010). Massive stars are all short lived, and thus we need to focus on galaxies showing strong recent star formation, i.e. starbursts. However, to have actual leakage of the ionizing photons produced by the young and massive stars the photons have to also somehow escape from the galaxy into the intergalactic medium. We will see that this photon escape is not at all a trivial matter.

Consider a simplified galaxy-model consisting of an arbitrary population of stars surrounded by a uniformly distributed neutral hydrogen envelope. Now, eventually, if

the hydrogen envelope is large or dense enough, all of the ionizing radiation produced by the stars will be absorbed in interactions with the surrounding interstellar medium (ISM) consisting of neutral hydrogen. The result of this would be the creation of Strömgren spheres (Strömgren 1939) of ionized hydrogen inside an outer envelope of hydrogen that remains neutral. The size of the Strömgren spheres is balanced by the amount of ionizing photons that are produced by the stellar population, and by the optical depth of the ionizing photons when they interact with the hydrogen envelope. The optical depth can be determined by measuring the column density of HI. Such observations of starburst galaxies show that the column density of HI easily is high enough to prevent any LyC escape provided that the neutral hydrogen is uniformly distributed (Heckman et al. 2001,Bergvall et al. 2006, Grimes et al. 2009). Thus for substantial LyC leakage we need both a starburst galaxy and a non-uniform neutral hydrogen distribution configured such that the ionizing radiation produced by the stars can escape through low density areas or voids in the ISM. This kind of porous ISM model for LyC escape is usually referred to as the picket-fence model (Heckman et al. 2001).

Fortunately, simulations show that feedback effects from massive star formation, as is expected to occur in starburst galaxies, could create the proper conditions (Yajima et al. 2011). A consequence of this kind of leakage model, is that f_{esc}^{LyC} measurements will depend on having holes in the ISM in the direction of the observer. Typically in the detections of f_{esc}^{LyC} at z = 3, only a small percentage (i.e. 10% in S06) show leakage, while the other objects show no leakage at all. This can be interpreted as directly supporting a massive star formation driven picket-fence model.

Starbursts show high flux in ultraviolet and blue wavelengths, as a direct consequence of the young stellar population. Additionally, simulations (Yajima et al. 2011) also show that lower halo masses correlate with higher f_{esc}^{LyC}. Thus, local searches for LyC leakers have generally focused on Blue Compact Galaxies (BCGs). Both Haro 11 and Tol 1247-232 is of this class. Additionally, BCGs also show at least some similarities to galaxies in the early universe. They are small in size, irregular in morphology, and show evidence for strong star formation and low metal content. However, we should note that their evolution is of course in reality very different and much longer than the actual reionization era galaxies.

2. Tol 1247-232

Since we are focused on investigating Tol 1247-232 (full name: TOLOLO 1247-232) we will start by introducing the basic properties of the galaxy. Tol 1247-232 has as already mentioned several peculiarities. Tol 1247-232 is both a LyC (Bergvall et al. 2006) and Lyα (Terlevich et al. 1993) leaker. The galaxy is classified as a starburst (Rosa-González et al. 2002), an HII galaxy (Terlevich et al. 1991), a Blue Compact Galaxy (Bergvall et al. 2006) and a Wolf-Rayet (Schaerer et al. 1999) galaxy. The Wolf-Rayet status of the galaxy is important since the leakage of ionizing LyC photons is thought to be made possible by violent star formation of the most massive stars. We quantify the LyC and Lyα leakage in Section 7, and we find further evidence for the presence of a substantial amount of Wolf-Rayet stars in Section 8 and in Section 9 where we investigate the ionization level and broad band photometry of the galaxy. The location of Tol 1247-232 in the sky, its approximate angular size and basic cosmological information is given by:

RA(2000) = 12 h 50 m 18.9 s

DEC(2000) = -23 h 33 m 58.0 s

Size = 0.3'×0.3'

Redshift = 0.048

Distance[1] = 200 ± 10 Mpc

Previous broad band photometry on the galaxy indicate a V-band magnitude of 15.4 mag. We have performed a new set of BVRI photometric measurements, with he results shown in Table 2. See Section 9 for a further discussion relating to the broad band photometry. We have also performed high resolution JHKs imaging of the galaxy (see again Section 9). Figure 1 shows the galaxy in the broad B-band and J-band photometric filters. Note that the galaxy appears to be orientated in a face-on manner, and also note that it visually appears to be an irregular or possibly a barred spiral since it shows hints of both spiral-arm and bar-like structure.

[1]The value reported here is the co-moving distance estimated from the redshift and a standard flat cosmology with $H_0 = 0.73$ km s^{-1} Mpc^{-1}. The reported error accounts for the impact of the local velocity field on the distance estimate.

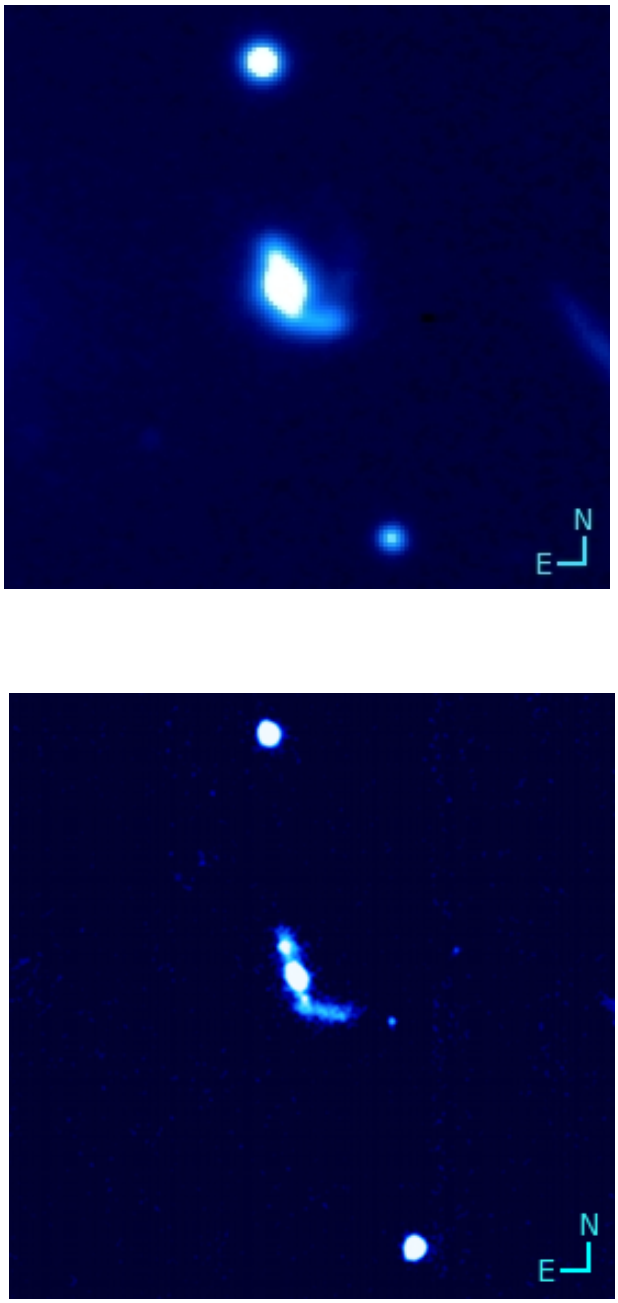

Fig. 1.— Top: B-band optical image of Tol 1247-232. Bottom: J-band near infrared image. The galaxy is centred in the images. Note the spiral-arm like structure seen in both filters.

3. Observations and data reduction

We have performed multiwavelength imaging of Tol 1247-232. Hα, Hα continuum, Hβ, Hβ continuum, [OIII]λ5007 narrow band imaging, BVRI broad band imaging and typical calibration data was obtained using the European Space Agency's New Technology Telescope (ESO NTT/EMMI). The following ESO NTT/EMMI filters were used for the narrow band imaging: #601 for Hα, #768 for Hα continuum, #591 for Hβ, #765 for Hβ continuum, #594 for [OIII]λ5007 and again #765 for [OIII]λ5007 continuum. The photometric standard star field PG 1323 was observed in BVRI, and the calibration star GD 60-54 was observed in the narrow band filters. All of the ESO NTT observations were made in photometric weather conditions using a dithering observation-mode, which amounts to moving the telescope slightly between each exposure, to allow for more robust data reductions. For the object frames on Tol 1247-232, at least 3 exposures for each filter were made.

Additionally, we have obtained J, H, and Ks broad band near infrared (NIR) imaging with the NOTCam on the Nordic Optical Telescope (NOT). The NOT observations were performed by myself by remote controlling the NOT from the remote control facilities at Onsala Space Observatory, in Onsala Sweden. The NIR observations were done in a 9-point dithering pattern to allow for sky background modelling and subtraction. Unfortunately, we were unable to observe a photometric standard calibration field, due to bad weather conditions during most of the observing run. However, the galaxy has previously been observed by 2MASS (Skrutskie et al. 2006), which we will use as a calibration source.

The reductions are carried out using a combination of the MIDAS (Warmels 1992) and IRAF(Tody 1993) image reduction systems. The processing in IRAF is based on various built in low- and high-level procedures. However, a number of self-made IRAF scripts and procedures were also produced to automate parts of the reductions. It is assumed that the reader is familiar, at least with the basics, of astronomical image reduction. We present the reductions performed on the data from the ESO NTT/EMMI in Section 3.1. The NOT/NOTCam NIR data reductions are presented in Section 3.2.

3.1. ESO NTT/EMMI data reduction

Before performing any image processing, we inspect all of the raw data and calibration frames manually. We note that especially in the Hα continuum and in some of the BVRI-band images there is slight bleeding on the target galaxy from a bright nearby star.

However, we always have at least one good frame in each filter. Thus, we have opted to use pixel masking of the affected frames, as opposed to interpolation over the areas affected by the bleeding from the nearby star. In this way we avoid interpolation entirely and can use data that is free of contamination in our subsequent calculations. However the result of this is of course also a slightly reduced signal to noise in a small area of some of the final combined images that we build from the separate dithered exposures. The impact of this is minimal on the final reduced frames, but we should at least note that this problem exists.

3.1.1. General reduction steps

To obtain stacked images from the separate dithered exposures we reduce both the narrow band and broad band data using what is essentially a standard data reduction procedure:

- All frames are initially converted from multi extension *.fits* format into single frame *.fits* files. This is done with a script for MIDAS provided by ESO. The result is images containing a ccd gap in the centre. This gap along with known bad pixels are masked out from all calculations with the help of bad pixel masks also provided by ESO. Any bleeding from nearby bright stars is also manually masked out by creating and editing individual bad pixel masks for each data frame.

- Using the provided calibration dataset we combine around 15 individual bias frames into master-bias frames. The observations were done on different dates, so we create 3 different master-biases, for march 24th, 9 april and 13th april (year 2007). The combining is done by taking the average of the pixel values over the frames, with minmax rejection to reject outliers, and no image scaling. The minmax rejection is configured to reject the single highest and lowest pixel value.

- We combine around 5 dome-flat exposures into a master-flat field frame for each filter. The dome-flats were taken within 24 hours of the corresponding times of the observations on the galaxy. The flat fields are processed by removing the relevant master-bias, and are then combined by taking the median of each pixel, with sigma clipping rejection (3σ) and by scaling the images by the mode. Finally the master-flats are normalized to conserve the image flux by dividing the images by the mode of the images. The ccd gap, and bad pixels are excluded in any mode scaling and normalization calculations.

- We process the object and standard star frames by subtracting the relevant master-bias frame for each image, and by dividing by the relevant master-flat frame.

- We mask cosmic rays from each frame using the laplacian edge detection procedure *LA Cosmic* by van Dokkum (van Dokkum 2001). The results of this step is checked to avoid good data being regarded as cosmic rays in any individual frames.

- We process all of the data frames by dividing by the exposure time and we correct all of the data frames for extinction using the average airmass during the relevant observation. We have constructed a simple procedure to read the average airmass value for each exposure from the .fits headers, and apply a correction factor to normalize the frames to zero airmass. The multiplicative correction factor, C, is computed as

$$C = 10^{\,0.4 \times airmass \times e_c} \tag{1}$$

  where the extinction coefficient, e_c, is obtained by interpolating the data given for the atmospheric extinction at La Silla obtained from ESO, e.g. typically 0.04 mag per airmass for H-alpha. and 0.125 mag for H-beta.

- We align the images by fitting the geometries using around 40 common point sources. This is done via the iraf procedures DAOFIND, GEOMAP, and GEOTRANS. Because of significant rotation (around 1.5 degrees) in the H-alpha-continuum frames we account for rotation, shifting, scaling, and distortion in the geometric mapping. All the GEOMAP fits are inspected to confirm that the residuals of the fits are very small (< 0.05 pixels). GEOTRANS is set to conserve the image fluxes. The fluxes are also manually checked before and after the transformations.

- We fit a low order (order 2 or 3) surface to each individual frame, to make a sky fit and subsequent sky subtraction. The sky fitting is performed using the procedure MSCSKYSUB using object the previously constructed bad pixel masks and additional object masking to exclude all of the stars and objects in the frames during the fitting calculation. The masks for the stars and objects in each frame is created using the procedure OBJMASK. A small IRAF procedure were written to automate this step. However, we still inspect each sky fit and subtraction manually. In some cases we slightly modify the fitting parameters, and repeat the procedure to obtain an optimal sky subtraction.

- The individual exposures are finally combined using the external IRAF procedure IMCOADD. We compare the final image produced by both median and average

combining the individual frames. Regardless of the method of combining we have a low amount of artefacts in the final images. Additionally, since we are using comprehensive bad pixel masking we do not have to utilise any significant pixel rejection during this step, thus we choose the final frames combined using the average of each pixel as our final stacked images in each filter.

3.1.2. Spectrophotometric Calibration of the narrow band images

To calibrate the counts in the combined narrow band images reduced using the above procedure we follow the basic steps below.

- o We first obtain the spectrum for the spectrophotometric standard star G 60-54. This is provided by ESO.
- o We obtain the filter transmission profiles for the filters that were used, also provided by ESO.
- o We convolve the filter profiles with the spectrum of the star. This is done by first interpolating the spectral data to obtain flux values aligned with the data points given for the given filter profile. When the data is aligned we multiply the flux values by the relevant transmission values, to obtain a convolved flux inside the filter.
- o We calculate a theoretical flux (in erg s^{-1} cm^{-2} $Å^{-1}$) from the star in the filter by integrating the convolved flux data according to

$$F_{filter-std} = \frac{\int F_{std}(\lambda) T_{filter}(\lambda)}{\int T_{filter}(\lambda)} \tag{2}$$

- o We perform aperture photometry (see Section 3.1.4) on the standard star images in each filter.
- o We compare the theoretical fluxes calculated as above to the measured counts in our standard star images and record the conversion factors. Note that we have chosen to do this by comparing the theoretical filter flux per wavelength with the measured counts converted to counts per wavelength by dividing by the effective width, EW, of the filter. The effective (box-profile) widths of the filters are calculated by computing the areas of the filter profiles by integration and dividing by the peak transmission values of the filters. All of the filters used display approximate top-hat profile shapes, thus such a box-profile approximation for the effective width should be valid.

- We multiply the narrow band and continuum images by the relevant conversion factors, resulting in calibrated images with the counts given in units of erg s^{-1} cm^{-2}.

- When obtaining isolated emission line images we always subtract[1] the calibrated continuum images from the calibrated narrow-band images by scaling the continuum images to the narrow band images again using the effective widths of the filters such that the flux in each pixel in the line images is calculated according to

$$F_{line} = F_{narrowband} - F_{continuum} \times \frac{EW_{narrowband}}{EW_{continuum}} \quad (3)$$

  However, note that this does not represent the full continuum subtraction procedure that we are using. We perform spectral synthesis model based corrections to our images before the actual continuum subtractions are done. The full emission line isolation procedure is described in Section 4.

- Finally we check where the Hα and Hβ line peaks from the galaxy fall in the filters by accounting for the redshift (z=0.048). In our case the emission line peaks should be located very close to the maximal transmission regions for the filters. Thus, we do not apply any further corrections to our line images.

3.1.3. BVRI photometric calibration

For calibration of the BVRI imaging we have observed the standard field PG1323. This field contains 5 bright standard stars. However, one of the stars is saturated in some of our images, and is thus excluded form the calibration. The calibrations are carried out by measuring the instrumental magnitudes of the four remaining stars, and calculating the zero point for each star in each filter by comparing the instrumental magnitude to the tabulated magnitudes for the standard field:

$$ZP_\lambda = mag_{\lambda_{std}} - log(F_\lambda) + K \quad (4)$$

Where K is an arbitrarily chosen zero point used for calculating the instrumental magnitude. We check for outliers in the calculated zero points, and then calculate the average zero point from the remaining good values. We generally find that the calculated zero points are very stable across the standard star field. Note that we have corrected all of our data to airmass zero before calibration.

---

[1] after aligning and matching the seeing in the images, see Section 3.3.

3.1.4. Photometry on the EMMI/NTT data

For the calibrations and subsequent photometry we use standard aperture photometry. The following apertures were used:

- o For the BVRI photometry of the galaxy we have chosen to use a circular aperture with radius 11", which is typically 33 pixels (pixelscale = 0.332) in our images. We estimate the background in a circular annulus between 37-48 pixels from the galaxy centre. See Figure 2 for an illustration of the aperture that we are using. This choice of apertures for measuring the total BVRI flux from the galaxy is motivated by investigating the curve of growth and surface brightness profiles for the galaxy in the various filters. Typically, the background dominates completely after around 33 pixel radius from the centre of the galaxy.

- o For the Hα, Hβ and [OIII] photometry of the galaxy we use a 11" aperture to measure the total emission line strengths in the galaxy before extinction corrections. The background annulus is chosen in the same way as for the BVRI photometry. However, after the extinction corrections are performed we use a slightly smaller aperture with a 7" radius in addition to a small aperture correction to correct for the missed flux in the smaller aperture. This choice is due to the extinction map that will later be calculated in Section 6.6.1. The extinction cannot be resolved beyond a radius around 7". We base the aperture correction on investigating the individual curves of growth for the galaxy both before and after the extinction corrections are applied. Figure 10 in Section 4 shows a typical curve of growth for the galaxy before the extinction corrections and Figure 4 shows the curve of growth after the extinction corrections that are further explained in in Section 6.7. We find that 99.2% of the flux is included in the 7" aperture, with very minor (less than 0.1%) variations between the three narrow band filters. We see no significant irregularities introduced in the curve of growth by applying the extinction map, and conclude that there should be no problem with using the aperture correction we find before the extinction corrections are made. The corrections are in any case very minor, and any uncertainties introduced will easily be dominated over by the statistical noise in the images.

- o For each standard star measurement we individually investigate the curve of growth, to confirm that the background subtraction is sound, and to find the radius where an estimated 99.9% of the flux is contained. We find that this typically translates to an object aperture radius between 3 to 4 times the FWHM, e.g. $\sim$ 4 times 2.9

pixels in the H-alpha standard star image. The background is generally measured in a circular annulus between approximately 6×FWHM to 9×FWHM. See Figure 3 for an example of the curve of growth in the reduced Hα, filter #601, standard star image. We can see that the total flux is very stable for apertures with radius above ~ 11 pixels or ~ 0.36". It would of course be possible to make a linear fit to the curve for the points somewhere between 11 and 18 pixels to find the intercept at zero, which would then give a robust estimate for the total flux. However, we find that this is unnecessary since our background-subtractions appear to have been very successful. Choosing a single aperture with an appropriate radius, i.e. 12 pixel for filter # 601, gives results that are virtually indistinguishable especially if the inherent statistical uncertainty due to poisson noise in our images is taken into account. Varying the aperture between 12-16" changes the measurement by less than 0.2%. There are only minor differences in the curve of growth between the various standard star narrow band images, and only small adjustments to the apertures are made. Figure 3 can be considered representative.

3.2. NOTCam reductions

To reduce the NIR data from NOTCam we follow the following procedure:

- We inspect the raw data frames. We have chosen to exclude the first frame of the observation run, (the first of the 9 J-band images). This frame shows higher noise, and the mode of the frame is very different from the other frames. This was probably due to the array not yet being stabilised from adjusting the pointing of the telescope to the object.

- Normalized differential flat fields were made by the staff at NOT during our observation run. We utilise these to flat-field our data, now consisting of 8 or 9 frames in each filter.

- After flat fielding, our frames contain both dark and sky contributions. To subtract these contributions from our frames we construct a sky model by median combining the frames using sigma clipping, without aligning the frames. This gives us a sky model that does not contain any objects. Before combining, the frames were scaled to each other by using the midpoint calculated with the IRAF task IMSTATISTICS.

- The sky model frame is subtracted from each individual object frame, again after scaling the sky frame to the sky in the individual images.

- o The sky subtracted frames are inspected, and finally aligned (using the IRAF task IMALIGN) and combined using the median of each pixel with minmax rejection configured to reject the lowest and highest pixel values for each pixel.

3.2.1. Photometric calibration

We calibrate the reduced J, H and Ks images using data on the galaxy available in 2MASS. The procedure to do this is identical to the calibration of the BVRI images above in Section 3.1.3, except that in this case the galaxy itself can be used as the standard. All we need to do is to find the total counts from the galaxy in each of our filters, and subsequently find the zero points which gives us magnitudes that match the values in 2MASS. However, because of the considerable background noise in the images due to their NIR nature, we take extra precautions when choosing the background annulus and apertures used to find the total counts from the galaxy in each filter.

To find the total counts from the galaxy in the images we perform photometry using apertures ranging between 3 to 14 arc seconds in radius, and investigate the stability of the measurements. We find that, if the sky fitting and subtraction has been properly done and the background annulus is chosen in a region where the background is uniform and not contaminated by other objects or artefacts, the flux measurements stabilise and appear roughly constant for apertures larger than approximately 6 arc seconds. However, the point where the sky completely dominates the flux measurements will of course slightly vary between the filters. Thus, to obtain robust estimates of the total counts in each filter we use the average of a series of measurements in apertures between 6 to 10 arc seconds as the final estimate of the total counts from the galaxy. The total counts are then used to find the zero points based on the magnitudes given in 2MASS.

3.3. Pixel scale matching, PSF matching and image alignment of the final calibrated images

To enable calculations involving images from different filters and detectors we estimate the seeing in all of the broad and narrow band images by measuring the Full Width Half Maximum (FWHM) of several point sources close to Tol 1247-232 in the images. If we approximate the Point Spread Function (PSF) in our images with symmetrical gaussians we can match the PSFs in our images by convolving them accordingly. The width of a

gaussian that matches the seeing in an image can be approximated by

$$\sigma_\lambda = \frac{FWHM_\lambda}{2.35} \tag{5}$$

where $FWHM_\lambda$ is a measured FWHM. Now if two images have differing FWHMs we can convolve the image with the smaller FWHM with a gaussian to increase the FWHM in the image. To achieve matching FWHMs we can calculate the difference in the width of the PSFs that are approximated by gaussians according to

$$FWHM_\lambda = \sqrt{FWHM^2_{worst} - FWHM^2_{\lambda_{avg}}} \tag{6}$$

where $FWHM_{\lambda_{worst}}$ is the FWHM in the image with the worst seeing and $FWHM_{\lambda_{avg}}$ is the average of the FWHMs measured in each filter. Eq. 6 combined with Eq. 5 then gives the proper width of the gaussian to use for the convolution of the image with the better seeing.

Further, we also match the pixel scales and alignment of the calibrated images using standard IRAF procedures (GEOMAP and GEOTRANS). It is required to account for rotation, shifting, and scaling to adequately match our images in order to be able to perform continuum subtractions for the narrow band imaging and to construct colour maps using the calibrated broad band images.

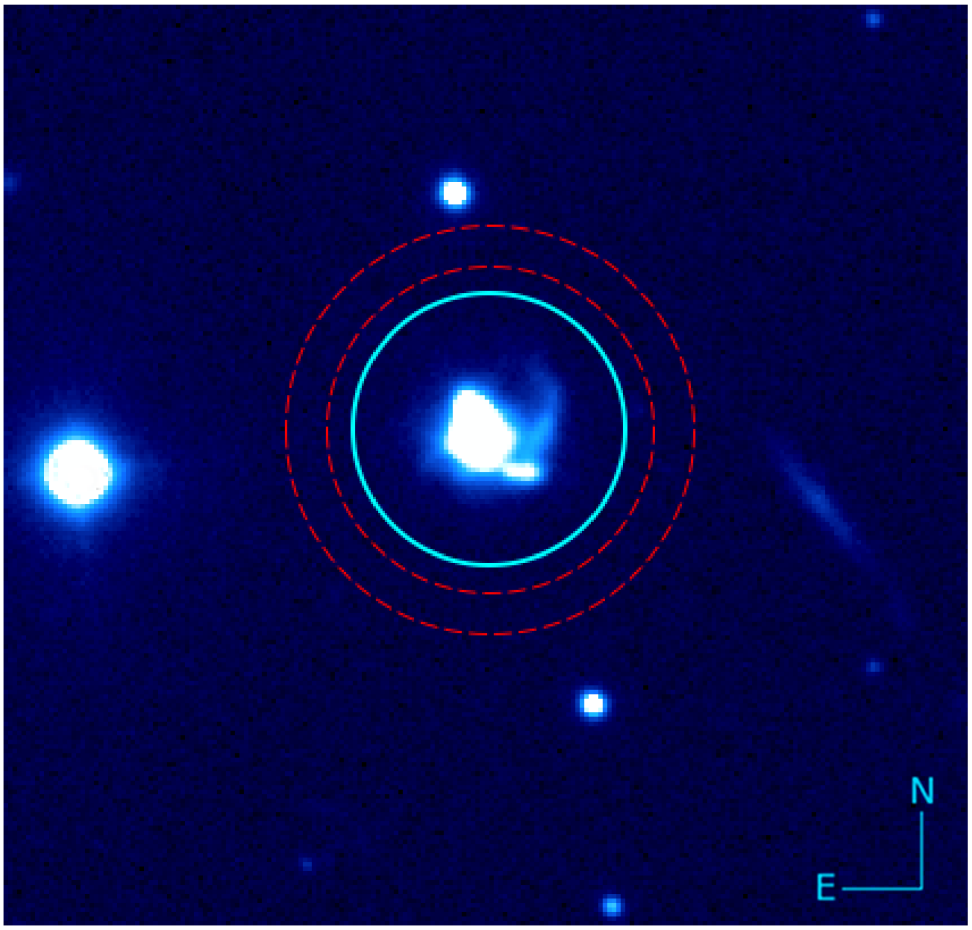

Fig. 2.— Tol 1247-232 in the Hα #601 narrow band filter. The cyan circle shows the photometric aperture (11") that we are using, and the red circles show the background annulus (13" to 15"). Note that light from the star in the upper part of the image becomes significant after approximately 16" radius from the galaxy centre.

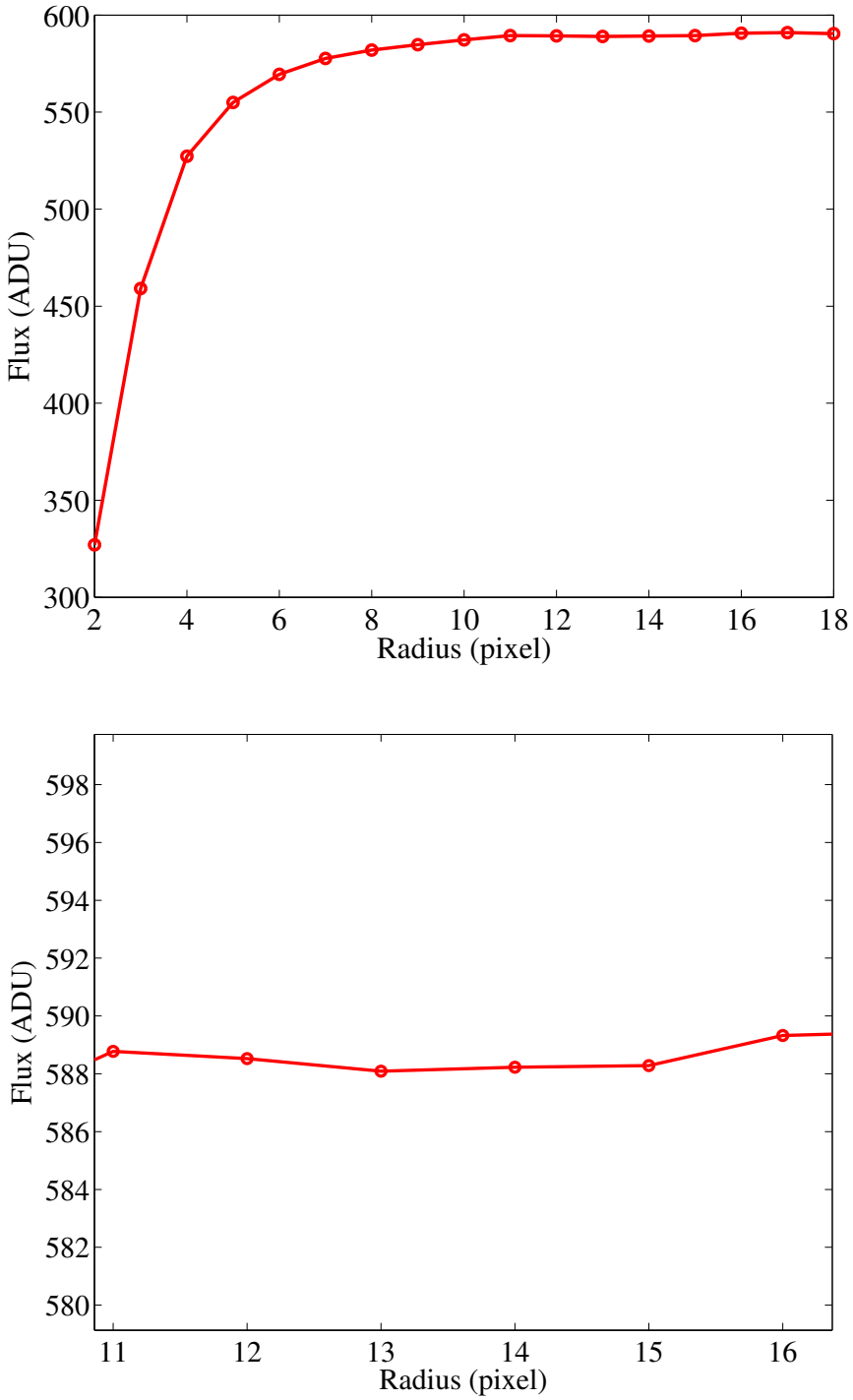

Fig. 3.— Top: Curve of growth for the reduced photometric standard star image in the Hα filter, filter #601. Bottom: Detailed growth curve between 12-16 pixels.

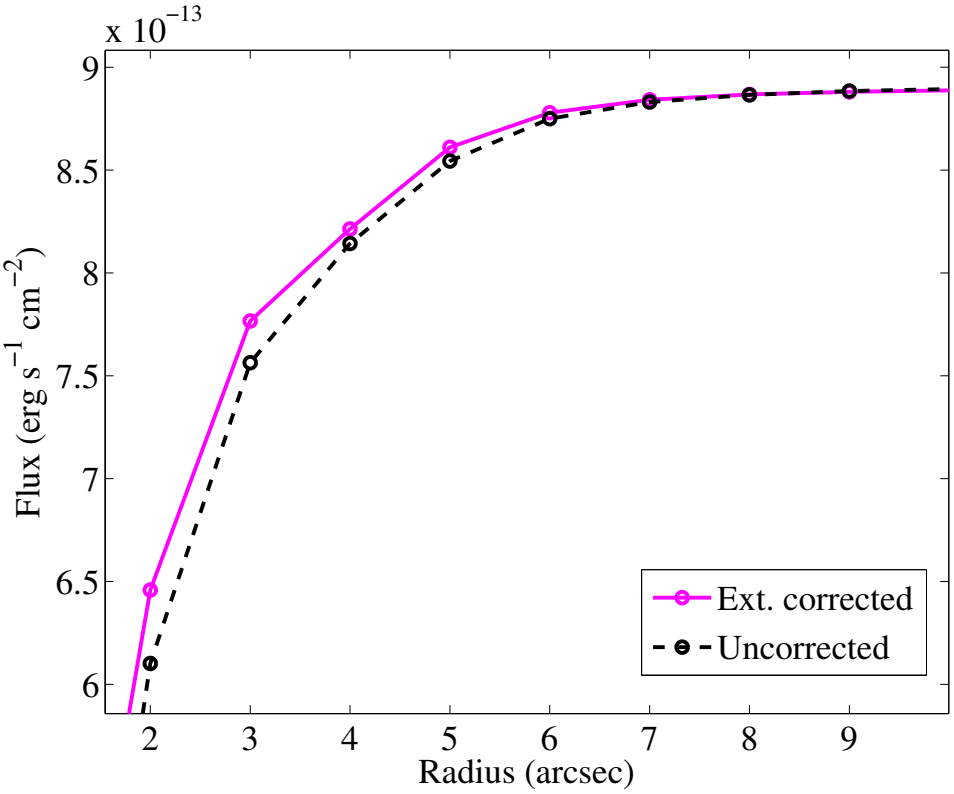

Fig. 4.— Curve of growth of the galaxy in the Hα emission line image after correction using the resolved extinction map calculated using the extinction law for the Milky Way by Fitzpatrick (1999). The dashed black line is the uncorrected growth curve scaled to match the extinction corrected curve at 10" radius.

4. Isolating the Hα, Hβ and [OIII] lines.

We have obtained flux calibrated (see Section 3) narrow band images of Tol 1247-232 using filters centered on the redshifted wavelengths of the Hα, Hβ and [OIII] (5007 Å) lines. However, the fluxes recorded in the calibrated images obtained using these filters do not solely originate from the relevant emission lines. In addition to the wanted emission-line fluxes, each filter also contains continuum-emission originating both from the stars and the gas in the galaxy. To account for this continuum images need to be subtracted. Such images were of course obtained in connection to the line-images. However, the filters used to obtain the continuum images need to be chosen such that no strong emission lines are present, which naturally leads to the continuums being measured at different wavelengths than that of the relevant emission line for which the continuum will later be used. This means that significant over or underestimation of the continuum level at the wavelength of the emission line is possible if there is a significant slope in the continuum of the emitted spectrum of the galaxy. Additionally, even if the filters are chosen very carefully, there will almost always be at least some contamination from other emission-lines in each filter.

To account for the possible general slope in the continuum and to remove significant contamination from other lines we use the spectral synthesis code Yggdrasil (Zackrisson et al. 2011) with stellar spectra from Starburst99 (SB99) by Leitherer et al. (1999). Yggdrasil is used to calculate model spectra for a model starburst galaxy undergoing constant star formation with a duration of 100 Myr. This kind of model which assumes a constant Star Formation Rate (SFR) with a specific duration is usually referred to as a short-burst model, and is appropriate as a model for galaxies undergoing strong star formation where the emission lines are dominated by the massive young stars that are constantly being formed. However, we should note that in reality it is expected that the SFR history of a starburst galaxy is more stochastic in nature (Östlin et al. 2003). See also Figure 5 for an illustration. In this kind of scenario we expect the galaxy to undergo a series of short bursts of star formation instead of a constant continuous episode. Regardless, a constant SFR short-burst model is still useful, since the constant SFR can be considered as an average of the underlying stochastic process as long as the timescales are considerably shorter for the stochastic variations than the timescale that the average is calculated over. The timescales for the variations shown in Figure 5 should not be considered very physical, it is merely an illustration. However, Östlin et al. (2003) show that variations on similarly short, and even shorter timescales appear to be possible. The modelled spectra that emerge from the spectral synthesis model are subsequently used to find the line strengths of all significant emission lines that lie inside the narrowband ESO

NTT/EMMI filters, and to estimate the difference in the continuum levels between the various line and continuum filters[1]. This can of course be done as a function of time since the burst was initiated, and we will henceforth refer to the time since the initiation of the burst in the model as the modelled age. What remains is choosing the proper age or age range to use for the treatment of our actual imaging data.

The results of the Yggdrasil model is shown in Figure 6 for ages (i.e. time since the initiation of the burst) between 1 Myr to 1 Gyr. The top left panel shows the relative contribution from the Hα, Hβ and [OIII] lines to their respective EMMI filters (#601 for Hα, #591 for Hβ and #594 for [OIII]). Note that in this model, for ages above 10^8 years, the modelled emission line contributions to the filters drops off drastically. This is because the formation of new stars is set to cease after this point, which leads to a sharp drop in the nebular emission lines since mostly old stars, contributing mainly to the continuum emission, is left alive after this point. Thus, the top left panel in Figure 1 shows that the impact of any older underlying stellar populations will be minimal on the emission lines that we are interested in. Further, earlier work by Terlevich et al. (1991) shows that Tol 1247-232 has strong emission in both Hα and Hβ. The Hα emission line strength is related to the Star Formation Rate (SFR), and the data in Terlevich et al. (1991) can be translated to an SFR of 47.4 $M_{\odot} yr^{-1}$ (Rosa-González et al. 2007). This leads to the classification of Tol 1247-232 as a starburst, and thus we can immediately conclude that we do not need to consider ages above 100 Myr in our model. We should clearly restrict ourselves to investigating model ages where star formation is still happening. However, we must still investigate the remaining age range (1 Myr - 100 Myr) in more detail. We will do this by first calculating the proper corrections and continuum subtractions to our filters as a function of modelled age, and then investigating the results for the entire age range. The procedure is described below.

The top right panel in Figure 1 shows the contributions from contaminating emission lines in the various filters calculated as a fraction of the total flux in the filters, C_{λ}. The continuum filter used for measuring the Hα continuum is filter #768. For the Hβ and OIII continuum measurements the same filter is used, filter #765. We correct all (both the line filters and the continuum filters) narrow band filter fluxes, F_{λ}, by removing the

[1]This is accomplished by convolving the model spectra with the transmission profiles of the ESO NTT/EMMI filters. This means that we are able to take the actual transmission profiles of the filters into account for all of the continuum and line strength calculations.

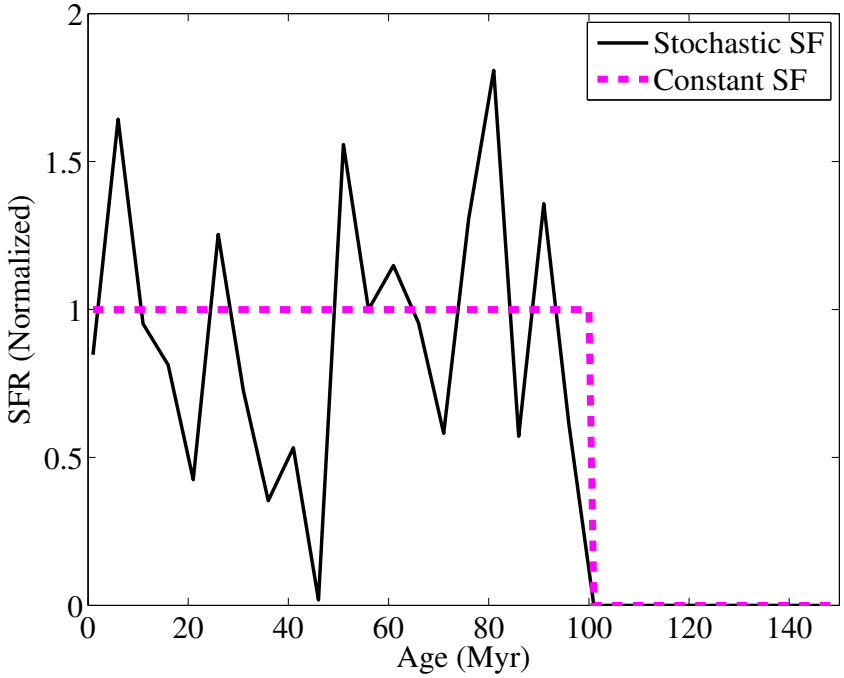

Fig. 5.— An illustration of different star formation scenarios. The magenta coloured line shows a constant burst with a duration of 100 Myr. The black line shows a stochastic scenario that when averaged over 100 Myr would be equivalent to the constant star formation scenario in terms of total amount of stars formed.

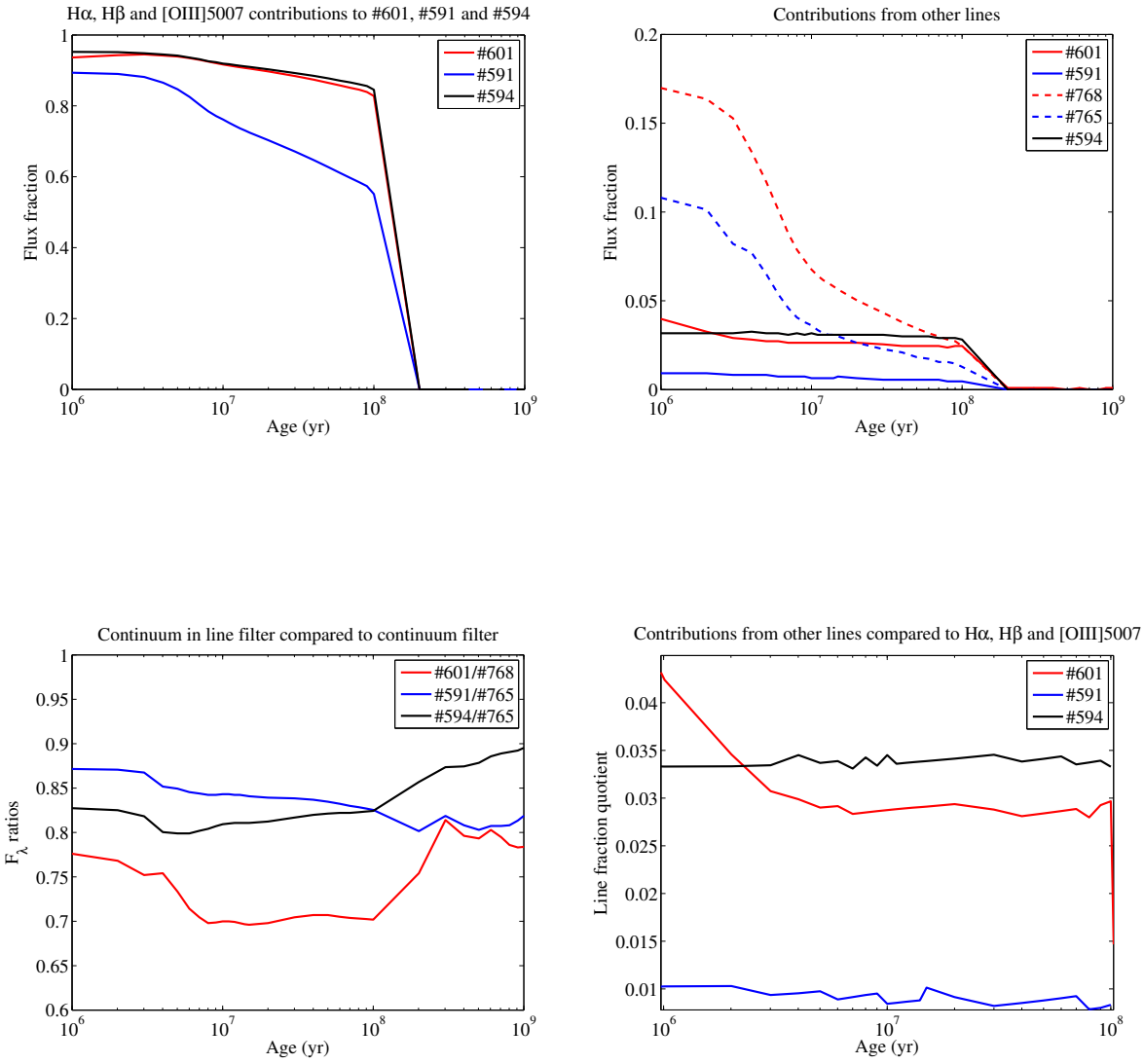

Fig. 6.— Results from convolving the ESO NTT/EMMI filters with the Yggdrasil model spectra. The top left panel shows the relative contribution from the Hα, Hβ and [OIII] lines to their respective filters (#601 for Hα, #591 for Hβ and #594 for [OIII]). The top right panel shows the calculated contribution from other emission lines in the various filters. The continuum filter used for measuring the Hα continuum is filter #768, for the Hβ and OIII continuum measurements the same filter is used, filter #765. The bottom left panel compares the continuum strength in the line and continuum filters. Note that the slope in the spectrum means that the continuum is systematically lower in the line filters than where the actual continuums are being measured. The bottom right panel shows the contribution of other lines relative to the Hα, Hβ and [OIII] line contributions in the line filters.

contaminating line contributions according to:

$$F_\lambda(corr) = (1 - C_\lambda) \times F_\lambda \tag{7}$$

The bottom left panel in Figure 1 compares the continuum strength in the line and continuum filters calculated directly from the Yggdrasil model spectra. Note that the slopes in the model spectra indicates that the continuum is systematically lower in the line filters than where the actual continuums are being measured for all of the filters. We correct the fluxes in our continuum images accordingly:

$$F_\lambda cont.(corr) = F_\lambda(corr) \times F_\lambda ratio \tag{8}$$

The bottom right panel in Figure 1 shows the contribution of other lines relative to the Hα, Hβ and [OIII] line contributions in the line filters. This shows that the effect of contaminating lines is generally very small, i.e. at most 4 %, in the line filters.

Based on the results from the Yggdrasil model above and after applying the relevant corrections to our calibrated line and continuum images we can now perform continuum subtraction (as described in Section 3) of the images to isolate the wanted Hα, Hβ and [OIII] emission lines. This can, as already mentioned, be done for each modelled age, resulting in the isolated line strengths shown in Figure 7. We can see that, except for very young and very old ages, the line strengths appear very stable. For ages between 1 Myr to 100 Myr, the variation in isolated line strength is less than 1.5 % for Hα, less than 2 % for Hβ and less than 1% for [OIII]. These variations are small but not completely insignificant. Thus, we have opted to do most of our calculations based on these images as a function of modelled age. The possibility to constrain the age of the dominating burst more accurately based on our Hα and Hβ imaging data is investigated further in Section 4.1.

We should finally note here that the method to find the corrections above is of course not perfect. We are assuming that it is correct to modify each pixel by the same constant to lower the continuum flux to a proper level for making the continuum subtraction, and it is also assumed that the relative line strengths of the contaminating lines are the same in each pixel across the entire galaxy. Both of these assumptions are of course not necessarily correct. Similarly to the SFR varying as a function of time, as shown in Figure 5, the SFR can of course also vary spatially across the galaxy. To solve this we would need to know the age of the burst in each pixel. However, as already shown, as long as the ages fall between 10 to 100 Myr the effect of the ages being unknown is small (see Figure 7). The validity of our method to isolate the emission lines is explored somewhat further in Section 4.1 and in Section 5.

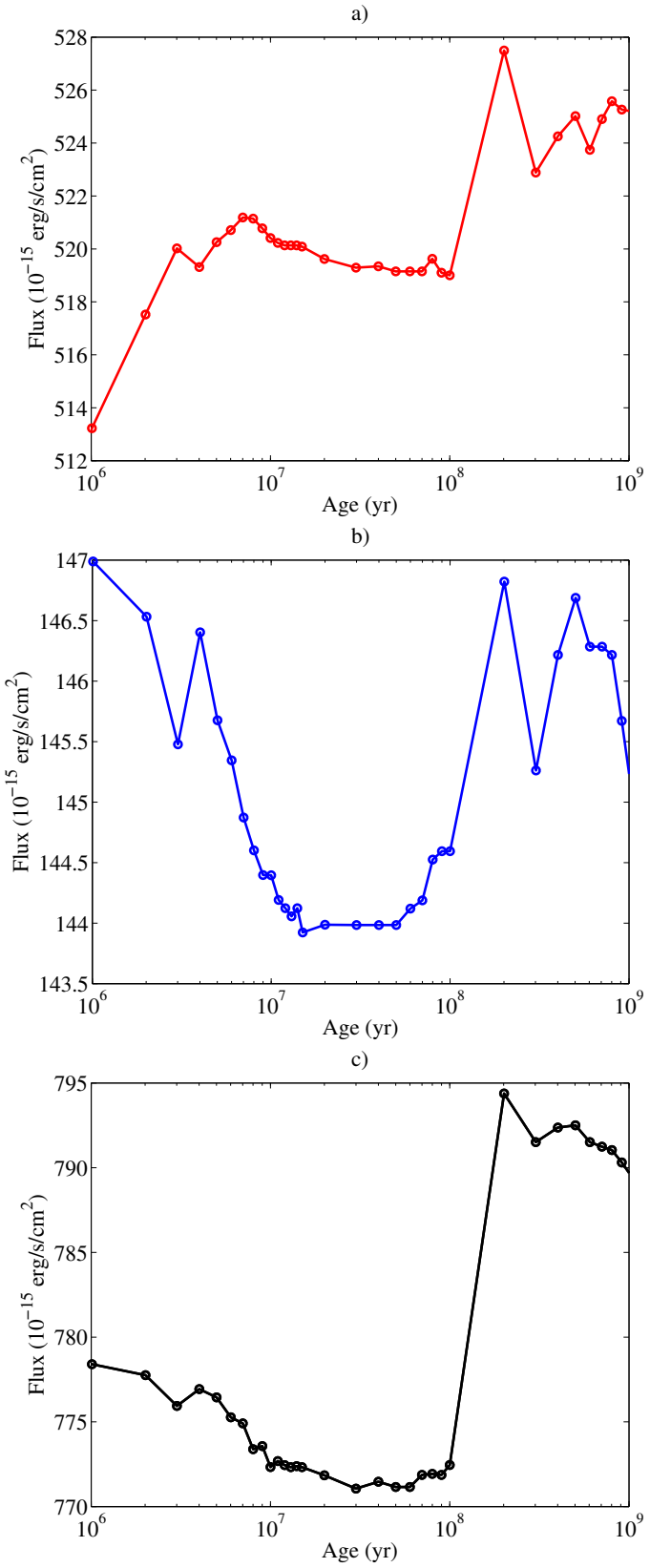

Fig. 7.— Line strengths after continuum subtraction of the a) Hα , b) Hβ and c) [OIII] lines before extinction corrections for modelled ages between 1 Myr and 1 Gyr.

4.1. The age of the dominating burst of star formation in Tol 1247-232

Since we at this point have obtained the isolated line strengths of the Hα, Hβ and [OIII] lines, we can similarly to the top left panel of Figure 1, calculate an empirical (model dependent) relative contribution of the emission lines to their respective filters. This is simply calculated as the relevant isolated line strength divided by the total flux in the matching narrow band filter. The result is shown for the Hα and Hβ lines in panel a) of Figure 3, alongside matching calculations for the Yggdrasil model spectra. Based on this figure we can see that the observed line contributions are expected to occur at quite similar ages for both lines. Further, if we calculate the total difference between the observed flux fractions and the modelled fractions and add the differences for the two lines in quadrature we find that there is a clear minimum at a burst age of 30 Myr, shown in panel b) of Figure 3. Thus, we conclude that the Hα and Hβ emission is dominated by a burst of approximate age 30 Myr. We will not attempt to determine the accuracy or reliability of this result in detail, since we already found in the previous section that any model age between 1 Myr to 100 Myr results in very similar corrections and continuum subtractions. However, we can at least note that if the age calculation is repeated without correcting for the slope of the continuum and without any corrections for contamination from other lines, the result is an age closer to 100 Myr, where the star formation stops. We consider this age determination for the dominating burst less likely, based on the classification of Tol 1247-232 as a starburst galaxy with very strong star formation. However, we must note that this result is at least somewhat model dependent, different input parameters to Yggdrasil might yield slightly different results.

Previous work in X-ray and radio (Rosa-González et al. 2007; Rosa González et al. 2009) indicate that Tol 1247-232 has very recently experienced at least one very strong burst of star formation. However, exactly how recently the burst has happened is more uncertain. Modelling of the equivalent width[1] of Hβ by Rosa-González et al. (2007) indicate that the age of the burst that is dominating the radio emission from Tol 1247-232 is around 4 Myr. This is based on the burst being instantaneous and the measurement of EW(Hβ)=97Å, for Tol 1247-232 by Terlevich et al. (1991). However, for an ongoing continuous burst model, similar to the model we adopt here the age based on the radio emission and EW(Hβ) can be consistent with the Hα and Hβ line contribution age determination above of 30 Myr. A similar uncertainty in the age determination of the burst

[1]The equivalent width is a measure of the line strength compared to the continuum level. For example EW(Hβ)=$F_{H\beta}$ (erg s^{-1}cm^{-2})/F$_{H\beta continuum}$(erg s^{-1} cm^{-2} Å^{-1}).

exist in the X-ray analysis by Rosa González et al. (2009). However the general X-ray properties are more consistent with the X-ray emission being dominated by a younger ($\leq$ 5 Myr) very young short burst. Spectral fitting of the ultraviolet (UV) spectrum of Tol 1247-232 by Buat et al. (2002) indicate that the UV emission is dominated by an even younger burst than for the X-ray data, perhaps as low as 1 Myr. However a scenario where this burst is continuous with an age of up to 5 Myr cannot be entirely excluded.

In conclusion, we find that considering burst ages younger than 1 Myr appears unnecessary given the observed properties of Tol 1247-232. Further, we find that the age of the dominant burst in the visual regime is very likely less than 100 Myr, and probably close to 30 Myr. However, it is difficult to determine if the burst dominating the X-ray, radio, UV and visual (Hα and Hβ) emission is the same burst, or if it is a result of the SFR being stochastic, as shown in Figure 5. It is possible that different wavelength regimes are dominated by different bursts. For example, if we consider the SFR history for an age of 30 Myr in the illustrative scenario shown in Figure 5. Then we can see that the SFR can be considered roughly as a constant between 1-30 Myr. However, if the stochastic nature is considered in detail, there are two separate strong peaks during this timespan. Such a scenario could be compatible with the youngest (closest to 30 Myr) peak at $\sim$ 25 Myr dominating for example the UV spectrum, where the absolutely youngest stars are in fact expected to dominate, while the average SFR over the full age of 30 Myr would still produce the emission lines we observe. However, this is merely an illustrative example to show that this possibility could exist. We have not performed any real investigation of such a stochastic model scenario as shown in Figure 5. However, note that even for a constant SFR, it is not unexpected that the burst age determined by the UV emission is generally lower than what would be determined from the emission in the visual regime. This is because the UV regime is strongly dominated by the youngest most massive stars, and for a continuous burst there is of course continuous formation of new massive stars. Regardless, it would in reality be very difficult to determine the SFR history of a galaxy with a similar resolution to what is shown in the illustration in Figure 5. Ultimately, since this has not been done, a true consensus about the age of the dominant burst cannot easily be reached. Because of this we will for the most part calculate our results as a function of age for continuous burst ages between 1 Myr to 100 Myr. Still, in some cases it is convenient to choose a specific burst age, such as when showing resolved maps of the emission line strengths (Section 5), or when mapping the extinction in the galaxy (Section 6.6.1). When such a choice is prudent we adopt the age 30 Myr, since this age is directly based on our narrow band imaging data.

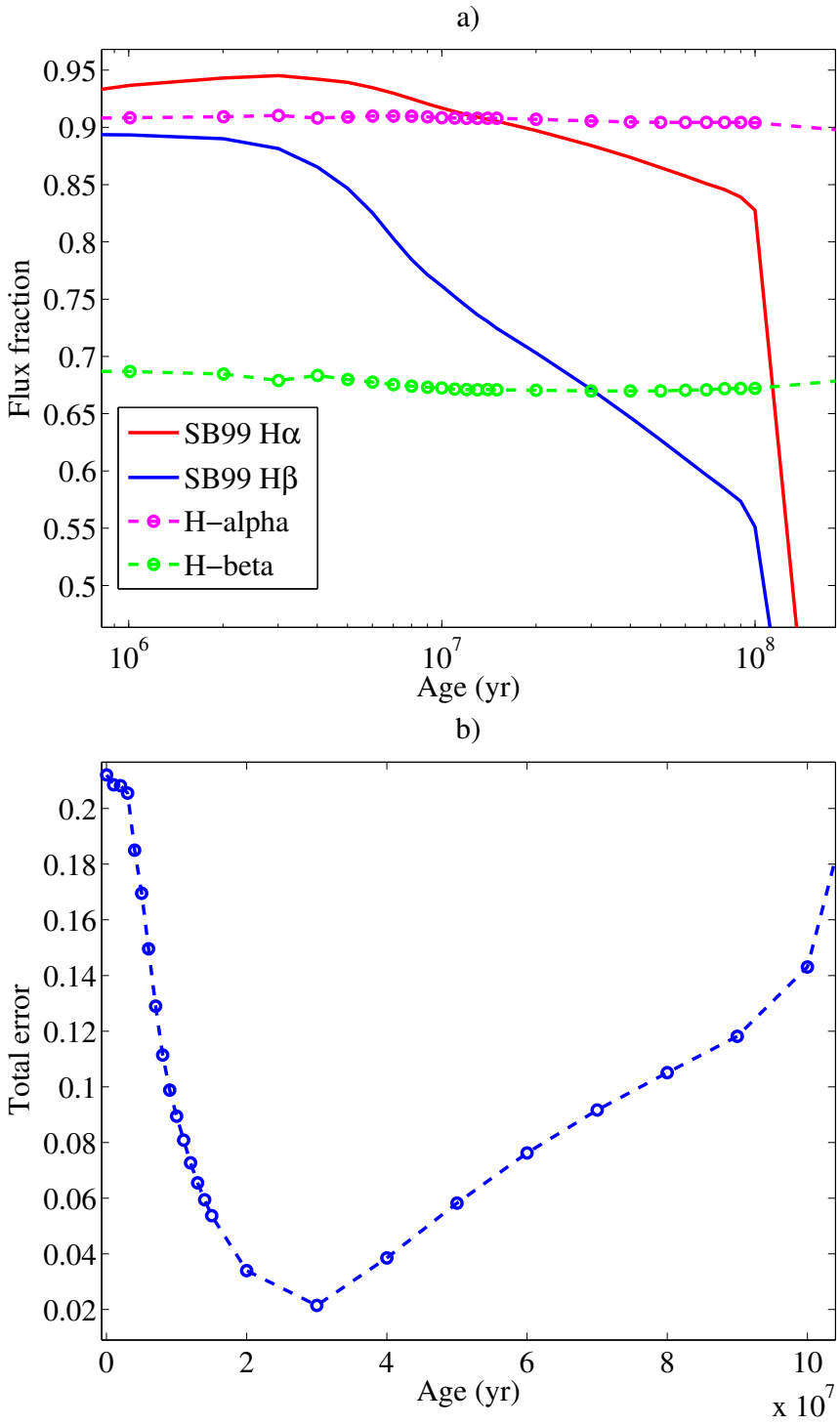

Fig. 8.— Panel a) shows the contribution of the Hα and Hβ lines to the respective filters. The red and blue lines show the purely theoretical Yggdrasil/SB99 model results, and the pink and green data points show calculated contributions based on continuum subtracted line photometry performed as described in Section 4. Panel b) shows the total difference between the model and our model based photometry as a function of modelled age. Note that there is a clear minimum at an age of 30 Myr.

5. Hα and Hβ emission line maps

We present dust attenuated flux density maps of the Hα and Hβ emission lines in Tol 1247-232 in Figure 9. These maps were calculated using an age of 30 Myr for the currently active burst of star formation in the galaxy. By investigating calculated surface brightness profiles and the curve of growth (see Figure 10) of the galaxy in these images we find that regular aperture photometry using circular apertures is adequate to estimate the total emission line fluxes in the galaxy. We find that there are no nearby contaminating objects and that the noise is low enough in our images that we can measure the total emission line fluxes simply by using a large aperture, eliminating the need for any aperture corrections to the total flux estimates. Figure 10 clearly shows that there is virtually no change in the flux for apertures bigger than 11". Note that the rise after 16" is due to the light from another source, see e.g. Figure 2. The purely statistical photon noise will dominate over any uncertainties due to the choice of aperture. The growth curves in the other filters are similar, and the same aperture works for all filters. Thus, we adopt a 11" aperture to measure the total emission line fluxes.

Using a circular aperture with a 11" radius we measure the total Hα flux to 523.3×10^{-15} erg s^{-1} cm^{-2} and the Hβ flux to 145.3×10^{-15} erg s^{-1} cm^{-2}. We find that the uncertainty in our measurements is less than 2%, and that the main source of error is the statistical error due to Poisson noise of the photons (see the following chapters for a full error analysis). Previous spectroscopic data on the total line fluxes by Terlevich et al. (1991) (T91) show Hα = 504.5×10^{-15} erg s^{-1} cm^{-2} and Hβ = 134.9×10^{-15} erg s^{-1} cm^{-2}. Terlevich et al. (1991) estimate an uncertainty of 10% in their line fluxes. Our flux measurements are somewhat higher, but still within the errors given by T91. However, we note that the fluxes by T91 are limited by the smaller aperture (8"x8" square) that was used. We conclude that we are able to improve on the T91 data with new estimates for the total Hα and Hβ emission line fluxes for Tol 1247-232 that should contain all of the flux from the galaxy within the given uncertainties.

5.1. Uncertainties in the line strengths before extinction corrections

The T91 measurements use a square aperture 8" by 8" in size, which is not identical to the circular one we adopt. It is interesting to investigate how our fluxes match those in T91 if we adjust for the aperture difference. By using an identical aperture we find the fluxes, H$\alpha = 497 \times 10^{-15}$ erg s^{-1} cm^{-2} and H$\beta = 137 \times 10^{-15}$ erg s^{-1} cm^{-2}. These fluxes are in extremely good agreement with the data in T91. The Hα flux differs by -1.6% and the Hβ flux differs by $+1.5\%$ compared T91. A similar excellent agreement is also found for the [OIII] line (further discussed in Section 8), which differs by less than 0.1%. After accounting for the noise in our images (see below) our measurements can be considered indistinguishable from those in T91 when identical apertures are used. This result can already be interpreted as showing that there should not be any significant systematic biases or uncertainties in our reductions or calibrations, since the agreement is so good and the T91 measurements use an independent spectroscopic method. However, we will still discuss the most likely possible sources of systematic errors in our isolated line fluxes below.

5.1.1. Uncertainty in the continuum subtraction & line contamination removal procedure

The data in T91 can be used to investigate our continuum subtraction and line contamination removal procedure. If we skip the correction procedure described in Section 4 before performing the continuum subtractions we obtain the isolated line fluxes H$\alpha = 487 \times 10^{-15}$ erg s^{-1} cm^{-2} and H$\beta = 123 \times 10^{-15}$ erg s^{-1} cm^{-2} using an identical aperture as in T91. These fluxes still lie within the errors given by T91. However, the differences between the measurements are now significantly larger, with the Hβ flux approaching a full 10% difference, and both line fluxes being significantly weaker than those in T91. Naively, without systematic biases and errors dominated by poisson noise one would of course expect half of our measurements to lie below those in T91 and half to lie above. This is in fact the case if our correction procedure is used (we found that the Hα line is weaker, while the Hβ line is stronger). Regardless, since we have so few data points, we should perhaps not put too much weight into this reasoning. However, it is still a fact that all our line fluxes are significantly closer to those in T91 when our correction procedure is used. Further, we will later use the isolated Hα and Hβ lines to estimate the extinction in Tol 1247-232 (see Section 6.2), and we have found that calculations that do not utilise the correction recipe in Section 4 tend to result in unreasonable continuum subtractions when the wavelength dependency of the extinction is taken into account when correcting

the various filters. Also, an iterative method to calculate the extinction in Tol 1247-232 is developed in Section 6.4, and we find that it is impossible to use this method on our images of Tol 1247-232 without basing at least the continuum subtractions on the Yggdrasil/SB99 model. Without the corrections the iterative method diverges. We interpret this, the better match with the fluxes in T91, along with the arguably more realistic age determination that can be done when Yggdrasil/SB99 and the recipe in Section 4 is indeed used, as evidence for the validity of the usage of the model based corrections.

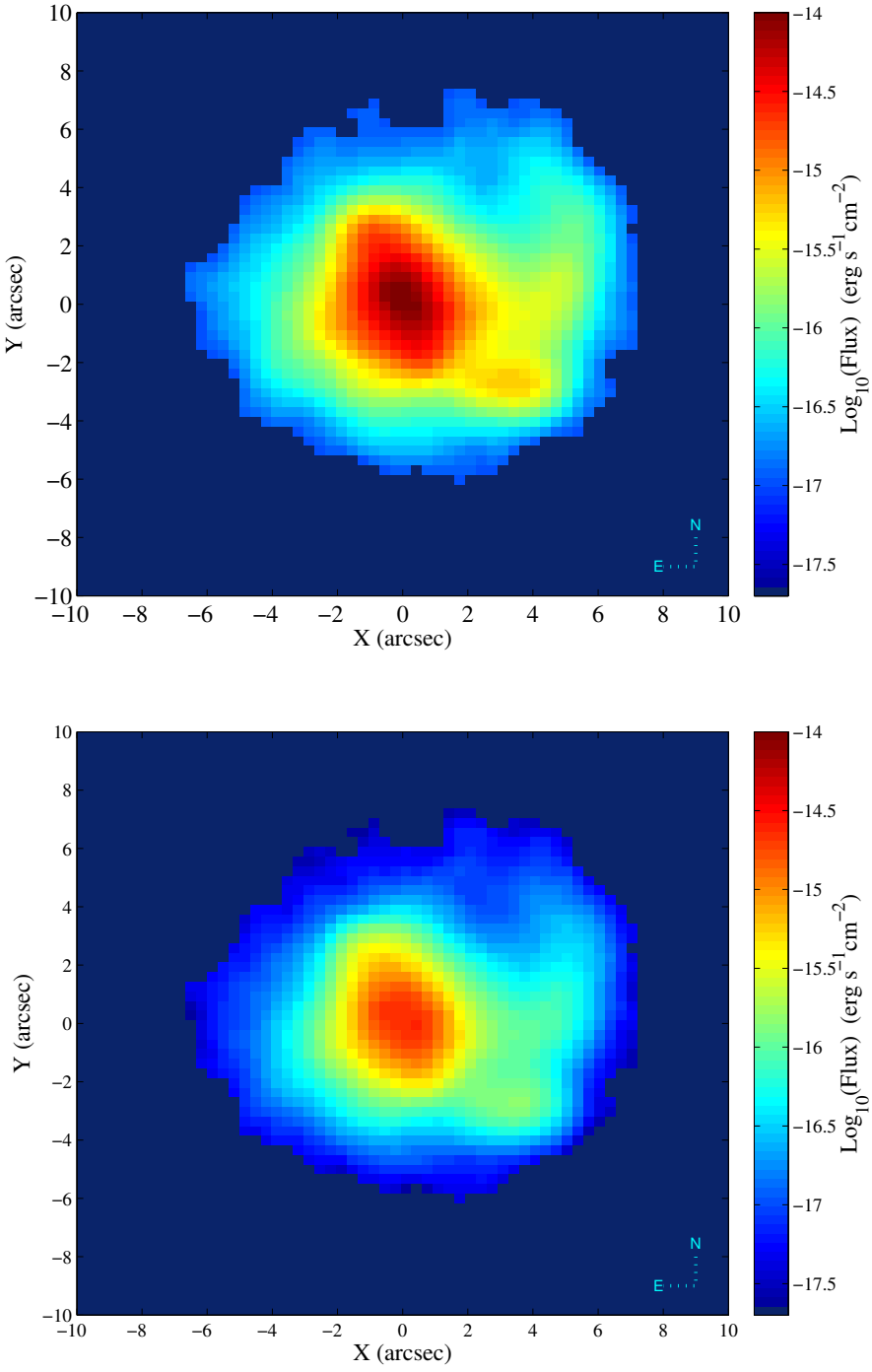

Fig. 9.— Top: Hα map. Log(F_{H_α}), where F_{H_α} is given in units of erg s^{-1} cm^{-2}. Bottom: Hβ map. Log(F_{H_β}), where F_{H_β} is given in units of erg s^{-1} cm^{-2}. These maps are not corrected for any extinction effects.

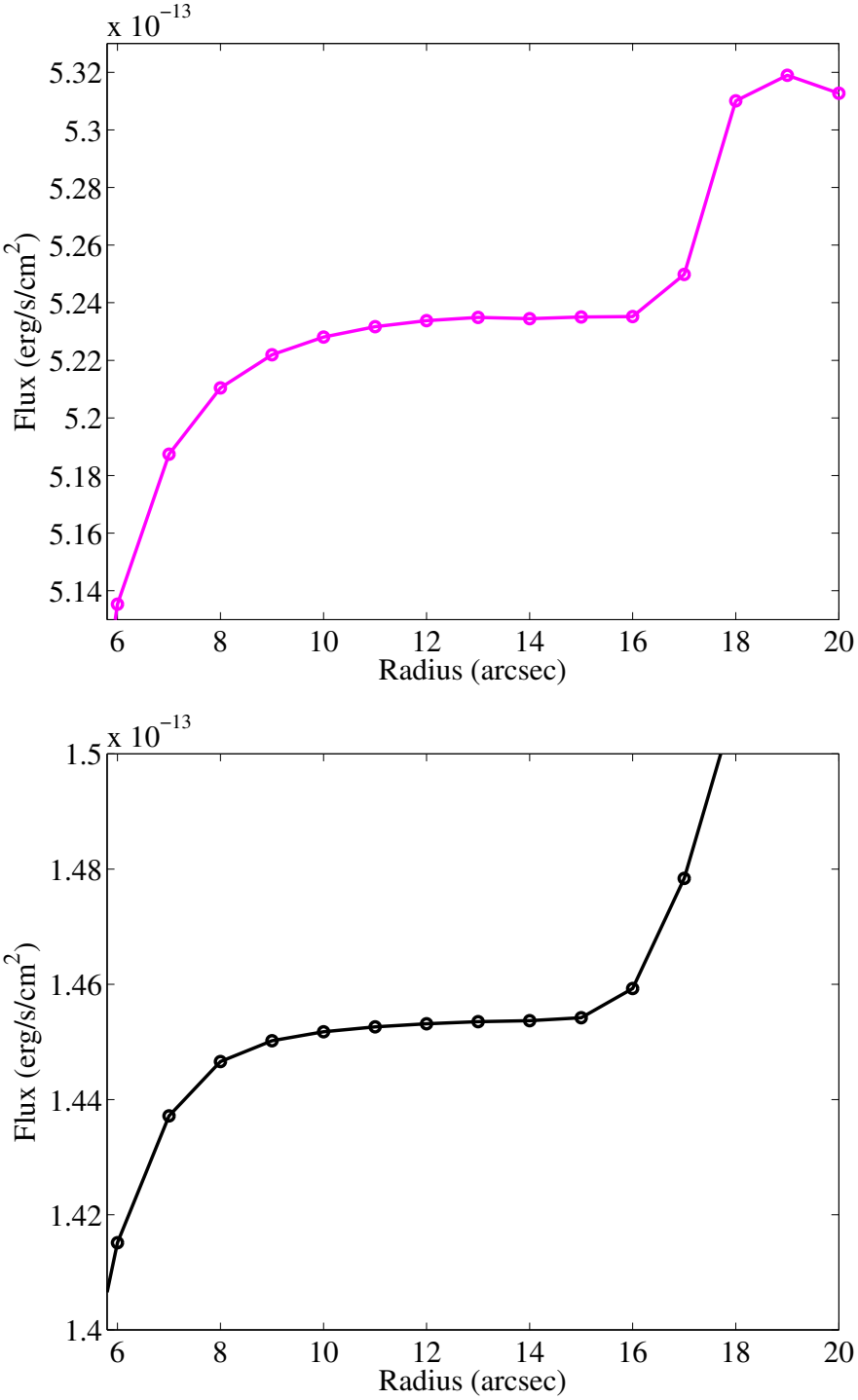

Fig. 10.— Top: Curve of growth of the galaxy in the Hα emission line image after continuum subtraction and contaminating line removal using the Yggdrasil models. Bottom: The curve of growth of Tol 1247-232 in the Hβ emission line image. Note that the bump in flux after 16" radius apertures. After this radius other sources become significant.

5.1.2. Statistical uncertainties

Regardless of how the continuum subtractions are performed and what modelled burst age or age interval is chosen, we also need to consider the inherent statistical poisson noise uncertainties in all of our narrow band images. We will later see that the effect of the statistical errors in our narrow band images on our final best estimate of the escape fraction in Tol 1247-232 (Section 7.2) will be vastly overshadowed by other uncertainties, thus an extremely accurate treatment of the statistical errors is not really needed. However, we will still perform some rough calculations below. Assuming that the CCD gain is close to 1, i.e. if one photon hitting the CCD results in 1 count in 1 pixel of the recorded CCD image, the uncertainty (standard deviation) in each pixel can easily be found as

$$\sigma = \sqrt{N} \tag{9}$$

where N is the recorded counts in the relevant pixel. To quantify the effect of the Poisson noise, basic Monte Carlo (MC) simulations can be used. However, we will first note that the above equation can of course be made more realistic by modifying it to incorporate the true CCD gain and readout noise. But for our purposes, which is merely a rough estimate, the gain can be considered close to 1 (it is really 1.26 for the CCD used), and we can also safely ignore the readout noise, since the counts in our images are generally very high. Now, given that we have an estimate for the standard deviation in each pixel, it is possible to construct *resampled* images of the original flat fielded and bias subtracted narrow band images by applying the per pixel uncertainty randomly for each pixel, resulting in what can be considered a new independent image. If this is done a large number of times and all of the resampled images are passed through the reduction and calibration recipe that we have used, the statistical noise contribution to any emission line measurements can easily be found. The main benefit of this method is that complicated theoretical analysis of how the statistical noise is propagating through the image reduction procedures can be avoided.

We show the result of a MC simulation based on 1000 resampled Hα and H$\alpha_{continuum}$ frames in Figure 11. Note that both the frames containing the galaxy and the standard star is resampled. Also note that this calculation was made prior to accounting for contamination from other lines or the slope in the continuum. However these corrections do not contribute to the statistical noise and are not needed for this analysis. An aperture of 11" was again used throughout all calculations when photometry of the galaxy is necessary. From the calculated distribution in Figure 11 we find that the flux is contained within the range 5.1×10^{-13} erg s^{-1} cm^{-2} to 5.18×10^{-13} erg s^{-1} cm^{-2} with roughly a

95% probability. The mean flux value is 5.14×10^{-13} erg s^{-1} cm^{-2}. This translates to a statistical uncertainty in the isolated Hα line flux of roughly 0.8%. However, since we have ignored the gain and readout noise we will round upwards and use the slightly more liberal statistical uncertainty of 1% for the isolated Hα line. A similar calculation for Hβ yields a slightly higher uncertainty of 2%. Finally for the [OIII] line we find the statistical uncertainty of 1% similar to that of Hα.

Other possible systematic errors

The statistical uncertainties are far from always the dominating source of uncertainty in astronomical images images. Thus, we should also consider some other possible errors, such as systematic errors from the choice of aperture when measuring the fluxes from the galaxy or the standard star, possible flat fielding errors or errors in the sky subtractions performed on our images. We have already discussed the apertures used for the standard stars in Section 3.1.4, where we show that we are able to make very robust measurements of the total fluxes. Any errors due to our choice of standard star apertures will be dominated over by the purely statistical errors. We should also consider the possibility of changing weather conditions during the observation run. However, we have found no evidence for this, and the observations of the photometric standard star were generally made in rapid succession to the observations on the galaxy for each narrow band filter. Thus we see no reason to assume that there would be any problems with applying the calibration calculated from the standard star images on the galaxy images themselves.

5.1.3. Errors due to the choice of aperture for measuring the total flux from the galaxy

We show curves of growth calculated using successively larger circular apertures for the galaxy in the Hα and Hβ filters in Figure 10, a virtually identical curve is found for [OIII]. It is clear from the figures that the quality of our data is very good. The growth curves becomes completely flat after the aperture becomes bigger than 11" in radius. The measured fluxes differ by less than 0.2% for apertures between 11" to 15". This shows that our sky subtraction and flat fielding appears to be excellent at least in the central part of the images where the galaxy resides. After 16" radius the flux from another source becomes significant. However it is clear that there is no more flux to be measured from the galaxy at this point. If we consider the statistical errors of 1-2% we can see that it does not make any sense to debate the choice of aperture.

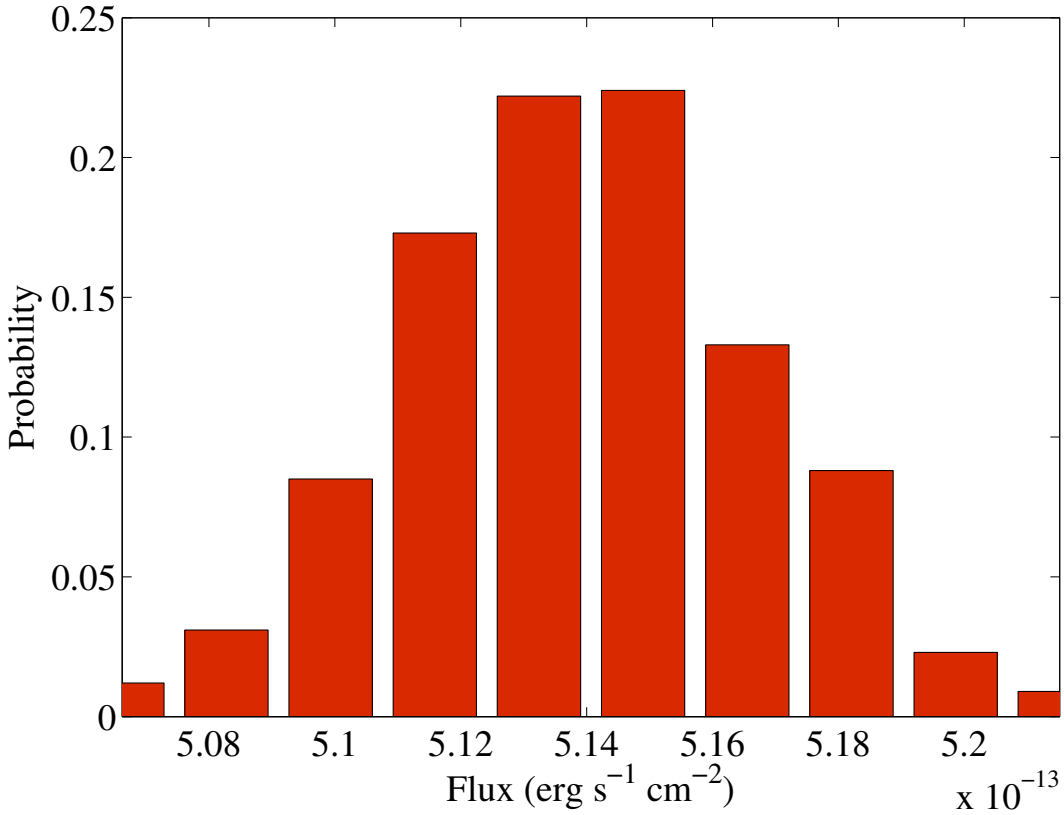

Fig. 11.— A Monte Carlo simulation of the statistical noise contribution to the continuum subtracted Hα line strength. The Yggdrasil model was not used to correct for the slope in the continuum or contaminating lines for this calculation.

5.1.4. Flat fielding, sky subtraction and atmospheric extinction correction errors

The flat fielding error can be up to 2% when dome-flats are used according to the ESO staff. However, considering the nature of our dataset, we do not expect any significant errors due to the flat fielding. This is mainly because we are always just performing photometry on one single object on the CCD, which is either the standard star or the galaxy itself. The maximal flat-fielding error is expected to surface when performing photometry on sources that are either very extended, or widely separated on the CCD. Neither is true for our dataset. We are measuring on a single galaxy, and the galaxy is circular and not very extended (radius $\sim$ 30 pixels). There is typically also a significant possibility of errors introduced by the sky subtraction step of any image reduction procedure. And, we have chosen to account for the atmospheric extinction by using the average airmass for each observation to correct our images, which might not be optimal. However, we have found that all of these errors (flat-fielding, sky-subtraction and atmospheric extinction correction) should be very minimal. This conclusion was made by comparing the cumulative sum of the flux from a number of common point sources across our images before making the final composite image from the separate exposures for each filter. We find that the cumulative flux of around 20 common point sources always vary by 1% or less across the separate frames that are to be combined. We further find that the difference between the separate dithered frames in each filter appears to be randomly distributed, with just as many images differing by $+1\%$ as -1%. All of the common point sources are located in different regions on the CCD in each dithered frame, thus this procedure should be an estimate of the maximal possible errors due to the flat-fielding, sky-subtraction, and our treatment of the atmospheric extinction, since the statistical errors should cancel out when the flux is summed for many objects in the frames. However, since the individual dithered frames show no strong systematic bias in either positive or negative directions, and since the differences between frames appear to be random and within 1%, we conclude that it is possible that we are again seeing just the statistical errors. This could happen if we are summing the flux from too few objects. However, we do not really want to sum flux from objects in areas on the CCD where the galaxy or standard star will never be in any frames. To be on the safe side we will use the full possible 1% systematic error we find here when appropriate in our calculations.

5.1.5. Errors in the chosen effective widths of the narrow band filters

Next we will investigate the possible systematic errors from how we are estimating the effective width of the ESO filters. The effective widths are used in the calibration procedure to convert the total fluxes in the filters to fluxes per wavelength to allow for calibration against the spectrophotometric standard star. The procedure we use to calculate the effective widths is described in described in Section 3.1.2. Note that the procedure is completely automatic and identical for each filter. Basically, the transmission profile of the filter is integrated and divided by the maximal transmission value. The emission lines that are dominating the emission in our line filters are always centred at wavelengths very close to the region of maximal transmission. Thus, we find it very unlikely that there are any significant errors introduced during this step. However, to confirm that the calibrations are not extremely sensitive to possible small errors in the effective widths we preform a simple simulation where we shift the effective width of each of the four filters (Hα line and continuum and Hβ line and continuum) randomly by 0-1 Å and perform the calibrations a large number of times. The result is a standard deviation in the results of 0.3%. We find it unlikely that there is a full 1 Å uncertainty in our determinations of the effective widths, thus we will conclude that this error can be neglected.

5.1.6. Errors from the age of the dominating burst in Tol 1247-232 being unknown

Another possible systematic effect, that we already discussed in Section 4.1, is the fact that we do not know the true age of the dominating burst of star formation in each pixel of our images. However, as we have previously shown, the average age of the burst of star formation that is dominating in the visual regime is probably around 30 Myr. And further, Figure 4 shows that as long as the age of the pixels fall between the age span 10 Myr to 100 Myr, the introduced error is extremely small since the corrections predicted by the Yggdrasil model is virtually identical in this rage. Thus we conclude that any errors from the per pixel age differences should also likely be dominated by the statistical errors already discussed.

5.1.7. Balmer line absorption

Finally we should briefly discuss the possibility for part of the emission lines being absorbed by the stellar continuum. This effect happens because stars can have the Balmer lines (Hα, Hβ, Hγ and so forth) in absorption in their optical spectra. This means that

the nebular emission lines will be superimposed on the absorption lines from the stellar continuum, causing a possible underestimation of the flux. This effect is expected to be negligible if the emission line is very strong, such as typically for Hα in a starburst (González Delgado et al. 1999). However, for the weaker Balmer lines the effect becomes successively more pronounced. It is conceivable that there could be an effect on our Hβ emission line. However, this has already been investigated by Rosa-González et al. (2002), who are able to rule out any significant Balmer absorption in Tol 1247-232 at least for Hα, Hβ and Hγ. This agrees with theoretical spectral evolutionary synthesis (González Delgado et al. 1999) which predicts very small equivalent widths for the absorption lines for ages below 50 Myr in a continuous burst of star formation scenario. Thus we can rather safely ignore this possibility.

Summary of the systematic errors

We find no strong evidence for any systematic errors, such as Balmer line absorption or unusual weather conditions. The only hint at systematic errors we have found are in the estimated total error from the flat-fielding, sky subtraction and atmospheric extinction correction procedures, which we find is less than 1%. However it is difficult to say how much less than 1% the errors introduced by these procedures are, since the statistical uncertainty will contribute to the estimate calculated as above at least to some degree. Combining the statistical and the possible systematic uncertainties we have found in a worst-case configuration results in an estimate of the uncertainty in our measurements of the isolated line strengths of 2-3 % for photometry using a 11" circular aperture on the galaxy. We find it unlikely that the true fluxes before extinction corrections would not lie within these errors, especially since we found our photometry in extremely good agreement with the spectroscopic measurements by Terlevich et al. (1991). Regardless, for our purposes in estimating the escape fraction, the uncertainties in the line strengths are not very critical. We have found that the uncertainty in the measured LyC leakage at $\lambda = 900$ Å, and other effects that are more difficult to quantify, such as LyC absorption on dust in the galaxy will dominate the escape fraction calculation.

6. Extinction for Tol 1247-232

We are ultimately interested in measuring the total emitted Hα flux from the HII regions in Tol 1247-232, since this measurement can be used to estimate the total intrinsic amount of ionizing (LyC) flux produced by the stellar population. The intrinsic LyC photon flux can in turn be used with the measured LyC leakage (Leitet et al. 2013) to estimate the escape fraction of the LyC photons produced by the galaxy. This will later be done in Section 7.2. However, before we are able to do this we must consider the presence of dust.

In Section 4 we have derived maps of the strength of the Hα and Hβ lines in the galaxy. However, these maps do not at all account for the presence of dust particles either in the line of sight towards the galaxy (Galactic extinction) or within the galaxy itself (intrinsic extinction). Subsequently, to find the true emission line strengths we must take both the galactic and intrinsic extinction into account. The Galactic extinction has been experimentally measured for virtually the entire sky (thus also toward Tol 1247-232) and can be conveniently be accounted for in a very straightforward manner. We very briefly explain how wen have chosen to do this in Section 6.1. However, the intrinsic extinction due to dust embedded within Tol 1247-232 itself is slightly more complicated to estimate, but it can still definitely be done. We will, as already mentioned in Section 1, use the observed Hα and Hβ line strengths, since the underlying physics that give rise to these lines are well known. We describe the method used in Section 6.2.

6.1. Galactic extinction towards Tol 1247-232

To account for the galactic dust extinction in the line of sight toward Tol 1247-232 we use the reddening measurements by Schlafly & Finkbeiner (2011). These measurements are based on stellar colour measurements from the Sloan Digital Sky Survey (SDSS; York et al. 2000), and are arguably the most accurate measurements of the Galactic foreground extinction to date. From the dust extinction map constructed by Schlafly & Finkbeiner (2011) we find that the visual extinction, A_v, toward Tol 1247-232 is given by $A_v = 0.237$, measured in magnitudes (mag). This measurement along with an extinction law for the Milky Way can be used to correct our initial calibrated narrow band images. Schlafly & Finkbeiner (2011) suggest that the Fitzpatrick (1999) (F99) extinction law, with the total to selective extinction ratio, $R_v = 3.1$, is preferable. Since the visual extinction and R_v can be considered as known, correcting our calibrated narrow band images for the Galactic extinction is a trivial matter of using the chosen extinction law (F99) to find

the extinction at the relevant central wavelength of each filter, and applying the proper corrections to the fluxes:

$$f_{\rm corr}(\lambda) = f_{\rm obs}(\lambda) \times 10^{0.4 A_\lambda} \tag{10}$$

where $f_{\rm obs}$ is the observed flux before extinction corrections and $f_{\rm corr}$ is the corrected flux.

We should note that this value for the Galactic extinction toward Tol 1247-232 is slightly different to what has previously been calculated by e.g. Schlegel et al. (1998) who show $E(B-V) = 0.089$, or $A_v = 0.27$ given R_V=3.08. The Schlegel et al. (1998) result has been previously used for Tol 1247-232, in e.g. Leitet et al. (2013). However, the higher accuracy in the results by Schlafly & Finkbeiner (2011) is compelling us to adopt the updated value $A_v = 0.237$.

6.2. Mapping the intrinsic extinction in Tol 1247-232

To account for possible attenuation of part of the emission line fluxes by dust particles within Tol 1247-232 we will utilise the observed flux ratios of the (corrected for Galactic foreground extinction) Hα and Hβ recombination lines. This is possible because the Hα and Hβ lines are produced in different transitions of the ionized hydrogen atom, and their intrinsic strengths in a typical HII region can be theoretically calculated by investigating the statistical equilibrium (Osterbrock 1989). The idea is to compare the observed Hα and Hβ line ratios to the theoretical values, assume that the observed difference is due to extinction/reddening, and correct the line fluxes accordingly.

The theoretical ratios between the recombination lines produced by the different hydrogen-atom transitions are commonly referred to as the Balmer decrements (Baker & Menzel 1938). However, the Balmer decrement depends on the conditions of the ionized gas in the nebula where the recombination lines are produced. We assume an electron density of $n_e = 100$ cm^{-3}, which is typical for HII regions (Osterbrock 1989). And we derive the electron temperature, $T_e \approx 12100$K, by investigating the statistical equilibrium and the observed [OIII] emission line ratio,

$$R_{[OIII]} = \frac{[OIII]_{5007\text{Å}} + [OIII]_{4959\text{Å}}}{[OIII]_{4363\text{Å}}} \tag{11}$$

which has been measured spectroscopically in Tol 1247-232 by Terlevich et al. (1993). This temperature calculation is somewhat dependent on the density of the electrons, but we find that modifying the density in the calculations over a large range (30 cm^{-3} to 1000

cm^{-3}) does not alter the result above. Further we will assume a pure Case B recombination approximation, also typical for the conditions in HII regions (Osterbrock 1989). Case B recombination implies that the nebula is optically thick to ionizing photons produced by the ionized hydrogen atoms in recombinations to the ground state. Under these assumptions we derive the theoretical Balmer decrement Hα/Hβ = 2.81, at $T_e \approx 12100$ K for Tol 1247-232. This calculation was performed using the hydrogen recombination-coefficient data in Osterbrock (1989).

Now by comparing the theoretical ratio to the observed ratio, and applying a dust attenuation curve, such as the extinction law for starburst galaxies measured by Calzetti et al. (2000), or the extinction laws for the Milky Way, the Large Magellanic Cloud (LMC) or the Small Magellanic Cloud (SMC) (Fitzpatrick 1999; Gordon et al. 2003; Pei 1992), we can determine the extinction at various wavelengths. Additionally, since we have obtained resolved Hα and Hβ emission line images of Tol 1247-232 we have spatial maps of the line strengths, and can subsequently calculate a spatially resolved extinction map. Typically the extinction is presented as the visual extinction, A_v, to enable easy comparison to other extinction related work. Below we will briefly outline the calculations needed to find A_v as described above. We will adopt a similar formalism as what is used by Calzetti et al. (2000).

6.2.1. Finding Av from the theoretical Hα/Hβ Balmer decrement

Consider the extinction at wavelength λ, A_λ. Assuming that we are working with extinction given in magnitudes as measured by the usual magnitude system, the intrinsic flux is related to the observed flux by

$$f_{\rm int}(\lambda) = f_{\rm obs}(\lambda) \times 10^{0.4 A_\lambda} \tag{12}$$

Now, using some extinction law, given by $k(\lambda)$, the extinction at λ is given by

$$A_\lambda = \frac{k(\lambda) A_V}{R_V} \tag{13}$$

where A_v is the visual extinction, and R_v is the total to selective extinction ratio

$$R_v = \frac{A_V}{E(B-V)} \tag{14}$$

where $E(B-V)$ is the reddening or colour excess:

$$E(B-V) = A_B - A_V = (B-V) - (B-V)_0 \tag{15}$$

where $(B-V)$ is the measured $(B-V)$ colour and $(B-V)_0$ is the intrinsic colour. We can see that if the intrinsic colour of an object is known, the reddening can be measured in this way by simply observing the $(B-V)$ colour. We can also see that the reddening or colour excess can be considered a measure of how much broad band colours will change due to the wavelength dependency of the extinction, while R_V relates the total extinction to the reddening. Most extinction laws in the literature are normalised in some way using these quantities.

We will show the following steps using the specific Calzetti et al. (2000) attenuation law for starbursts, however the procedure will be the same for any extinction/attenuation law presented in a similar way. The extinction law in Calzetti et al. (2000) is given by

$$k(\lambda) = 2.659\left(-2.156 + \frac{1.509}{\lambda} - \frac{0.198}{\lambda^2} + \frac{0.011}{\lambda^3}\right) + R_v \quad \text{for} \quad 0.12\mu\text{m} \leq \lambda \leq 0.63\,\mu\text{m} \quad (16)$$

and

$$k(\lambda) = 2.659\left(-1.857 + \frac{1.040}{\lambda}\right) + R_v \quad \text{for} \quad 0.63\mu\text{m} \leq \lambda \leq 2.20\,\mu\text{m} \quad (17)$$

now using Eq. 12 for Hα and Hβ we get

$$\frac{f_{\text{int}}(H\alpha)}{f_{\text{int}}(H\beta)} = \frac{f_{\text{obs}}(H\alpha) \times 10^{0.4A_{H\alpha}}}{f_{\text{obs}}(H\beta) \times 10^{0.4A_{H\beta}}}$$

Eq. 6.2.1, Eq. 13 and the intrinsic Balmer decrement $\frac{f_{\text{int}}(H\alpha)}{f_{\text{int}}(H\beta)} = 2.81$ solved for the visual extinction A_v gives

$$A_v = \frac{(\log 2.81 - \log \frac{f_{\text{obs}}(H\alpha)}{f_{\text{obs}}(H\beta)})R_v}{0.4(k_{H\alpha} - k_{H\beta})} \quad (18)$$

now by adopting some value for the total to selective extinction, R_v, and using for example the Calzetti et al. (2000) law given above to find $k_{H\alpha}$ and $k_{H_{beta}}$ and our measured line strengths we can calculate A_v. Eq. 18 can subsequently be used to find the extinction in each spatially resolved region or to calculate an average extinction by photometrically measuring the total Hα and Hβ line strengths. Note again that the above procedure, and Eq. 18, can of course be used for any extinction law $k(\lambda)$ as long as the law is given by

$$k(\lambda) = \frac{A_\lambda R_V}{A_V} = A_\lambda / E(B-V) \quad (19)$$

We will later in Sections 6.6.1 and 14 use Eq. 18 to estimate the average extinction and to construct a resolved map of the visual extinction in Tol 1247-232. However, we should first discuss the choice of extinction law(s) and total to selective extinction values (R_v) that we will be using to determine the extinction in Tol 1247-232.

6.3. Adopted extinction laws

We adopt the extinction laws shown in Figure 12, which is the empirical law for the Milky Way (MW) with $R_V = 3.07$ (Fitzpatrick 1999), the empirical extinction laws for the Large Magellanic Cloud (LMC) & Small Magellanic Cloud (SMC) with $R_V = 3.46$ and $R_V = 2.75$ respectively (Gordon et al. 2003), and the already mentioned empirical attenuation law for starbursts by Calzetti et al. (2000), which is shown for $R_V = 4.05$ and $R_V = 3.1$ in the figure.

Tol 1247-232 is a starburst which of course makes it seems natural to prefer the attenuation law for starbursts by Calzetti et al. (2000), and we will do this when correcting the broad band BVRIHJKs images shown in Section 9. However, we should note that the Calzetti et al. (2000) law is specifically developed to correct the integrated stellar continuum emission for reddening in a typical starburst galaxy. It is not as suitable for dealing with Balmer line extinction determinations and nebular emission line attenuation corrections (Calzetti et al. 1994), especially with the suggested $R_v = 4.05$ (Calzetti et al. 2000) for the total to selective extinction, since this value is an average calculated for the integrated continuum emission of a sample of starbursts. Calzetti et al. (2000) and Kreckel et al. (2013) both show that the extinction determined from the Balmer line ratios, and the stellar continuum extinction appear to be different, with the extinction generally being lower for the continuum emission according to:

$$E_s(B-V) = 0.44 E_{HII}(B-V) \tag{20}$$

where $E_s(B-V)$ is the colour excess for the stellar continuum and $E_{HII}(B-V)$ is the colour excess determined from the Balmer line ratios using a standard extinction law for the MW or LMC with $R_V \approx 3.1$. Note that if $R_V = 4.05$ would be used when determining the extinction from the Balmer lines this effect would be even larger. Calzetti et al. (1994) argue that this discrepancy is observed because the Balmer lines are produced in regions very close to the young massive stars that form in dusty regions in the galaxy – while older stars that dominate the stellar continuum emission drift away from these dusty regions over time. Thus it appears that the Calzetti et al. (2000) law with $R_V = 4.05$ should perhaps not be directly used to determine the extinction from the Balmer lines since the law is formulated for the continuum emission. However, the shape of the law, i.e. the wavelength dependency, can still be useful since it is empirically determined for starbursts. We find that using the Calzetti et al. (2000) law to find the extinction via the Balmer lines gives very similar results as for the MW law by Fitzpatrick (1999) if R_V is adjusted to similar values as for the MW or LMC. Note that this is not very

surprising, the bottom panel in Figure 12 clearly shows that all of the laws we adopt show only minor differences in the slope of the extinction-curves between the Hα and Hβ wavelengths. The law that deviates the most from the others is in fact the extinction law for the SMC. Regardless, since we do not in the end know which of these laws is the most applicable for Tol 1247-232 we will, when appropriate, calculate the results in the following sections separately for all of these laws and for a range of R_V values typically between $R_V = 2.75$ to $R_V = 4.85$, since individual galaxies show quite a large variation in the average R_V (Calzetti et al. 2000). Finally, we will note that other work dealing with extragalactic Balmer line based extinction determinations tend to prefer the MW, LMC and Calzetti et al. (2000) laws typically with $R_V \approx 3.1$ (Calzetti et al. 1994; Kreckel et al. 2013; Rosa-González et al. 2002). Thus the results we obtain using these laws could perhaps be considered as preferred. However, before proceeding with any calculations at all we must first consider an important consequence of using photometric filters to determine the extinction from continuum subtracted Hα and Hβ line ratios. Due to the wavelength dependency of the extinction, the corrections will be slightly different for the filter used to measure the line and for the filter used to measure the continuum for the line. Extinction corrections applied separately in this way means that the corrected Hα and Hβ line ratios will no longer necessarily match the theoretical Balmer decrement that was used to calculate the extinction in the first place. To solve this, the extinction can be determined in an iterative fashion, hopefully converging on a stable solution, which retains the Balmer decrement even after the wavelength dependent extinction is applied for the continuum and line filters separately. We describe a simple procedure to accomplish this in the following section.

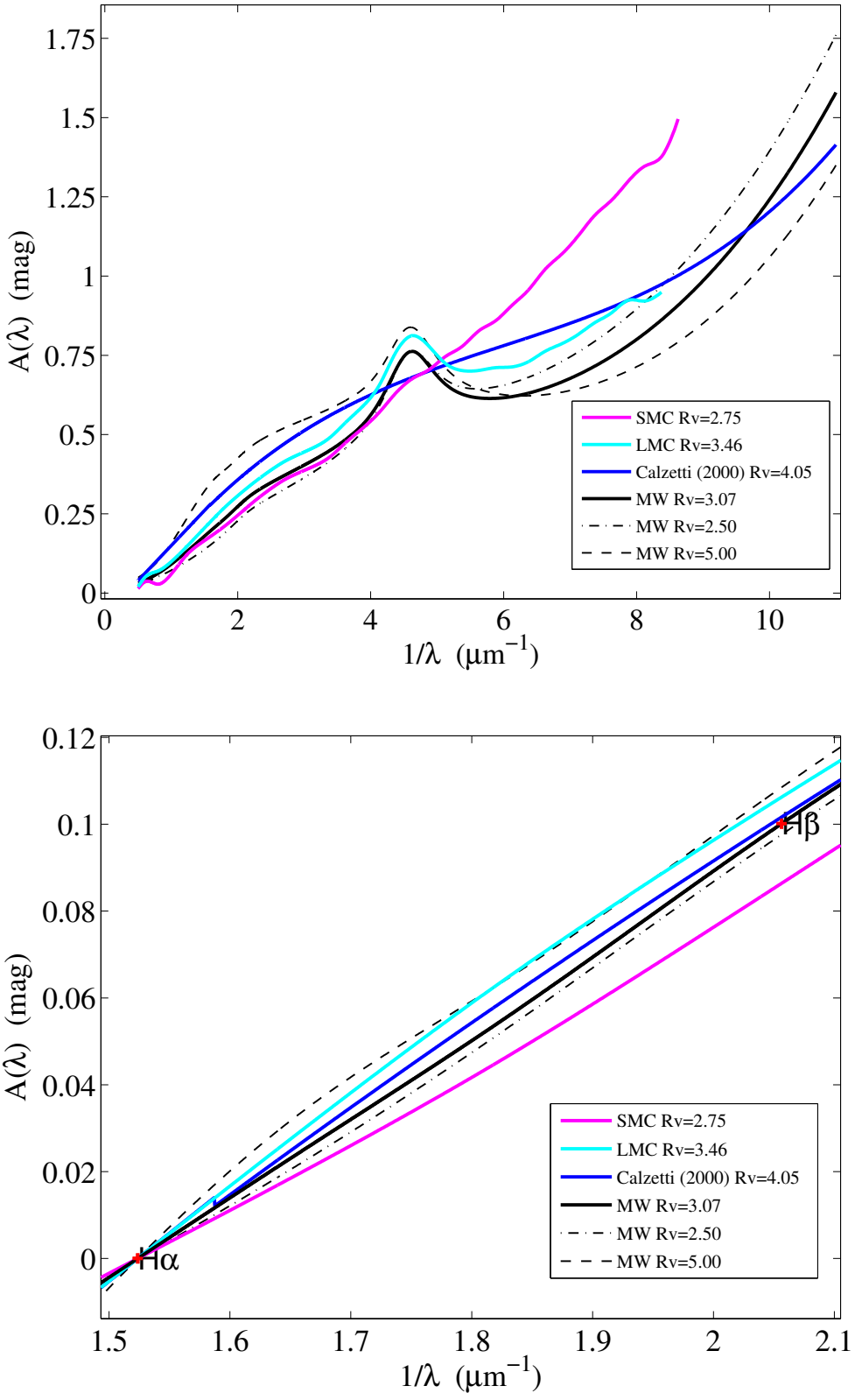

Fig. 12.— Top panel: A(λ) calculated for $E(B-V) \approx 0.08$ for all of the extinction laws that are used for our emission line corrections. Bottom panel: The adopted extinction laws normalised at the wavelength of Hα.

6.4. An iterative method to calculate the extinction

We now consider A_v calculated from the continuum subtracted Hα and Hβ lines as described above (Section 6.2.1) as a first approximation of the extinction, $A_v(i)$. Now if we adopt the calculated $A_v(i)$ and some extinction law along with an estimate for R_V we can apply the extinction to each separate photometric filter using Eq. 13. After this is done we can proceed by redoing the continuum subtractions to find the extinction corrected isolated line strengths. However, since the extinction is wavelength dependent, this correction can cause the line ratio of the Hα and Hβ lines to no longer display the correct Balmer decrement. This can then in turn be interpreted as additional extinction, $A_v(i+1)$. To find this additional extinction the procedure described in Section 6.2.1 can simply be repeated. The total extinction, $A_v(t)$, is then given by adding the initial extinction and the leftover extinction.

$$A_v(t) = A_v(i) + A_v(i+1) \tag{21}$$

now, this can of course be repeated an infinite amount of times by setting

$$A_v(i) = A_v(t) \tag{22}$$

and starting over. However, doing this only makes sense if the extinction calculated after each pass becomes progressively smaller, and eventually approaches zero. Thus, the validity of this procedure needs to be investigated.

Fortunately, we find that generally, at least in the particular case of our narrow band dataset here, the procedure does converge rather rapidly. In fact, if an A_v map is calculated for each modelled age of the galaxy, we find that the calculated iterative A_v appears stable already after 3 or at most 4 iterations. However, this is only true if the emission-line isolation procedure based on the Yggdrasil model, as described in Section 4 is used. If this is not done, i.e. the emission lines are isolated by directly performing the continuum subtractions without applying any model based corrections, we find that the iterative extinction calculations give unreasonable results, with parts of the extinction in the calculated A_v map approaching infinity. We further find that this is due to the continuum levels being too high resulting in negative flux values after subtraction in certain regions of especially the Hβ image. This translates to the iterative method not being able to reasonably converge. We interpret this as even further support for the need of the line-isolation procedure described in Section 4, since the model shows that the continuum is generally overestimated without corrections. The difference between using the first-pass extinction calculation and the iterative method is further explored in Section

6.6.1. Nevertheless, we have to admit that it is not trivial to determine if this iterative method really is always correct. However, to confirm that the method at least does not converge on completely unreasonably solutions we have constructed a simple simulation.

We start with a set of images in the four filters, Hα, H$\alpha_{continuum}$, Hβ and H$\beta_{continuum}$, such that each pixel shows the theoretical blamer decrement $\frac{H\alpha}{H\beta}_{T_e=12100K} = 2.81$ in an image showing the ratio of the continuum subtracted Hα to the continuum subtracted Hβ line. Note that such an image set does in fact naturally emerge from running the iterative method above. Thus, we will use our actual extinction corrected images for the following calculations. However, note that we could just as well generate the images for use in the simulation artificially, as long as they adhere to the chosen Balmer decrement (here 2.81) after the continuum subtractions are done. Regardless, after obtaining a proper set of images, we can apply an arbitrary extinction on the images, by constructing a randomised extinction map. The result of this is dust attenuated images in the four different filters. Now, if we run the dust attenuated images through the iterative method explained above to find the resolved extinction, we can see if our method successfully reproduces the same randomised extinction map that was used to construct the dust attenuated images in the first place. We show the result of such a simulation in Figure 13. The top left panel shows the randomised extinction map used to apply the extinction. The top right panel shows the iteratively calculated extinction map after the method has converged (4 iterations in this case). Note that we set the calculations to only be performed in pixels where the fluxes in the ingoing images are high, resulting in the cutoff beyond $\sim$7" radius from the centre. The bottom left panel shows the difference between the randomised extinction map and the extinction map calculated using only one iteration (a first-pass calculation), and the bottom right panel shows the difference after convergence.

It is clear that the iterative method is superior, at least in this particular case for our particular narrow band dataset. The wavelength dependency of the extinction law and the differences in central wavelength of the line and continuum filters is successfully accounted for without adding any errors to the calculated extinction map. We have in fact found that the method will always find an exact replica of any randomised extinction map applied on the images in the above fashion. However, we should note that we have applied the randomised extinction map using the same extinction law as what is later used to find the extinction. If the law used to calculate the resolved extinction map would not be representative of the underlying extinction the method would of course not find the true underlying map. A physically good result relies completely on if the extinction law is properly chosen for the situation at hand or not. However, this is of course a more

fundamental problem and not unique to this method. The simulation should really only be interpreted as showing that the iterative method is successful at accounting for the wavelength dependency of the extinction law and the wavelength differences between the continuum and line filters. We have tried the method on completely artificially constructed images as well, resulting in the same conclusion as above, as long as the image set adheres to the chosen theoretical Balmer decrement before the randomised extinction map is applied. While we have not been able to construct any artificial set of images where the method clearly does not work, we should still note that this does not mean that the iterative method would generally work on any Hα and Hβ narrow band dataset. As already discussed, when working with real data the method can easily diverge and be worse than a first-pass method if there are errors in the data reduction procedure resulting in for example incorrect continuum subtractions. Thus, the suitability of this method needs to be investigated on a case by case basis.

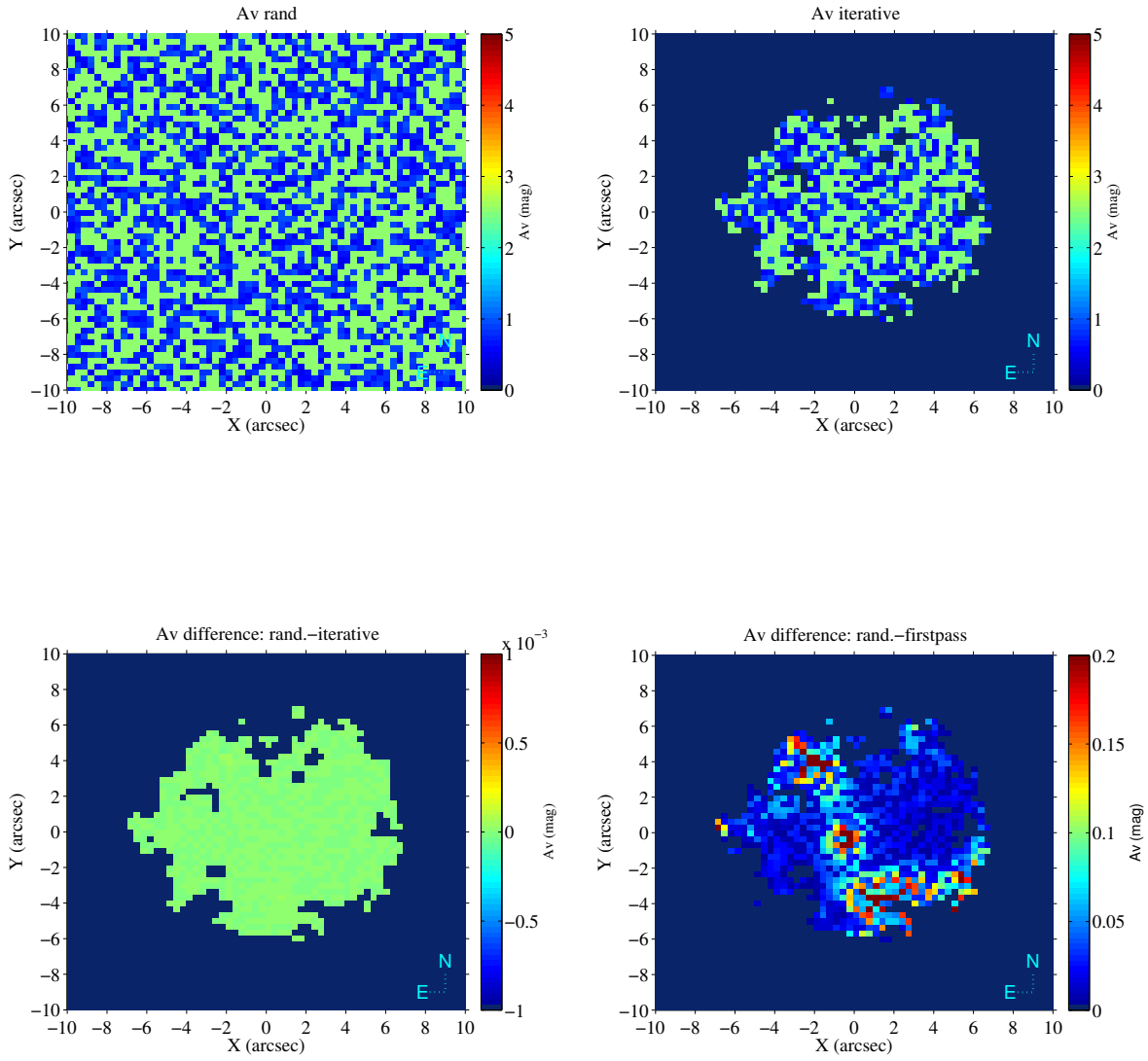

Fig. 13.— Results from applying a randomised extinction and subsequently calculating the resolved extinction using the first-pass and iterative methods described in Section 6.6.1. The top left panel shows the randomised extinction map used to apply the extinction. The top right panel shows the iteratively calculated extinction map after the method has converged (4 iterations in this case). The bottom left panel shows the difference between the randomised extinction map and the extinction map calculated using only one iteration (first-pass calculation), and the bottom right panel shows the difference after convergence (4 iterations). Note that the A_v scale in the randomised-map and iterative-method difference image (bottom left) is set to -1×10^{-3} to 1×10^{-3}. It is clear that the iterative method is superior at least for our particular narrow band dataset.

6.5. Average extinction of Tol 1247-232

By using the total Hα and Hβ fluxes from Figure 2 in Equation 18, and the extinction laws given in Figure 12 we can now calculate an *unresolved* or average extintion in Tol 1247-232. Note that we can easily do this as a function of modelled age, which is shown for the Milky Way (MW) (Fitzpatrick 1999), SMC & LMC (Gordon et al. 2003) and the Calzetti et al. (2000) starburst attenuation law in Figure 14. Note that as we already mentioned in Section 12 the calculations based on the Calzetti et al. (2000) law with $R_V = 4.05$, and the MW law with $R_V = 2.5$ should be considered as extreme cases. However, the net result of including this large span of values for R_V is only approximately a 0.1 magnitude shift from the average value across all laws. Also note that Figure 14 shows a calculation for the Calzetti et al. (2000) law with $R_V = 3.1$ similar to the standard Milky Way value, which results in an almost identical result to the MW law calculation. The differences in the calculation of A_v between the rest of the extinction laws are also largely due to the differing values for R_V, but these differences can be considered negligible since we find that the statistical error alone translates into an 8% error in these calculations. Thus, we find that the average extinction is not very sensitive to the choice of extinction law between the empirical laws for the MW, SMC, LMC and starburst galaxies, but somewhat sensitive to the choice of R_V.

Figure 14 also shows that the calculated average extinction is quite stable with respect to the modelled age for all of the various laws in the relevant age interval between 10 Myr to 100 Myr. The average for the MW, LMC and SMC laws is $A_v \approx 0.44$ in this range. Note that these values excludes the Galactic foreground extinction, $A_V(Gal) = 0.237$. By adding the results in Figure 14 to the Galactic extinction and taking the average of the laws resulting in the highest and lowest A_v for ages between 10 Myr to 100 Myr we estimate the total unresolved extinction for Tol 1247-232 as $A_V(\text{unresolved}) = 0.70$. After correcting for both the galactic and intrinsic average extinction we find, for an age of 30 Myr, the extinction corrected Hα flux 857.7×10^{-15} erg s^{-1} cm^{-2} using a 11" aperture on the galaxy and by adopting the Calzetti et al. (2000) law with $R_V = 3.1$ to correct the line fluxes. Similar calculations has been made by Rosa-González et al. (2007) based on the data in Terlevich et al. (1991) (T91) with the result, $A_V \approx 0.74$ and H$\alpha_{unresolved}$ =851.1×10^{-15} erg s^{-1} cm^{-2}, using the dust extinction law for the Milky Way from Seaton (1979). Note that our calculation above results in a very slightly higher Hα flux, even though our extinction estimate is somewhat lower. This outcome is mainly a result of the aperture that we are using being bigger than the aperture used in T91, which does not include all of the flux from the galaxy. Also note that we find an even

lower $A_v = 0.67$ than Rosa-González et al. (2007) if we only consider the MW extinction law. This is also in part a result of our choice of using a bigger aperture. In the following sections we will show that the majority of the dust in the galaxy appears concentrated in the bright central regions, which will somewhat shift the unresolved A_v towards lower values with increasing aperture.

Relating back to the previous discussion of the age of the burst of star formation currently active in Tol 1247-232 it is interesting to look at the extinction calculated for very young ages. For an age of 1 Myr we find $A_v(\text{intrinsic}) \sim 0.35$ calculated for the MW law to allow easy comparison to the result by Rosa-González et al. (2007). The result is a total extinction toward Tol 1247-232 of $A_v(tot) \sim 0.59$. This can be considered as in slight contrast to the calculations by Rosa-González et al. (2007), and could be interpreted as further evidence that the Hα and Hβ lines are not dominated by emission originating from such an extremely young burst of star formation as indicated by for example the UV spectrum of Tol 1247-232. The average extinction becomes stable and comparable, within 0.1 mag, to the calculation by Rosa-González et al. (2007) for ages above 10 Myr. However, this argument does not hold a lot of weight in the age discussion after the uncertainties in the total isolated line fluxes are taken into account. A Monte Carlo simulation (300 iterations) of the statistical errors propagated all the way throughout our reductions to the calculation of the unresolved A_v results in an uncertainty of approximately 8%. This in combination with the 10% uncertainties in the emission line strengths reported by T91 makes detecting any discrepancy due to the modelled age impossible. The 8% uncertainty in A_v results in a similar uncertainty in the unresolved extinction corrected total line strengths. However, this uncertainty is not important since we will not be basing any further calculations on these unresolved results. We will obtain resolved maps of the extinction in Tol 1247 in section 6.6.1, which allows better estimates of the total emission line strengths.

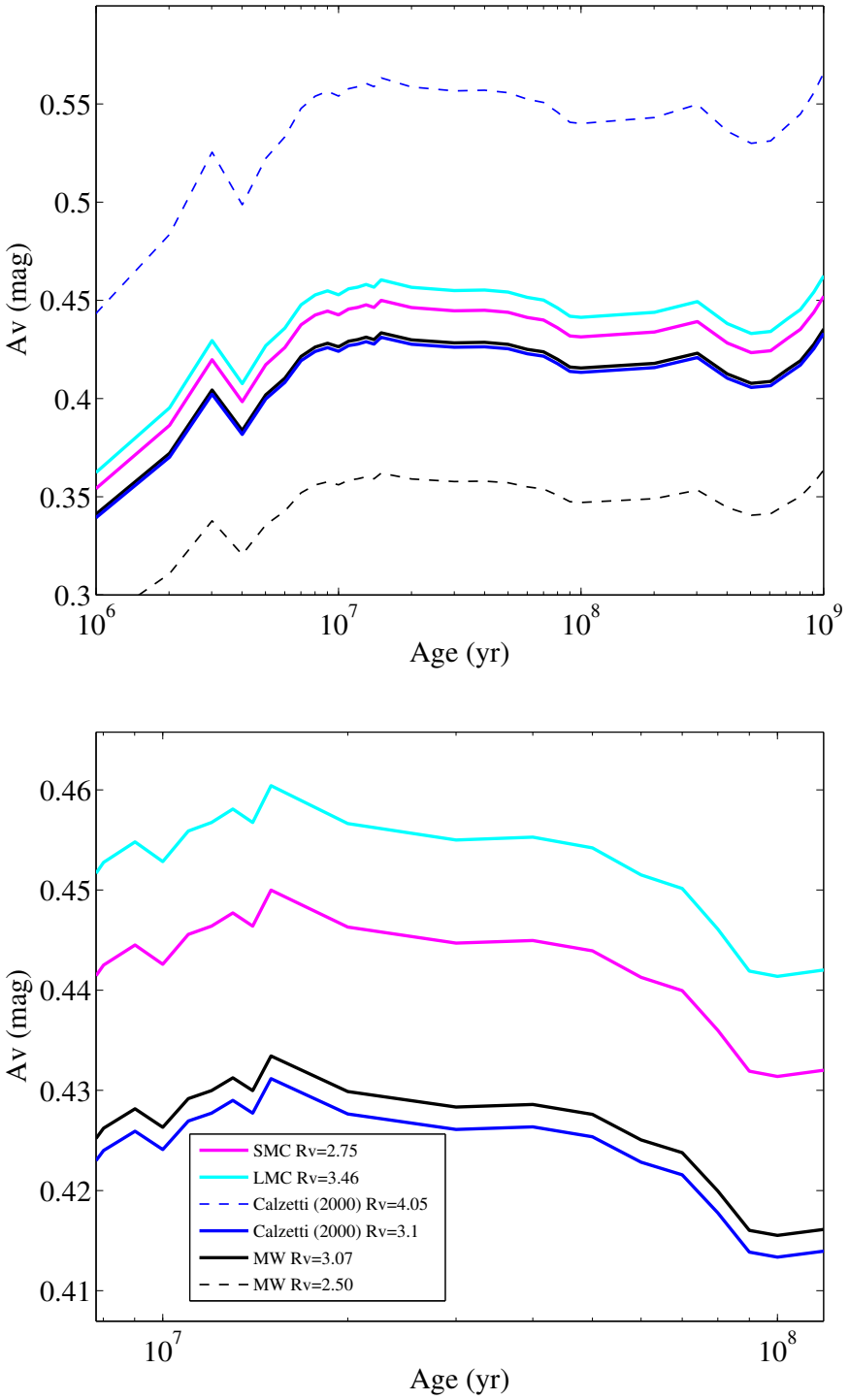

Fig. 14.— Average/unresolved visual extinction for Tol 1247-232 as a function of the modelled age for the dominating burst of star formation. Milky Way, LMC, SMC and starburst (Calzetti et al. 2000) extinction laws are shown. The Galactic foreground extinction $A_v = 0.237$ has been subtracted. The top panel shows the full range of extinction laws that we are using to estimate the average extinction in Tol 1247-232, and the bottom panel is focused on the extinction laws with $R_V \approx 3$. The legend in the bottom panel holds for both panels.

6.6. The importance of a resolved extinction map

Working with the Hα/Hβ line-ratio based average unresolved extinction as was done in the previous section will generally result in an underestimation of the true luminosity of an object. This can be understood by considering a hypothetical galaxy consisting of two separate regions. Consider a scenario with one region having a much higher extinction than the other. Now, remember that we are calculating the extinction from the Hα/Hβ line ratios. An observer would measure that the Hα/Hβ ratio deviates substantially from the theoretical Balmer decrement in the region affected by the higher extinction, while for the lower extinction region the ratio will be closer to the Balmer decrement. Combining the observed flux from the two regions into an unresolved flux will always result in a combined line ratio that is closer to the theoretical value than what really is the case for the region with the highest extinction. Thus, the true flux from a high-extinction region will always be underestimated if flux from a region with lower extinction is contaminating the Hα/Hβ line ratio used to find the average extinction. Not that this is exactly the case for an observer that cannot resolve the two separate regions. To what degree the luminosity from the high-extinction region will be underestimated will be determined by the relative balance between the intrinsic luminosities and the total extinctions of the different regions. Higher overall extinction magnitudes will give higher overall possible errors. In a worst-case scenario the true flux of a region can easily be underestimated by over 50%. The same reasoning can of course also be used to argue that a high extinction region will always cause the extinction to be overestimated in an adjacent region of lower extinction. However, in terms of extinction corrected total luminosities, it can easily be numerically shown that the total luminosity calculated from the unresolved total flux and Hα/Hβ line ratio will still always be underestimated.

A simple simulation can be constructed to show that the reasoning above indeed holds for any combination of intrinsic fluxes and extinction values. This is accomplished by creating two regions with randomised intrinsic luminosity, and applying randomised extinctions on the regions using for example the Milky Way extinction law from Pei (1992). The resulting dust attenuated luminosities from the two regions can then be used to find both a resolved and unresolved extinction for the region using Eq. 18, which in turn allows the unresolved and resolved extinction corrected luminosities to be found. The simple calculation described above can be run a large amount of times, giving us an overview of the possible outcomes for any combination of relative luminosities and extinctions. The result of such a calculation repeated 10^4 times is shown in Figure 15. The randomised luminosities for the two regions are normalised such that the total

luminosity is maximally equal to one. The values for the A_v extinction are set to be drawn randomly from a uniform distribution scaled so that the average value over a large sample is 1.5 magnitudes. This should be reasonable since the unresolved Av is around 0.8 for Tol 1247-232. Note that while the extinction values have been adjusted to suit Tol 1247-232 in the simulation we show, not much generality is lost. The main effect of the adjustment is that the maximal errors will be limited compared to what could be shown for higher extinctions. However, visual extinctions between 0.5-2 magnitudes are typical for HII regions in nearby galaxies. It is immediately clear from the top panel in Figure 15 that the unresolved luminosity never surpasses the resolved luminosity. Further, in the bottom panel of Figure 15 we show the probability for different outcomes. The probability to underestimate the flux by 10% or less when using an unresolved extinction correction under the above assumptions is around 70%. Note that this result only holds when we are working with only two separate regions and when the extinction in the regions is allowed to vary randomly within 0 to 1.5 magnitudes. However, the result of this simulation can be interpreted in a very useful way. Consider a hypothetical astronomical image containing a region consisting of many pixels where we aim to calculate a resolved extinction map. Now if we assume that the underlying extinction will vary approximately randomly between 0 to 1.5 magnitudes in each pixel we can interpret the result of the simulation in Figure 15 as predicting how much we will improve a hypothetical extinction corrected flux measurement by going from a resolved to unresolved calculation. This is easily found as the average relative flux difference of the entire computation shown in the top panel of Figure 15, which is $\sim$0.9. Thus if we expect A_v to vary between 0 to 1.5 magnitudes in an extended astronomical object we will generally underestimate the flux by around 10% if only an unresolved extinction correction is used.

Finally we should discuss what would happen when improving an already resolved extinction map by increasing the resolution. The simulation above assumes that the extinctions and luminosities of the two ingoing regions are uncorrelated. However, if the extinction is already resolved, this is not very realistic. In reality we would in a resolved image expect nearby pixels to show at least somewhat similar luminosity and extinction. If the simulation above is modified so that the two separate regions (pixels) are correlated such that both the intrinsic luminosity and extinction is expected to differ maximally by 20% from one pixel to the other we find that the difference between the resolved and unresolved case will be less than 0.5% with a 99% probability. Note that the only difference compared to the previous simulation is the addition of the correlation between the two regions/pixels. The values for the extinctions are still allowed to vary randomly between 0 to 1.5 magnitudes. This correlated simulation predicts the maximal gain ($\leq 0.5\%$) when

doubling the resolution in an already resolved image, given the specified assumptions. We use this result to investigate the potential gain from increasing the resolution further in the extinction map that we have calculated for Tol 1247-232 in Section 6.6.1.

In conclusion, the extinction should clearly be calculated in a resolved fashion, with as high a resolution as possible whenever possible. However, in practice there will of course be diminishing returns from improving the resolution endlessly. The smaller the region that is resolved in each pixel, the less difference in flux and extinction will be present between adjacent pixels. As already mentioned, if adjacent pixels show flux values and extinction values within 20% of each other, our simulation shows that the gain from doubling the resolution will be less than 0.5%. We demonstrate the difference in the total extinction corrected Hα flux from using a resolved and unresolved extinction calculation for Tol 1247-232 in Section 6.7, where we also discuss if further improvement of the resolution of the A_v map would be beneficial.

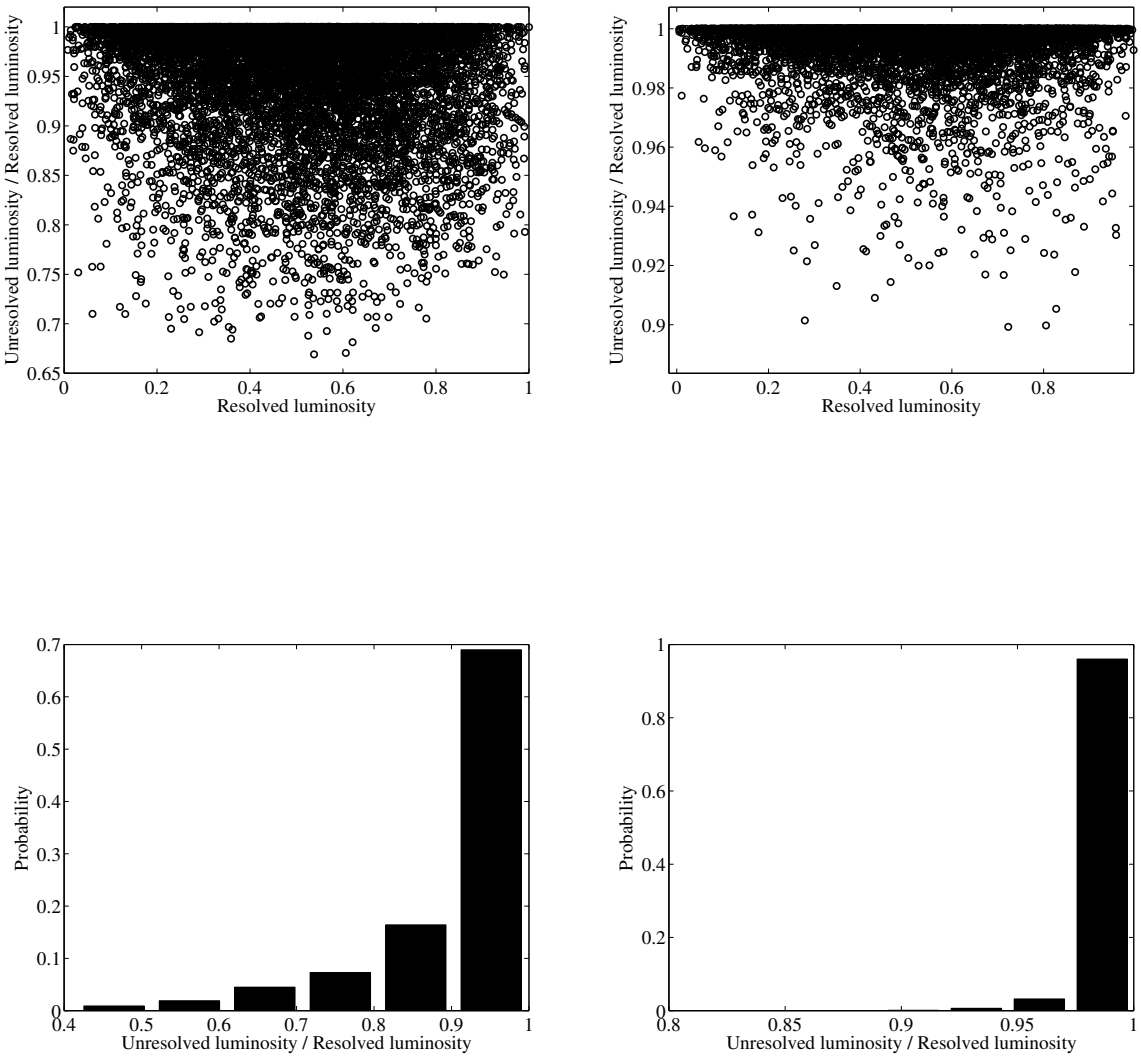

Fig. 15.— The simulated theoretical difference between using a resolved and unresolved extinction when correcting the flux from two spatially resolved regions. The left panels show an uncorrelated simulation. The right panels show a simulation where the extinction of the two separate regions is correlated within 15%. Top panels: The total theoretical luminosity from the two regions is shown on the horizontal-axis, scaled such that the maximal luminosity is unity. The vertical axis shows the unresolved luminosity divided by the resolved total luminosity, i.e. how much the luminosity is underestimated in the unresolved case. Bottom panels: the probability distribution of the unresolved luminosity divided by the resolved luminosity calculated from the results in the top panel.

6.6.1. Resolved A_v extinction maps of Tol 1247-232

We use the resolved Hα and Hβ flux line images, shown in Figure 9, the first-pass method described in Section 6.2.1 and the iterative method described in Section 6.4 to compute the extinction in each pixel and to obtain a visual extinction map of Tol 1247-232 for a modelled age of 30 Myr, Figure 16. The Fitzpatrick (1999) extinction law with $R_V = 3.07$ was used for these calculations. To eliminate large extinction variations/noise in the outskirts of the galaxy we have set the extinction to zero when either the Hα or Hβ fluxes fall below a signal threshold of around $10 \cdot \sigma_{sky}$ estimated from the continuum subtracted images. Calculation further than 7" from the galaxy centre results in rather noisy regions with extreme variations in the extinction values between each pixel. Thus, we have limited the size of our extinction maps presented in Figure 16 to approximately 7". Note that the extinction clearly appears to trace the shape of the high luminosity areas in the galaxy, and especially note the dusty possible spiral arm west of the central regions.

Usage of the iterative method results in somewhat higher extinction values across the entire galaxy, with the extinction typically differing by a little less than +0.1 magnitudes in each pixel. However, in the regions of highest extinction, the effect of using the iterative method can be a little more pronounced showing up to a maximum of 0.25 magnitudes difference between the methods. Experimentation with the iterative method has shown that large differences (over $\sim$0.5 mag) between the methods generally only occur when the signal to noise is very low, or if there is another underlying problem, such as mis-aligned images. As we already have shown, the effect of the iterative method is expected to be quite subtle. It is only correcting for the minor differences in the extinction coefficients (due to the wavelength differences) used for the various line and continuum filters. Thus, we see no indication that the iterative method is not working as intended.

We show the effect of the Galactic foreground extinction in Figure 17. The top panel shows a converged iterative calculation of an extinction map where the Galactic foreground extinction has not been subtracted prior to the calculation and the bottom panel in the figure shows the same calculation performed after the foreground has already been subtracted. Note that ideally the Galactic foreground should be subtracted before any further calculations are made, since the wavelengths of the emission-lines are redshifted when they interact with the dust in the Milky Way, but not when traveling through the ISM in Tol 1247-232 itself. This figure should only be considered as an illustration of the effect of the Galactic foreground extinction.

Figure 18 shows converged extinction maps calculated for the MW, LMC, SMC and Calzetti et al. (2000) extinction laws. The results are extremely similar with the exception of the Calzetti et al. (2000) law when $R_V = 4.05$ is used, which results in a systematic increase in extinction of around +0.1 mag on average, similar as for the average extinction discussed in Section 6.5.

Monte Carlo simulations have been run like in the previous sections to estimate the statistical uncertainty in the extinction maps. We find that the general appearance of the maps presented in Figure 16 remains largely unchanged, with errors that are relatively small (~ 0.1 mag) in the central regions. However, as the radius from the centre increases, and the total flux drops in the ingoing Hα and Hβ images used to calculate the A_v map, the errors successively increase. At a radius of approximately 3" the errors are around 0.2 mag in each pixel, and toward the very outermost parts at around 6" radius in the maps the uncertainty in each pixel can approach 1.0 magnitudes.

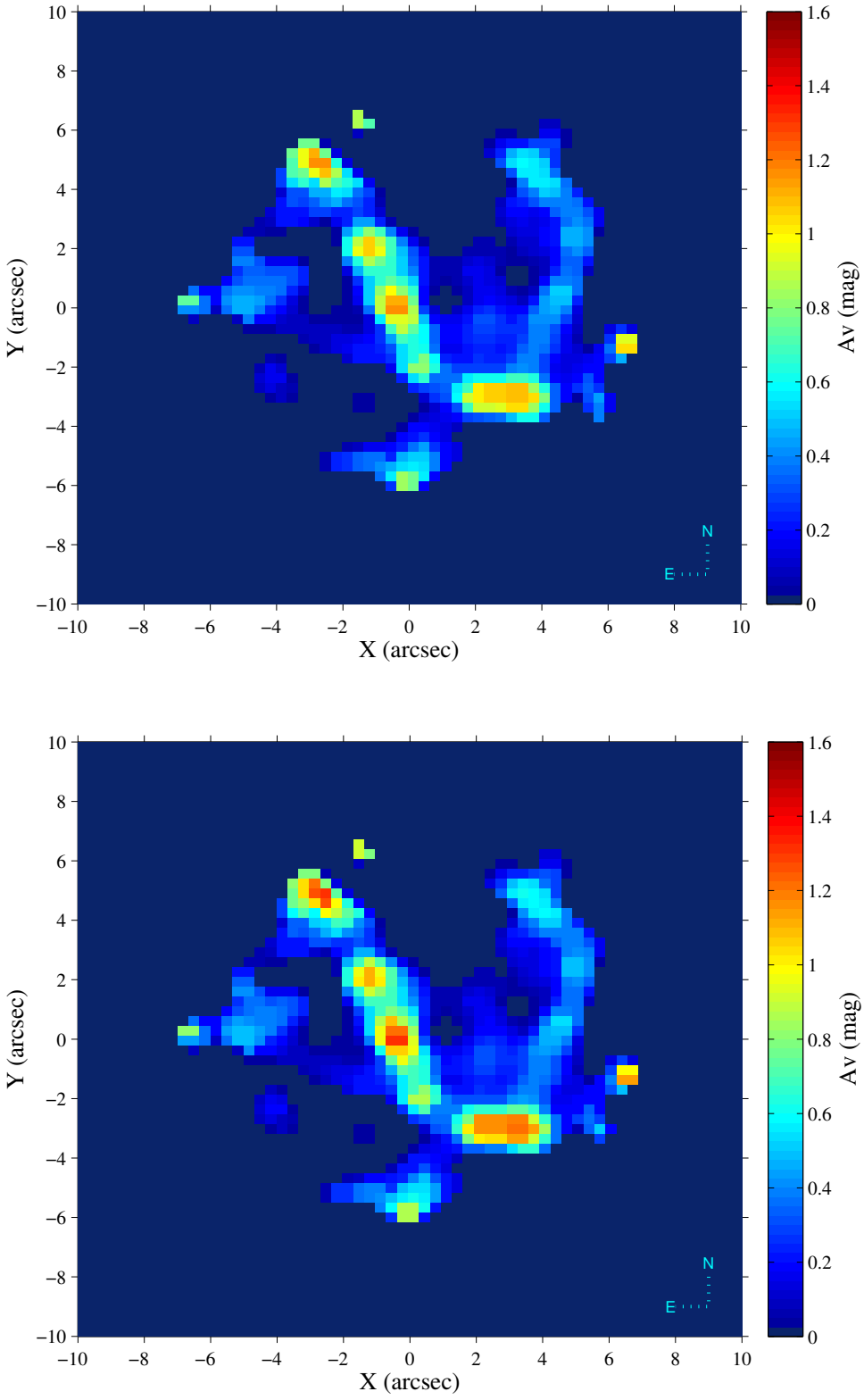

Fig. 16.— Av extinction maps for Tol1247-232 calculated using the Fitzpatrick (1999) extinction law with Rv=3.07. Av is given in magnitudes. The top panel shows a first-pass extinction calculation and the bottom panel shows A_V calculated using the iterative method described in Section 6.4 after convergence.

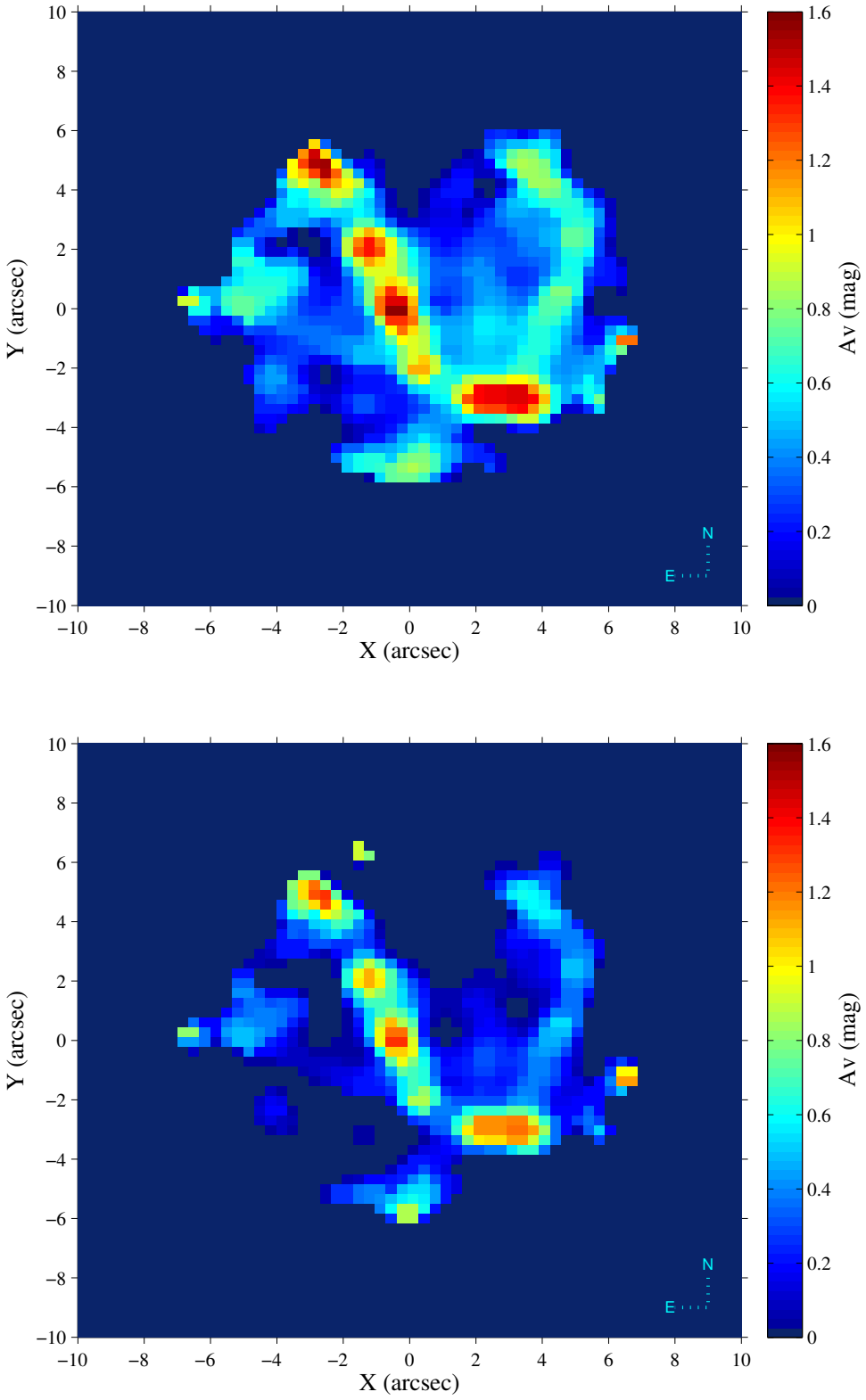

Fig. 17.— *Av* extinction maps for Tol1247-232. Calculated using the Fitzpatrick (1999) extinction law with Rv=3.07. The top panel shows a calculation where no Galactic foreground subtraction has been performed. The bottom panel shows a calculation that has been run after the Galactic foreground extinction $A_{v,gal} = 0.237$ has been subtracted.

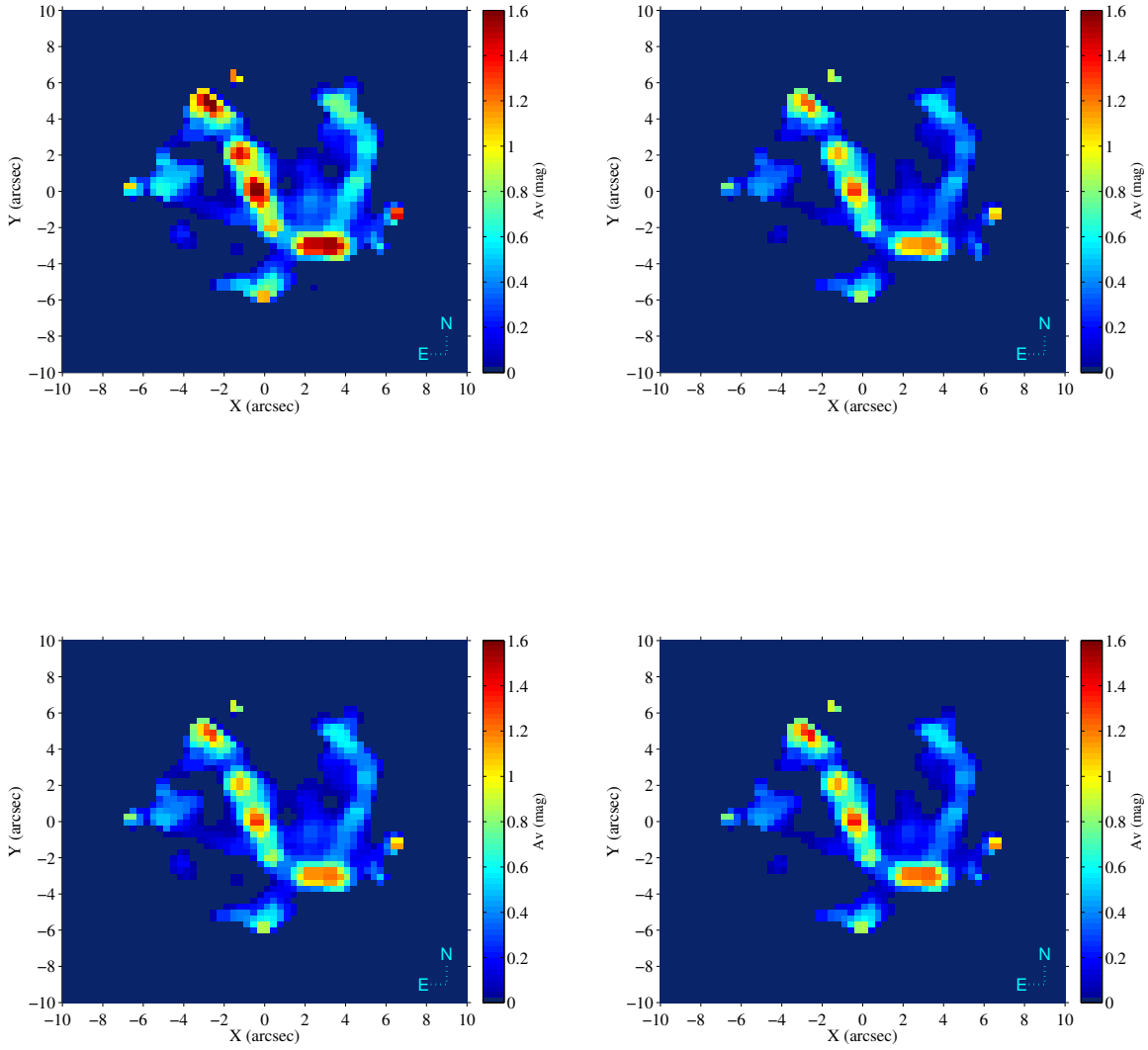

Fig. 18.— Comparison of Av extinction maps for Tol 1247-232 calculated using various extinction laws. Top left: Calzetti et al. (2000) law with Rv=4.05. Top right: Gordon et al. (2003) for the Large Magellanic Cloud with Rv=3.46. Bottom left: Fitzpatrick (1999) with Rv=3.07. Bottom right: Gordon et al. (2003) for the Small Magellanic Cloud with Rv=2.75. The Galactic foreground extinction $A_{v,gal} = 0.237$ has been subtracted from all maps.

6.7. An extinction corrected Hα map and the total extinction corrected Hα flux of Tol 1247-232

To assemble a map of the total Hα flux in Tol 1247-232 we apply the resolved extinction maps shown in Section 6.6.1 calculated using our iterative method on our Galactic extinction corrected Hα line image shown in Figure 9. We present the extinction corrected Hα flux density map of Tol 1247-232 in the top panel of Figure 19. For completeness we also present an extinction corrected Hβ line map in the bottom panel of Figure 9. These maps were calculated for a modelled age of 30 Myr. Also note that these particular maps were made by both calculating and applying the extinction using the Calzetti et al. (2000) attenuation law with $R_V = 3.1$.

Now, to estimate the total extinction corrected Hα flux of the galaxy we use aperture photometry with a 7" radius aperture and a +0.8% aperture correction[1]. We obtain the integrated Hα line flux, H$\alpha_{resolved}$ =971.3 $\times$ 10^{-15} erg s^{-1} cm^{-2}, calculated as an average from the extinction laws shown in Figure 6.3 with a somewhat modified range of values for the total to selective extinction R_V in order to match the laws we used to calculate the unresolved extinction in Figure 14. We estimate that this flux is accurate to 15% as an estimate for the total Hα flux for Tol 1247-232. Note that this result does not take the Calzetti et al. (2000) extinction law with $R_V = 4.85$ into account when the average is calculated. This is just to allow comparison with the unresolved case we showed in Figure 14. However, this averaged estimate is not very critical at all since we will keep calculating all of our results in the following sections separately for the various extinction laws.

See Figure 21 for the extinction corrected flux as a function of modelled age for the various extinction laws. The statistical uncertainty in the extinction corrected fluxes calculated for a specific law and specific age is typically 5%. Also note that this is still an integrated flux, we have only labeled it as H$\alpha_{resolved}$ to distinguish it from the previously calculated unresolved case, H$\alpha_{unresolved}$ =857.7 $\times$ 10^{-15} erg s^{-1} cm^{-2} calculated using the average extinction for Tol 1247-232 found in Section 6.5. H$\alpha_{resolved}$ is only resolved in the sense that we are using a resolved extinction map to correct the Hα line flux separately for each pixel in the original dust attenuated Hα line image. In the case of Tol 1247-232 We find H$\alpha_{unresolved}$ = 0.88H$\alpha_{resolved}$. Note that this can be seen as the expected result from using a resolved extinction map, since the extinction is systematically underestimated if

[1]We motivate the aperture correction used to find the total flux in Section 3.

only an average extinction across the entire object is used. Remember that we showed in Section 6.6 that going from a completely unresolved to a resolved extinction can in a simulated scenario roughly tuned to our dataset result in around a 10% gain in accuracy. In this case the simulated prediction happened to almost exactly match the observed outcome. However, we should definitely note here that the net effect of using a resolved extinction map will vary from object to object. The excellent prediction by the simulation here is very likely a coincidence. We will further discuss the choice of extinction law and the effect of the various extinction treatments (unresolved, first-pass, iterative) on the total extinction corrected flux in the following section where we also discuss how we arrive at the estimated total uncertainty in our final extinction corrected Hα flux shown above.

6.8. Uncertainties in the extinction corrected Hα emission line flux

Monte Carlo simulations are again used to investigate the statistical uncertainty due to Poisson noise. Figure 20 shows a typical result calculated using the Calzetti et al. (2000) extinction law with $R_V = 4.05$. We find that the typical errors are approximately 5% in calculations for a specific extinction law and modelled age. It is worth noting that this is a lower uncertainty than what we obtain when correcting the Hα flux using the unresolved average extinction, which typically results in an 8-10% statistical error. This is due to the unresolved method inherently being more unstable. A small shift in either the integrated Hα or Hβ flux as a result of the statistical uncertainty results in a total shift in the extinction correction for every pixel in our images at the same time. This is not the case if each pixel is treated independently. Note also that if the full uncertainties in the Terlevich et al. (1991) integrated emission line strengths are taken into account, the estimated average A_V for Tol 1247-232 would have a roughly 35% uncertainty. Thus we are able to vastly improve our treatment of the extinction in the galaxy by using the resolved extinction maps.

However, the main source of uncertainty in our extinction corrected Hα flux is as we have already shown in Figure 6.3 more fundamental, and lies in the choice of extinction law and R_V. With the choice of R_V predominantly acting as the largest source of error and the choice of extinction law between the MW, SMC, LMC and starburst laws being less important. Unfortunately we do not currently have enough information about the properties of the dust in Tol 1247-232 to be able to tell what the proper choice of R_V is. And because of this we will again opt to work with a large range in R_V throughout our calculations in the following sections, which allows the effect of these choices to always

be seen. The result of this problem is an increase in the uncertainty of our extinction corrected best-estimate for the total Hα flux from 5% due to the statistical errors to a full 15% if R_V is allowed to vary between $R_V = 2.5$ and $R_V = 4.85$. Note also that when the Calzetti et al. (2000) law is used, the continuum emission should be corrected using a lower $E(B-V)$ than for the nebular emission according to

$$E_s(B-V) = 0.44 E_{HII}(B-V)$$

as already discussed in Section 6.2.1. However, the application of this to our narrow band data becomes somewhat complicated since all of our images include both nebular and continuum emission to varying degree. Fortunately the Zackrisson et al. (2011) models predict the contribution from the emission lines to each filter, and thus we can apply a combination of the continuum and nebular corrections to each of our images accordingly. However, we unfortunately find that any benefit in accuracy in the corrections that could be achieved by following this recipe is lost when we again consider that we do not know R_V with any certainty. We can only note that the general trend when the continuum contributions to the filters are corrected with a lower $E(B-V)$ is a slight lowering of a few percent of the corrected Hα flux. This only very slightly lowers the maximal error in the positive direction from the mean value across all of the adopted extinction laws, and is already taken into account in the estimated 15% uncertainty above.

Figure 21 also shows the typical differences in calculated Hα flux for the three different extinction correction methods that we have used. We again note that we saw that going from a completely unresolved extinction to a resolved map resulted in a extinction corrected flux increase of around 12%. This is in good agreement with our simulation in Section 6.6 when the luminosities and extinctions in the simulation are allowed to change randomly within appropriate values for typical HII regions. When going from a first-pass calculation to a converged iterative calculation the flux increases by around 3%. Since we have found no problems with the iterative method, we will simply consider it as the preferred choice, since we in this way avoid introducing systematic errors due to the wavelength dependency of the extinction corrections to the line and continuum filters.

Finally we should discuss what would happen if we could increase the resolution of the A_v map further. Consider if we would make a hypothetical observation where each pixel in our image would be resolved in two different pixels. Now in this case we would expect the flux and extinction in these pixels to be correlated and quite similar. In such a correlated scenario the simulation in Section 6.6 shows that the benefit would be much less than the 10% gained when going from a completely unresolved case to a resolved case. We can in fact estimate an upper limit to the possible benefit by investigating our

results in Figure 16 and Figure 19. If we consider two adjacent pixels in our image, we find that the flux in the pixels are typically within 20% of each other and the extinctions are typically within 15% of each other. If we incorporate this in the simulation described in Section 6.6 the result is that the flux increases by less than 1% when going from the unresolved to the resolved case. Thus we can estimate that halving the resolution of our image would underestimate the total flux only by around 1%. Similarly if the resolution would be doubled we estimate that the total flux would increase by less than 1%.

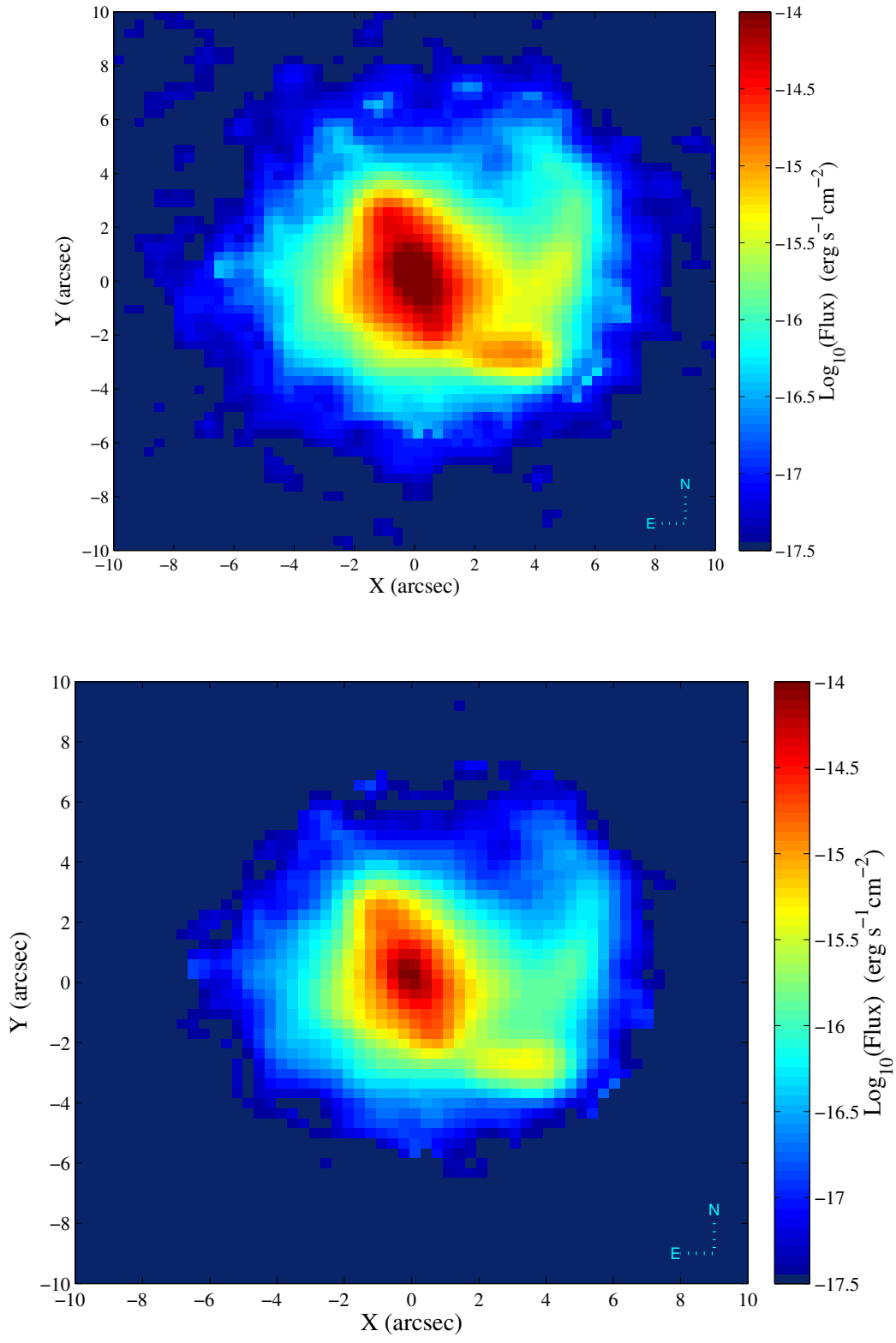

Fig. 19.— Top: Extinction corrected Hα flux map. Bottom: Extinction corrected Hβ flux map. These maps have been constructed using the Fitzpatrick (1999) extinction law with $R_V = 3.07$ and the intrinsic Balmer decrement Hα/Hβ=2.81.

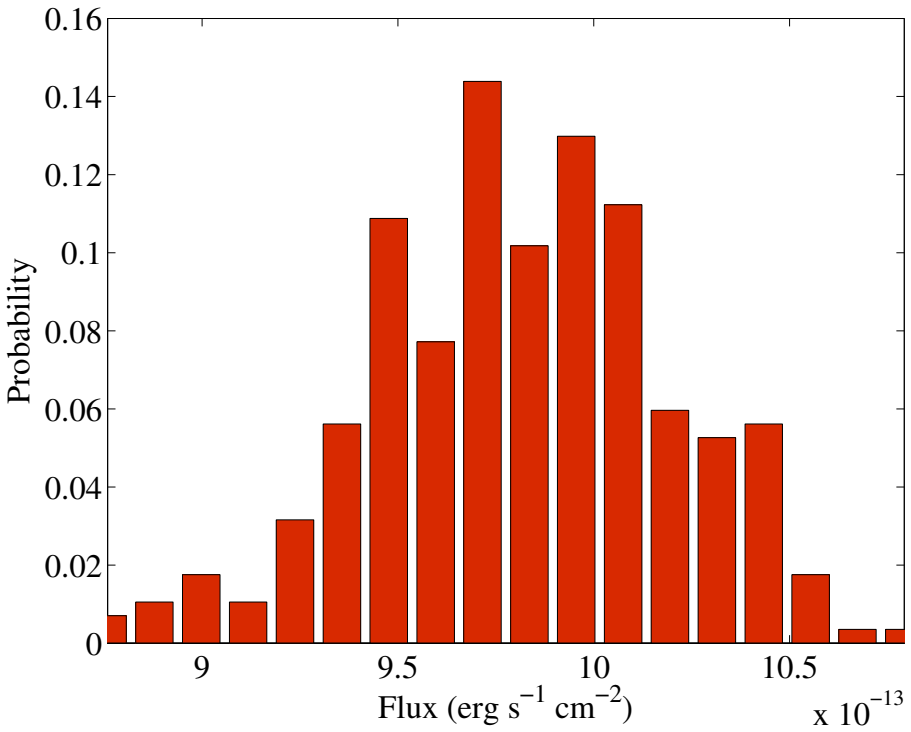

Fig. 20.— Monte Carlo simulation of the poisson noise impact on the total extinction corrected Hα flux from Tol 1247-232. The standard deviation of the distribution is 5% of the mean value which is Hα =981.7 $\times$ 10^{-15} erg s^{-1} cm^{-2}. This calculation uses the Calzetti et al. (2000) law with $R_V = 4.05$.

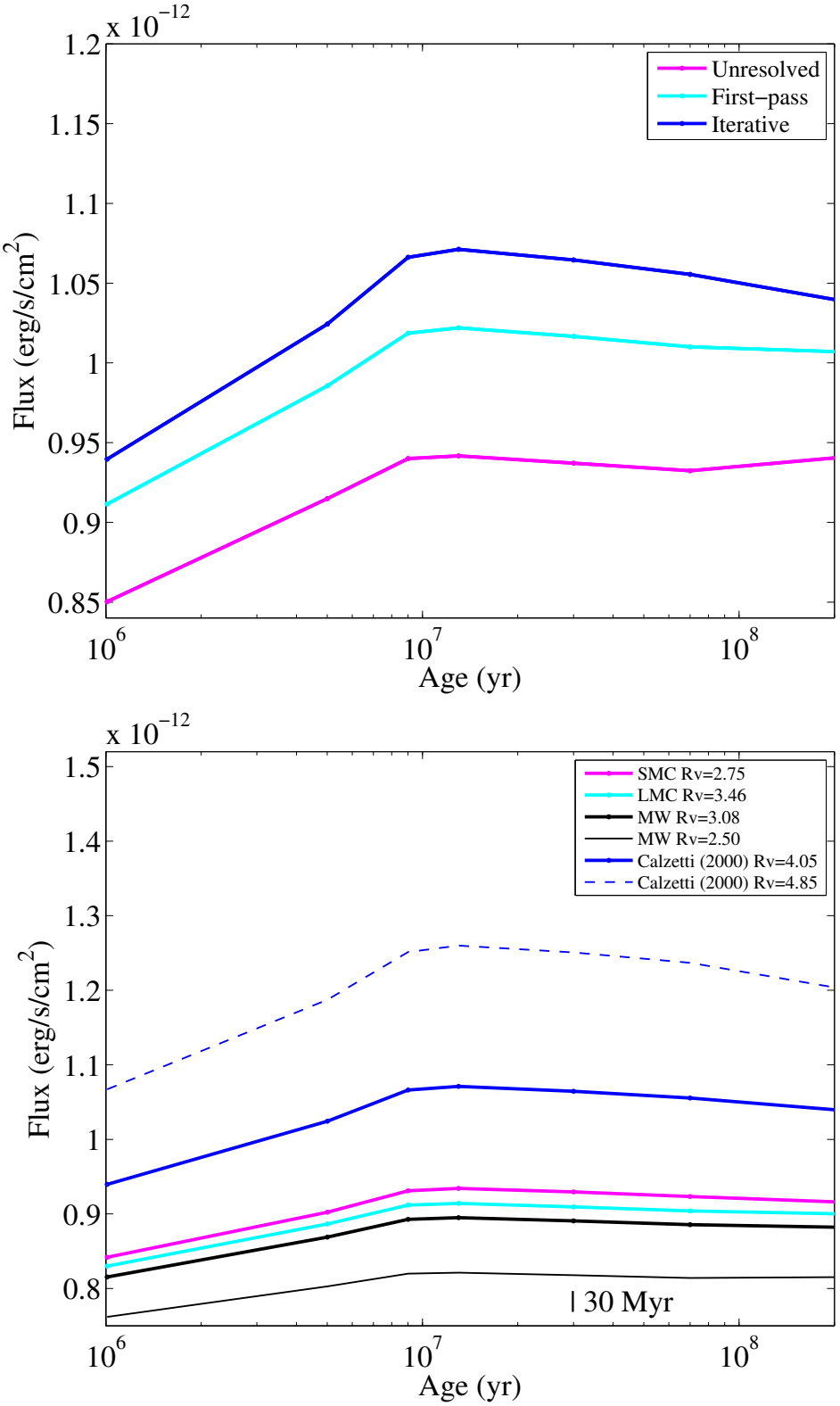

Fig. 21.— Top panel: The differences in corrected Hα flux between the various methods used to calculate the extinction. This particular calculation is done for the Calzetti et al. (2000) extinction law with $R_V = 4.05$. Bottom panel: Extinction corrected Hα flux as a function of age for the adopted extinction laws calculated using the iterative method after convergence.

7. Measuring the leakage of ionizing photons

To robustly quantify the leakage of ionizing photons from galaxies, a successful direct detection of the leaking photons with wavelengths $\lambda \leq 912$ Å must first be made. This is as we have already discussed in Section 1 not at all trivial, and in the local universe we are working with only two separate detections. Haro 11 and Tol 1247-232 by Bergvall et al. (2006) (B06) and Leitet et al. (2013) (L13) respectively. These detections were made by analysing spectra obtained with the Far Ultraviolet Explorer (FUSE) (Moos et al. 2000). Both B06 and L13 quantify the amount of leaking photons by measuring the flux density[1], $f_{900_{obs}}$ at $\lambda = 900$ Å. These measurements are related to the total number of leaking photons,

$$f_{900,obs} \propto N_{LyC,esc} \tag{23}$$

where $N_{LyC,esc}$ is the intrinsic LyC photon production measured in s^{-1}. Now to estimate the absolute escape fraction, f_{esc}^{LyC} we must relate either $f_{900_{obs}}$ or $N_{LyC_{obs}}$ to the total intrinsic production, $f_{900,int}$ or $N_{LyC,int}$ in the galaxy, i.e.

$$f_{esc}^{LyC} = \frac{f_{900,obs}}{f_{900,int}}, \text{ or } f_{esc}^{LyC} = \frac{N_{LyC,esc}}{N_{LyC.int}} \tag{24}$$

Thus we must somehow estimate the intrinsic production of ionizing photons. As we have already mentioned in Section 1 this can be done by using the luminosity of radiation from young massive stars, since these are the dominating source of ionizing photons in galaxies without AGN contributions. Various methods to estimate the intrinsic luminosity of the youngest stars exist, mainly due to the large amount of work that has traditionally been done to estimate the SFR of star forming galaxies. However, here we will use the observed total luminosity of the Hα line originating from the ionized HII regions that form around the young massive stars. We derived a very robust estimate for the total Hα flux in the previous sections. The usage of Hα line observations is especially well suited for estimating the SFR or f_{esc}^{LyC}, since star-forming regions are expected to be associated with high dust content, see e.g. Rosa-González et al. (2002). And the dust can be measured by comparing the Hα line to the Hβ line. Remember that we clearly showed in Section 6.6.1 that the dust (and thus high extinction) in Tol 1247-232 is concentrated around the brightest central regions, and also in the spiral-arm like structure to the west in the galaxy. These regions are also where we would expect the most massive stars to

[1]The flux density is measured in units of erg s^{-1} cm^{-2} $Å^{-1}$, and quantifies the radiance at the specified wavelength.

be located. Analysing the dust content in this way is critical, since a correct estimate for the total flux or luminosity of the Hα line, and thus also for the intrinsic production of ionizing photons depends strongly on successfully accounting for the dust attenuation of the emission line.

We were able to conveniently correct the Hα line for the extinction by interstellar dust. This was possible because the physics of dust extinction has been very well studied for wavelengths between UV ($\lambda \geq 912$ Å) to near infrared (Pei 1992; Fitzpatrick 1999; Schlafly & Finkbeiner 2011). This wavelength range of course includes the Hα line. However, how photons in the Lyman continuum below ($\lambda \leq 912$ Å) are affected by the presence of dust in the HII regions is not as well understood. Thus, we must investigate the possible complications that are caused by this for estimating the absolute escape fraction.

From observing the Hα line we are restricted to estimating the total amount of LyC photons that contribute to the ionization of the hydrogen in the HII region,

$$f_{H\alpha} \propto N_{LyC.gas} \tag{25}$$

If we assume that an adequate measure of the total intrinsic amount of LyC photons is the measured leakage combined with the Hα inferred LyC photon production we can then find the escape fraction from the observed leakage of LyC photons and this total intrinsic LyC estimate,

$$N_{LyC.int} \approx N_{LyC,esc} + N_{LyC,gas} \tag{26}$$

which would give us the absolute escape fraction,

$$f_{esc}^{LyC} = \frac{N_{LyC,esc}}{N_{LyC,esc} + N_{LyC,gas}} \tag{27}$$

However, If part of the LyC photons emitted by the massive stars in the central parts of the region are affected by extinction on dust grains, part of the total amount of produced LyC photons will never contribute to the ionization of hydrogen at all, resulting in a systematic underestimation of the intrinsic LyC photon production, if the estimate is based solely on the extinction corrected Hα line strength. In reality the total intrinsic amount of LyC photons would then in the presence of Lyman Continuum Extinction (LCE) have three components,

$$N_{LyC.int} \approx N_{LyC,esc} + N_{LyC,gas} + N_{LyC,dust} \tag{28}$$

Thus, to find the absolute escape fraction, now given by,

$$f_{esc}^{LyC} = \frac{N_{LyC,esc}}{N_{LyC,esc} + N_{LyC,gas} + N_{LyC,dust}} \tag{29}$$

we would now also need to estimate the amount of LyC photons that has been absorbed by dust.

7.1. LyC dust absorption

The effect of energetic LyC photons being absorbed by dust particles is a net heating of the dust, which subsequently results in infrared emission that can be measured. Thus, it is at least in theory possible to estimate how much of the intrinsically produced photons are absorbed. This LyC dust extinction effect was predicted by Petrosian et al. (1972), who create an analytical model of a dusty HII region and use their model and observationally inferred Lyα and infrared data to show that 26% of the LyC photons should be absorbed by dust in the Orion nebula. The theory is based upon investigating how Lyman-alpha (Lyα) interacts with dust. Simulations of LyC leakage also show this effect, with e.g. Yajima et al. (2011) showing a large range ($\sim$10% to 60%) of LyC dust absorptions in the results of their simulations.

Lyα photons are produced when the excited atoms in an HII region eventually recombine, resulting in emission of new photons. Lyα originates from the 2^2P to the 1^2S energy level of the hydrogen atom resulting in emission at wavelength $\lambda = 1215.668\,$Å. Eventually the emitted Lyα photons reach the neutral HI regions surrounding the HII regions and become re-absorbed. However, Quantum Mechanical (QM) effects result in subsequent resonant scattering (Weisskopf 1931) of the Lyα photons as they traverse the HI region. The mean free path of these photons is extremely small, causing them to be absorbed and re-emitted rapidly. Because of the short mean free path the probability for the Lyα photons to eventually be absorbed on dust grains also becomes large over time, with the net effect again being a heating of the dust, similarly as in the case of LyC photons being directly absorbed.

Petrosian et al. (1972) calculate an estimated dust heating due to Lyα photon absorption and compare this with a measurement of the total infrared flux of the Orion Nebula. The ratio of the total infrared flux to the Lyα contribution estimate is then a measure of the amount of LyC photons that were absorbed on dust already before ionizing any hydrogen.

Inoue et al. (2001) expand on the theory by Petrosian et al. (1972), by developing

a method to find the fraction of ionizing photons not absorbed by dust, given by f, by measuring the selective extinction E(B-V), the total infrared luminosity, and the total Hα flux. The LyC absorption fraction, which is then given by $(1-f)$, is found by comparing the total infrared flux to the inferred LyC photon production found via Hα. Inoue et al. (2001) also account for part of the infrared luminosity originating from heating by non-ionizing photons with $\lambda \geq 912$ Å. Inoue et al. (2001) further find that the average LyC dust absorption fraction, $(1-f)$, for HII regions in the Milky Way is $f = 0.45$. Which is quite substantial, and definitely should be taken into account when estimating LyC leakage. Thus Eq. 29 and not Eq. 27 should be used for estimating the absolute LyC escape fraction. However, the method developed by Inoue et al. (2001) makes a range of assumptions. Primarily, Inoue et al. (2001) assume that there is no leakage of ionizing photons, and further it is also assumed that all of the LyC photons that are not ionizing hydrogen are absorbed on dust. We will base our calculations on the results obtained by Inoue et al. (2001). However we will develop the theory somewhat further to include LyC leakage, and also leakage of Lyman-alpha (Lyα) photons, which has also been observed in Tol 1247-232.

Based on the theory of the IR emission from dust by Petrosian et al. (1972), Inoue et al. (2000, 2001) derive a relation between the observed IR luminosity and the number of LyC photons inferred from observing the effect of the ionizing radiation on the HII region,

$$\frac{L_{IR}^{dust}(8-1000\mu m)/L_{\odot}}{N_{LyC,gas}/5.63\times10^{43}s^{-1}} = \frac{0.44-0.28f+0.56\epsilon}{f} \tag{30}$$

where $L_{IR}^{dust}(8-1000\mu m)$ is the total infrared luminosity in the specified wavelength range, which includes all of the infrared luminosity to a good approximation, f is the fraction of ionizing LyC photons and ϵ is the average efficiency of dust absorption for non-ionizing photons with $\lambda > 912$ Å calculated for OB stars[1]. 5.63×10^{43} s^{-1} is a theoretical estimate of the number of LyC photons produced per unit solar luminosity calculated from the bolometric luminosity of OB stars, thus dividing $N_{LyC,gas}$ by this number results in an estimate of the bolometric luminosity of the ionizing photons derived from the ionized gas. For details we refer to Inoue et al. (2000) and Inoue et al. (2001). The formula above can be rewritten in a slightly more user friendly way by normalising the infrared

[1]The choice of working with OB stars is natural also in our case since we are dealing with a scenario where young massive stars are cointinuously being formed. And we have already shown that the UV to optical emission of Tol 1247-232 is dominated by emission from a very young burst of star formation.

luminosity and LyC photon production rate resulting in,

$$f = \frac{0.44 + 0.56\epsilon}{0.28 + 5.6(L_{IR,7}/N'_{LC,50})} \tag{31}$$

where $L_{IR,7}$ and $N'_{LC,50}$ is the infrared luminosity and LyC photon production rate normalised by 10^7 $L_\odot$ and 10^{50} s^{-1} respectively.

The average dust absorption efficiency, ϵ, for photons with $\lambda > 912$ Å has already been investigated by Inoue et al. (2001) for a mixture of OB stars. Inoue et al. (2001) are able to derive a relation between the observed colour excess $E(B-V)$ inferred from the Balmer decrement and ϵ. However, this calculation depends on the choice of extinction law, and since we are using a wide range of extinction laws we will recalculate this factor using a similar procedure as in Inoue et al. (2001). The total absorption and scattering optical depth of dust is given by

$$\tau_\lambda = \frac{\tau_\lambda^{abs}}{1-\omega_\lambda} = \frac{A_\lambda}{2.5log_{10}(e)} \tag{32}$$

where τ_λ^{abs} is the absorption optical depth, ω_λ is the dust albedo and A_λ is the total amount of extinction at wavelength λ. A_λ can be determined from an extinction curve and the colour excess $E(B-V)$ (Eq. 22). The efficiency of dust absorption at some wavelength, ϵ_λ, can now be expressed as

$$\epsilon_\lambda = 1 - e^{-\tau_\lambda^{abs})} = 1 - 10^{-0.4k(\lambda)E(B-V)(1-\omega_\lambda)} \tag{33}$$

We can now find the average efficiency of dust absorption for non-ionizing photons by averaging ϵ_λ over an appropriate wavelength range, and weighting the average by the flux density of the stellar distribution as a function of wavelength within the chosen range. We will use a blackbody approximation for the weighting with a temperature of T=30000 K. Further we will calculate the average over a wavelength range of 1100 Å to 3500 Å, since the emission from OB stars is negligible at longer wavelengths. We will use the dust albedo $\omega_\lambda = 0.55$ and assume that it is constant over the entire wavelength range, which is a good approximation for these wavelengths, see e.g. Weingartner & Draine (2001). We show the result of this calculation for the Fitzpatrick (1999) (Milky Way), Gordon et al. (2003) (SMC & LMC) and Calzetti et al. (2000) (starburst) extinction laws in in Figure 22. Note that while the Calzetti law differs substantially from the others in this figure, the effect is lessened in actual calculations where ϵ is used, since the high Rv=4.05 will systematically predict lower observed colour excess E(B-V).

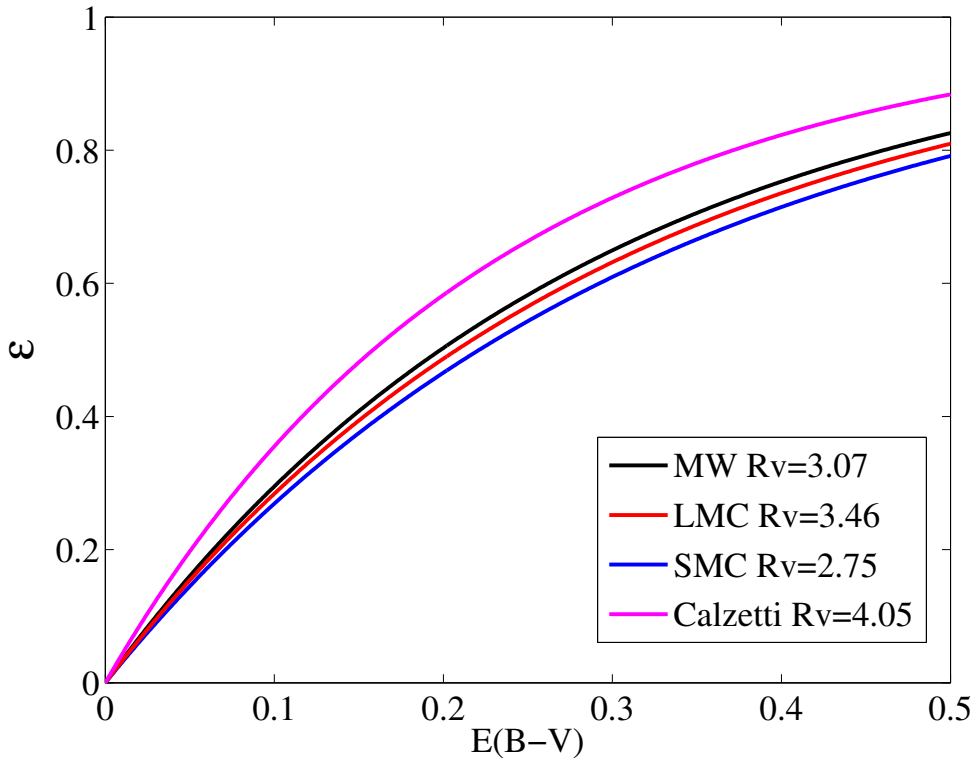

Fig. 22.— The the average efficiency, ϵ, of dust absorption for non-ionizing photons with $\lambda > 912$ Å as a function of the observed colour excess E(B-V). A constant dust albedo $\omega = 0.55$ is assumed.

However, even if we now can properly calculate ϵ, the formulas above by Inoue et al. (2001) still do not take Lyα and LyC escape into account. To account for this we begin similarly to Petrosian et al. (1972) and Inoue et al. (2000) by relating the theoretical total infrared luminosity to the total Lyα luminosity and the total intrinsic luminosity of ionizing and nonionizing radiation produced by the mixture of stars at the centre of an HII region,

$$L_{IR}^{dust} = L_{Ly\alpha,tot} + (1-f) < h\nu >_{ion} N_{LyC,int} + \epsilon L_{nonion} \tag{34}$$

where $< \nu >_{ion}$ is the averaged energy of LyC photons. However, in the presence of LyC and Lyα leakage we must augment the above equation accordingly.

If we begin by assuming that the leaking LyC photons are escaping through dust-free channels in the HII region, and do not contribute to the IR luminosity, the equation takes the form

$$L_{IR}^{dust} = L_{Ly\alpha,tot}(1-f_{esc}^{Ly\alpha}) + (1-f) < h\nu >_{ion} N_{LyC,int}(1-f_{esc}^{LyC}) + \epsilon L_{nonion}(1-f_{esc}^{LyC}) \tag{35}$$

Where f_{esc}^{LyC} is defined as in Eq. 29, and $f_{esc}^{Ly\alpha}$ is simply defined as the fraction of escaping Lyα photons to the total intrinsic production of Lyα photons,

$$f_{esc}^{Ly\alpha} = \frac{L_{Ly\alpha,esc}}{L_{Ly\alpha,tot}} = \frac{N_{Ly\alpha,esc}}{N_{Ly\alpha,tot}} \tag{36}$$

Note that $N_{LyC,int}$ in this case has three components, one that can contributes to the dust heating, one that ionizes the gas in the HII region and one that just escapes from the region without interacting, i.e.

$$\begin{aligned} N_{LyC,int} &= N_{LyC,dust} + N_{LyC,gas} + N_{LyC,esc} \\ N_{LyC,dust} &= (1-f) N_{LyC,int}(1-f_{esc}^{LyC}) \\ N_{LyC,gas} &= f N_{LyC,int}(1-f_{esc}^{LyC}) \\ N_{LyC,esc} &= f_{esc}^{LyC} N_{LyC,int} \end{aligned}$$

Note also that we assume in Eq. 35 that part of the non-ionizing radiation produced by the stars is also leaking through the dust-free channels, and that the relative magnitude of this leakage is the same as for the ionizing radiation, i.e. it is also given by f_{esc}^{LyC}. In a Case B recombination approximation (Osterbrock 1974) the total Lyα photon production is related to the total production of ionizing photons such that every three produced ionizing photons eventually results in the creation of two Lyα photons. Which means

that we get the following relation between the two in the presence of LyC dust absorption and LyC escape,

$$L_{Ly\alpha,tot} = 0.67 h\nu_{L\alpha} \times f \times N_{LyC,int}(1 - f_{esc}^{LyC}) \tag{37}$$

in terms of the luminosity of ionizing photons, i.e. $L_{LyC} =< h\nu >_{ion} N_{LyC}$, we get with $h\nu_{L\alpha} = 10.2$ eV and with the average energy for LyC photons $< h\nu >_{ion} \sim 15$ eV (Inoue et al. 2000),

$$L_{Ly\alpha,tot} = 0.67 \frac{h\nu_{L\alpha}}{< h\nu >_{ion}} \times f \times L_{LyC,int}(1 - f_{esc}^{LyC}) \approx 0.45 \times f \times L_{LyC,int}(1 - f_{esc}^{LyC}) \tag{38}$$

Eq. 38 in 35 gives

$$\frac{L_{IR}^{dust}}{(1 - f_{esc}^{LyC})} = \left(1 - 0.55 \times f(1 + 0.82 f_{esc}^{Ly\alpha})\right) L_{LyC,int} + \epsilon L_{nonion}$$

The right hand side of this equation is now very similar to Eq. 3 in Inoue et al. (2000). Inoue et al. (2000) assume that the bolometric luminosity in the centre of a typical HII region in a star forming galaxy is dominated by a combination of O and B type stars. Further Inoue et al. (2000) assume that all of the ionizing LyC radiation is produced by the O type stars, and that the non-ionizing radiation is dominated by emission from B type stars. In this scenario Inoue et al. (2000) are able to show using a standard assumption of a Salpeter IMF with a mass range of $0.1 - 100 M_{\odot}$ that the ionizing and non-ionizing luminosity is related to the bolometric luminosity by $L_{LyC} = 0.4 L_{OB}^{bol}$ and $L_{notion} = 0.6 L_{OB}^{bol}$. Eq. 7.1 then becomes

$$\frac{L_{IR}^{dust}}{(1 - f_{esc}^{LyC})} = (0.4 - 0.2 f(1 + 0.82 f_{esc}^{Ly\alpha}) + 0.6\epsilon) L_{OB}^{bol}$$

The total luminosity of the OB stars in a HII region can now be inferred by observing the number of LyC photons through observations of for example the ionized gas,

$$N_{LyC,gas} = f \times N_{LyC,int}(1 - f_{esc}^{LyC}) \tag{39}$$

and by calculating the intrinsic number of LyC photons produced by the assumed distribution of OB stars per, for example, unit solar luminosity. This can be done by assuming a suitable mass and temperature distribution of stars, and then by assuming blackbody spectra for the stars. The emitted power per unit area and wavelength is easily found for a blackbody, and thus this can be applied on the distribution of stars to calculate their emission in a chosen wavelength band, such as the LyC range. A somewhat more involved calculation based on this reasoning has already been done by Inoue et al. (2000) with the result

$$N_{LyC,OB} = 5.63 \times 10^{43} s^{-1} (L_{\odot}^{bol})^{-1} \tag{40}$$

this result and Eq. 39 combined with Eq. 7.1 gives

$$\frac{L_{IR}^{dust}}{(1-f_{esc}^{LyC})} = \frac{(0.4-0.2f(1+0.82f_{esc}^{Ly\alpha})+0.6\epsilon)}{f(1-f_{esc}^{LyC})}\frac{N_{LyC,gas}}{5.6\times10^{43}}$$

If we now also use Eq. 36 to expand the $Ly\alpha$ escape fraction we now have

$$\frac{L_{IR}^{dust}}{(1-f_{esc}^{LyC})} = \frac{(0.4-0.2f(1+0.82(\frac{N_{Ly\alpha,esc}}{N_{Ly\alpha,tot}})+0.6\epsilon)}{f(1-f_{esc}^{LyC})}\frac{N_{LyC,gas}}{5.6\times10^{43}}$$

however, remember that for every three LyC photons two Lyα photons are produced (Eq. 37). Thus we now have

$$\frac{L_{IR}^{dust}}{(1-f_{esc}^{LyC})} = \frac{(0.4-0.2f(1+0.82(\frac{N_{Ly\alpha,esc}}{0.67N_{LyC,int}f(1-f_{esc}^{LyC})})+0.6\epsilon)}{f(1-f_{esc}^{LyC})}\frac{N_{LyC,gas}}{5.6\times10^{43}}$$

and now if we can again express $N_{LyC,int}$ in terms of the LyC photons that contribute to the ionization of the gas, $N_{LyC,gas} = fN_{LyC,int}(1-f_{esc}^{LyC})$, we can see that $(1-f_{esc}^{LyC})$ not unsurprisingly cancels out everywhere. This is natural since we have assumed that the escaping LyC photons escape through dust-free channels and do not in this case interact with the overall system; all of the dust heating must come from the remaining photons. The final equation then becomes:

$$L_{IR}^{dust} = \frac{(0.4-0.2f(1+0.82(\frac{N_{Ly\alpha,esc}}{0.67N_{LyC,gas}})+0.6\epsilon)}{f}\frac{N_{LyC,gas}}{5.6\times10^{43}} \tag{41}$$

This equation can now be used to predict the total IR luminosity of a galaxy, via observations of, $N_{Ly\alpha,esc}$ and $N_{LyC,gas}$. Assuming Case B recombination, the gas temperature T=12100K and the Balmer decrement Hα/Hβ = 2.81 calculated in Section 6.2 we can infer the amount of ionizing photons that is contributing to the ionization of the gas from the recombination coefficients,

$$Q(H^0) = \frac{\alpha_B}{\alpha_{H\beta}^{eff}} \times \frac{L_{H\beta}}{h\nu_{H\beta}} \times \frac{1}{B_d(H\alpha/H\beta)} \tag{42}$$

where $Q(H^0)$ is the intrinsic amount of ionizing photons, $\alpha_B \approx 2.1517\times10^{-13}$ cm^{-3} s^{-1} is the Case B recombination coefficient, $\alpha_{H\beta}^{eff} \approx 2.3578\times10^{-14}$ cm^{-3} s^{-1} is the effective recombination coefficient for Hβ and $B_d(H\alpha/H\beta)$ is the intrinsic Balmer decrement of 2.81 that we calculated previously in Section 6.2. All of the coefficients were obtained by interpolating the data given in (Osterbrock 1989) to the proper electron temperature of $T_e = 12100$ K for Tol 1247-232. If we follow the same unit conventions as in Inoue et al.

(2000) we can now express the estimated intrinsic ionizing photon production responsible for ionizing the gas as

$$N_{LyC,gas} = 9.51 \times 10^{55}[D/(1kpc)]^2[F_{H\alpha}/(ergs^{-1}cm^{-2})] \quad (43)$$

where D is the distance to the galaxy and $F_{H\alpha}$ is the extinction corrected Hα line flux. With this conversion all of the quantities in Eq. 7.1 except f are directly observable through measuring the H-alpha line and by directly measuring the leakage of LyC photons at an appropriate wavelength. The IR luminosity can subsequently be predicted by assuming some value for f. However, more importantly, if we already have a measurement for the total IR luminosity Eq. 7.1 can be used to calculate f. The total IR luminosity can be found from infrared observations at appropriate wavelengths, for example between 60μm and 200μm, by assuming a blackbody emission spectrum of the dust and some estimated dust temperature, typically around 30K. We will be using IRAS observations at 60 μm, exactly like in Inoue (2001), who find the relation

$$L_{IR}/L_{\odot} = 3.50 \times 10^{55}[D/(1kpc)]^2[F_{60\mu m}/(1Jy] \quad (44)$$

This result is obtained by assuming a blackbody spectrum for the dust with T=30 K, normalising the resulting spectrum to match the measurement at 60 μm, and integrating between 8 μm to 1000 μm, which is a decent approximation of the total IR luminosity (Inoue 2001).

We now have all the tools we need to estimate the LyC dust absorption fraction $(1 - f)$. The relevant properties for Tol 1247-232 for performing the calculations are[1]: E(B-V)=0.14 (calculated using a Milky Way extinction law with $R_V = 3.07$), $F_{60\,\mu m} = 0.507\,Jy$, $F_{H\alpha} = 1.06\times10^{-12}$ erg s^{-1} cm^{-2}, $F_{900} = 4.8\times10^{-15}$ erg s^{-1} cm^{-2} Å^{-1} from which we estimate the total flux of LyC photons that escape as $\approx 1.62 \times 10^{-12}$ erg s^{-1} cm^{-2} by assuming a blackbody spectrum with T=33000 K, and finally $F(Ly\alpha)_{esc} = 2.39 \times 10^{-13}$ erg s^{-1} cm^{-2} (corrected for Galactic foreground extinction). This set of data results in an estimate for the LyC dust absorption fraction in Tol 1247-232:

$$(1 - f_{Tol1247-232}) = 0.51$$

Note again that this is the absorption fraction for only the part of the ionizing radiation that is not leaking; the result would not be altered in any way from altering the measured

[1]We present the relevant available observational data on Tol 1247-232 along with our own additions in more detail in Table 1.

LyC leakage, since these photons are assumed to pass through the nebula unhindered through dust-free channels.

The result of a calculation of $(1-f)$ directly using the equations in Inoue (2001) gives the result $(1-f) = 0.48$. Thus not accounting for the $Ly\alpha$ leakage observed from Tol 1247-232 results in an underestimation of the LyC extinction by around 3%. We further find that even if the observed $Ly\alpha$ leakage is multiplied by 5 in the calculations the effect is still very small with only a change of a around one percent in the calculated LyC absorption fraction. Thus it is not extremely critical to account for the $Ly\alpha$ leakage when estimating the LyC dust extinction in the case of Tol 1247-232. However, a calculation of $f_{esc}^{Ly\alpha}$ for Tol 1247-232 using the approximation by Osterbrock (1989) under Case B recombination conditions gives

$$f_{esc}^{Ly\alpha} \approx \frac{F_{Ly\alpha,esc}}{8.7 F_{H\alpha,c}} \approx 3.1\%$$

where $F_{H\alpha,c}$ is the extinction corrected Hα flux and $F_{Ly\alpha,esc}$ is the extinction corrected Lyα flux. Thus our result is not very surprising since the leakage is in any case quite low. However, there are galaxies with much higher $Ly\alpha$ leakages, even approaching 100% for some galaxies at $z \sim 3$ (Atek et al. 2009). If we multiply the leakage in our calculation until we achieve a 75% leakage according to the above approximation we find a 5% increase in our LyC dust absorption estimate (from the $(1 - f_{Tol1247-232}) = 0.51$ value), which would mean that failing to account for the Lyα leakage at all could result in a 8% underestimate of the LyC dust absorption for a galaxy that is otherwise similar to Tol 1247-232 except for a higher Lyα leakage. Such a significant underestimate would be important for calculations of f_{esc}^{LyC}.

Note also that the results of the above LyC dust absorption calculations assume that the LyC photons that escape are passing through channels in the nebula that are completely devoid of dust. An arguably more realistic model for LyC leakage would likely be that the channels through which the LyC photons escape are close to but not completely devoid of dust, since this is typically the case in simulations. The result of neglecting this effect completely is likely a very small overestimate of the LyC dust absorption. However, accounting for this becomes somewhat complicated since we do not know much about the dust-to gas ratio in the hypothetical channels in the nebula where we assume that the LyC photons can escape. Currently the only information we have comes from simulations, e.g. Yajima et al. (2011), Razoumov & Sommer-Larsen (2007) and Gnedin et al. (2008). The simulations indicate that the LyC escapes through channels formed by violent star formation and that both the dust content and the hydrogen content in these

channels is very much lower than in the rest of the nebula. Thus it would very likely be correct to assume only a small absorption fraction for the photons traveling through the channels. However, the available simulations do not specifically measure the effect of dust in the hydrogen-sparse channels where the LyC is escaping – only the total impact of the inclusion of dust in the simulations is reported. The impact of dust can result in a 10 to 50% decrease of the LyC photons (and similar decreases in the escape fraction), depending on the choice of dust-grain sizes in the simulations. Our dust-treatment above results in a 50% decrease of the intrinsic LyC photons, which while high is consistent with the simulations. Note again that the impact of dust in the channels where the LyC photons escape is included in the total estimate of the decrease in the simulations. Thus, since our dust treatment already results in a decrease of the intrinsic LyC photons that is in the upper range of the simulation-based predictions we find it rather unlikely that there would be an additional substantial increase in the LyC dust absorption due to not accounting for dust in the channels. However, since the information we need to fully account for this effect is not currently available we are in the end unable to properly deal with this. Simulations constructed to specifically estimate the impact of dust in the channels would likely have to be constructed. Still, as a rough estimate, and to investigate the effect of including the possibility of dust in the hydrogen- and dust-sparse channels we will assume that the same percentage of LyC photons are absorbed on dust in the channels as in the rest of the nebula. Note that this estimate for the LyC absorption in the channels of the nebula is quite arbitrary, but also probably quite high; all of the simulations agree that when there is a leakage of LyC photons, the leakage happens through very close to empty channels.

We start with our previous model for the infrared luminosity when the Lyα leakage is already taken into account, i.e. Eq. 7.1.

$$L_{IR}^{dust} = \frac{(0.4 - 0.2f(1 + 0.82(\frac{N_{Ly\alpha,esc}}{0.67N_{LyC,gas}}) + 0.6\epsilon)}{f} \frac{N_{LyC,gas}}{5.6 \times 10^{43}}$$

now we also want to add a small contribution to the estimated IR luminosity from the LyC photons that is passing through dust-filled but hydrogen-sparse channels in the nebula,

$$L_{IR}^{dust} = \frac{(0.4 - 0.2f(1 + 0.82(\frac{N_{Ly\alpha,esc}}{0.67N_{LyC,gas}}) + 0.6\epsilon)}{f} \frac{N_{LyC,gas}}{5.6 \times 10^{43}} + (1 - f)L_{LyC,pot} \qquad (45)$$

where $L_{LyC,pot}$ is now defined as the total luminosity of the LyC photons that could

potentially leak without any dust absorption, i.e.

$$L_{LyC,pot} = L_{LyC,esc} + L_{LyC,dust}$$
$$L_{LyC,esc} = fL_{LyC,pot}$$
$$L_{LyC,dust} = (1-f)L_{LyC,pot}$$

which gives

$$L_{LyC,pot} = \frac{1}{f}L_{LyC,esc}$$

If we now substitute this into Eq. 45 we obtain

$$L_{IR}^{dust} = \frac{(0.4 - 0.2f(1 + 0.82(\frac{N_{Ly\alpha,esc}}{0.67N_{LyC,gas}}) + 0.6\epsilon)}{f}\frac{N_{LyC,gas}}{5.6 \times 10^{43}} + \frac{(1-f)}{f}L_{LyC,esc} \quad (46)$$

This equation can now again be used to find the LyC dust absorption fraction $(1 - f)$ using the observed properties of Tol 1247-232, exactly as we did previously using Eq. 7.1. However, note again the this choice of assuming the same LyC absorption fraction for the ionized nebula as for the ionizing photons travelling through the channels where LyC escape is possible is in the end rather arbitrary, as already discussed above. When accounting for the possibility of dust in the hypothetical channels where the LyC is escaping in this way we find the LyC dust absorption fraction

$$(1 - f_{Tol1247-232}^{dusty}) = 0.50$$

which is a 1% drop in the LyC dust absorption compared to the model with dust-free channels. Again a minor effect, at least in the case with the same relative amount of dust absorption in the LyC escape channels as in the rest of the nebula. Also note that the net result of this 1% drop is that our final estimate again becomes closer (within 2%) of the result obtained by directly adopting the formula in Inoue et al. (2001), that does not attempt to account for any of these effects.

Finally we should note that to fully account for large leakages of LyC photons, the entire theoretical framework used to arrive at Eq. 31 would probably need to be re-done, by assuming a Strömgren sphere containing holes or channels where large amounts of LyC photons can escape. However, Leitet et al. (2013) estimate that the LyC escape from Tol 1247-232 is on the order of a few percent, which means that the above equations should be adequate as a first-order approximation. With knowledge of f we can now also proceed to re-calculate the LyC escape fraction directly using our extinction corrected Hα data.

7.2. The absolute LyC escape fraction

Without any LyC dust absorption the LyC escape fraction is given by Eq. 27,

$$f_{esc}^{LyC} = \frac{N_{LyC,esc}}{N_{LyC,esc} + N_{LyC,gas}}$$

we have shown in the previous section that all of the quantities on the right-hand side of this equation can be inferred directly from observations of the leaking LyC photons and the Hα line strength. A calculation using the above equation and the relevant data from Table 1 results in the absolute escape fraction with no LyC dust absorption,

$$f_{esc}^{LyC,f=1} = 10.2\%$$

However, since both simulations and observations indicate that a substantial amount of the intrinsically produced LyC photons are absorbed on dust before ever being able to ionize hydrogen we must incorporate LyC dust absorption into the above formula, which is then given by Eq. 29

$$f_{esc}^{LyC} = \frac{N_{LyC,esc}}{N_{LyC,esc} + N_{LyC,gas} + N_{LyC,dust}}$$

However, $N_{LyC,esc}$, $N_{LyC,gas}$, $N_{LyC,dust}$ and the total intrinsic LyC production $N_{LyC,int}$ are with our definitions of f and f_{esc}^{LyC} related by

$$\begin{aligned}
N_{LyC,int} &= N_{LyC,dust} + N_{LyC,gas} + N_{LyC,esc} \\
N_{LyC,dust} &= (1-f)N_{LyC,int}(1-f_{esc}^{LyC}) \\
N_{LyC,gas} &= fN_{LyC,int}(1-f_{esc}^{LyC}) \\
N_{LyC,esc} &= f_{esc}^{LyC}N_{LyC,int}
\end{aligned}$$

which means that we can relate $N_{LyC,gas}$ and $N_{LyC,dust}$ to each other using $N_{LyC,int}$,

$$\begin{aligned}
N_{LyC,int} &= \frac{N_{LyC,gas}}{f(1-f_{esc}^{LyC})} \\
N_{LyC,dust} &= (1-f)\frac{N_{LyC,gas}}{f(1-f_{esc}^{LyC})}(1-f_{esc}^{LyC})
\end{aligned}$$

and since $(1-f_{esc}^{LyC})$ cancels we get

$$N_{LyC,dust} = (1-f)\frac{N_{LyC,gas}}{f} \tag{47}$$

Thus, with the inclusion of LyC dust absorption, the absolute escape fraction f_{esc}^{LyC} can be expressed as

$$f_{esc}^{LyC} = \frac{N_{LyC,esc}}{N_{LyC,esc} + N_{LyC,gas} + \frac{1-f}{f}(N_{LyC,gas})} \tag{48}$$

note that with $f = 1$ we retrieve Eq. 27. Using the data in Table 1 we find

$$f_{esc}^{LyC,f=0.51} = 4.8\%$$

However, this result still assumes that the LyC escape happens through dust free channels. If part of the escaping LyC photons would also be attenuated by dust when they travel through the hydrogen-sparse channels in the nebula we must add yet another term to the estimate for the total intrinsic amount of LyC photons to properly estimate the LyC escape fraction, i.e.

$$f_{esc,dusty}^{LyC} = \frac{N_{LyC,esc}}{N_{LyC,esc} + N_{LyC,gas} + \frac{1-f}{f}(N_{LyC,gas}) + \frac{1-f_2}{f_2}(N_{LyC,esc})} \tag{49}$$

Where (1-f_2) describes the dust absorption of the LyC photons traveling through the hydrogen-sparse channels in the nebula. Note that this fraction in theory can be both higher and lower than the absorption in the rest of the nebula. However, we assume $f_2 = f$ (see the previous section). The effect of including this term on the calculated escape fraction is a small decrease to

$$f_{esc,dusty}^{LyC,f=0.50} = 4.6\%$$

All of the above results were calculated by only using the Fitzpatrick (1999) extinction law with $R_v = 3.07$ for a modelled age of 30 Myr, and should thus not be seen as our definitive estimate of f_{esc} for Tol 1247-232. We are merely illustrating the effect of including the various forms of LyC dust absorption above. We will make a proper best-estimate for the absolute escape fraction while accounting for the full range of extinction laws and the full range of uncertainties in our calculations in the following section. However, we will first slightly modify the equations above to work with fluxes instead of luminosities and total amounts of photons in order to match the formalism used by Bergvall et al. (2006) for the calculation of f_{esc} in the other local LyC leaking galaxy Haro 11. The benefit of doing this is of course that the distance dependencies are removed, which is possible since all of the terms on the right hand side of Eq. 49 is determined from the observed flux and the standard flux to luminosity relation $L = 4\pi D^2 F$, where D is the distance. The formula used by Bergvall et al. (2006), which is based on the formalism introduced by Deharveng et al. (2001) is

$$f_{esc}^{LyC} = \frac{F_{900,obs}}{F_{900,obs} + 8.56 \times 10^{11-k_1} F_{H\alpha}} \tag{50}$$

where $F_{900,obs}$ is the observed flux at 900 Å given in erg s^{-1} cm^{-2} Å^{-1}, $F_{H\alpha}$ is the observed extinction corrected Hα flux given in erg s^{-1} cm^{-2}, and the conversion term $8.56 \times 10^{11-k_1} F_{H\alpha}$ converts the Hα flux to an estimated flux at 900 Å, and is roughly the equivalent of our calculation in Eq. 43, and also assumes Case B recombination. However, a model dependent conversion factor, k_1, defined as

$$k_1 = log_{10}(\frac{N_{LyC,gas}}{L_{900,abs}}) \tag{51}$$

is introduced. The parameter k_1 relates the amount of ionized photons responsible for ionizing the gas to the expected luminosity at $\lambda = 900$ Å. Thus the full conversion term $8.56 \times 10^{11-k_1} F_{H\alpha}$ effectively converts the observed Hα flux measured in erg s^{-1} cm^{-2} to an estimated intrinsic flux at $\lambda = 900$ Å measured in erg s^{-1} cm^{-2} Å^{-1}, which subsequently allows calculation of f_{esc} without the need to introduce luminosities and the distance to the galaxy. The conversion factor has been constrained by Bergvall et al. (2006) who use spectral synthesis to investigate a range of star formation scenarios and find the average conversion factor $k_1 = 13.235$. which we will also adopt here. Note that the above formula again does not take the LyC dust absorption into account. We will use a modified version of Eq. 50 that matches our results that include both the LyC dust absorption terms that we derived above. We have also recalculated the conversion term to suit the electron temperature in Tol 1247-232. The result of our corrections is the following equation

$$f_{esc}^{LyC} = \frac{F_{900,obs}}{F_{900,obs} + 7.95 \times 10^{11-k_1} F_{H\alpha} + \frac{1-f}{f} 7.95 \times 10^{11-k_1} F_{H\alpha} + \alpha \frac{1-f}{f} 7.95 \times 10^{11-k_1} F_{900,obs}} \tag{52}$$

where α is either set to $\alpha = 1$ to include the our approximation of the impact of dust inside the channels where the LyC photons escape, or $\alpha = 0$ to assume dust-free channels. Note that the method we use to find the LyC dust absorption fraction (1-f) also depends on the choice of α. With $\alpha = 0$ requiring Eq. 7.1 and $\alpha = 1$ requiring Eq. 46.

7.3. The Lyman Continuum escape fraction of Tol 1247-232

To make a best-estimate of the absolute LyC escape fraction of Tol 1247-232 we will consider the full range of extinction laws resulting in an R_V range of $R_V = 2.5$ to $R_V = 4.85$. We will also consider the effect of LyC dust absorption in the dust-free channels case and in the case with dust-filled channels where the LyC is escaping. Thus we adopt Eq. 52 with both $\alpha = 0$ and $\alpha = 1$. However, since our treatment of the dust-filled case ($\alpha = 1$) is merely a rough approximation we will put less weight on these results than on the ($\alpha = 0$) results in our subsequent calculations. We adopt the LyC escape flux $F_{900} = 4.8 \times 10^{-15}$ erg s^{-1} cm^{-2} Å^{-1}, which is a recalculation of the value given in Leitet et al. (2013). The flux at 900 Å in Leitet et al. (2013) was calculated using the Cartledge et al. (2005) extinction law for the SMC based on the somewhat outdated galactic line of sight extinction estimate $A_v = 0.27$ by Schlegel et al. (1998). We adopt the empirical law by Gordon et al. (2009) to correct the leaking LyC flux for the Galactic foreground extinction $A_v = 0.237$ measured by Schlafly & Finkbeiner (2011). The result of the f_{esc}^{LyC} calculations performed as described above is shown in Figure 23. All of the results in Figure 23 is based on resolved extinction corrections calculated using our iterative method described in Section 6.4.

In the bottom left panel of Figure 23 we show the fraction of the intrinsic LyC photons that are absorbed on dust, and in the top right panel we show the colour excess, $E(B-V)$, that goes into the calculation of the dust absorption. Note that the Yggdrasil model predicts both systematically lower fluxes and lower values for $E(B-V)$ for low ages < 10 Myr. The result of this is that more of the infrared luminosity must be explained by LyC dust absorption. This is clearly seen in the bottom left panel of Figure 23. Note that higher LyC dust absorption in turn lowers the absolute escape fraction calculations shown in the bottom right panel of the figure. Without accounting for the dust absorption of LyC photons at all the result would be that much higher escape fractions are predicted for the extremely young ages of less than 10 Myr, since the estimated intrinsic LyC photon production will be lower due to the lower predicted Hα line strength for these ages. Thus, the inclusion of LyC dust absorption not only systematically lowers the predicted escape fraction (as already shown in the previous section) but also acts as a balancing effect on the predicted escape fractions as a function of the modelled age. The same can be seen if we consider the fluxes predicted by the various extinction laws and R_V values. The lowest and highest predicted flux differ by roughly 30% as already discussed, however, this only translates to a 17% difference in the predicted escape fraction. This is again due to the balancing effect of the LyC dust absorption, if the predicted Hα flux is very high this will

result in a lower LyC dust absorption needed to explain the observed infrared flux, which in turn predicts higher escape fractions, and vice versa if the flux is low.

To make a final best-estimate for the escape fraction of Tol 1247-232 we take the average of the escape fractions predicted by the Milky Way law with $R_V = 3.07$ and the two laws giving the most extreme escape fraction values. Note that we can take this average over the entire range of ages between 1 Myr to 100 Myr, since the escape fraction is very insensitive to the modelled age. Note that for this calculation we use a weighted average of the the $\alpha = 1$ and $\alpha = 0$ results for each extinction law, with the $\alpha = 1$ case given a 50% lower weight than the $\alpha = 0$ case, since the $\alpha = 1$ results are very approximate. However, since the effect of including our estimate of the impact of dust in the channels where the LyC photons escape is small (generally less than 1% as shown in the previous section), this does not really affect the final result in any meaningful way. To estimate the final error in this calculation we have performed Monte Carlo simulations again based on the two extinction laws resulting in the highest and lowest escape fractions in Figure 23. These simulations take the given uncertainties in all of the ingoing parameters into account, which is, e.g. 10% for the infrared measurement at 60 μm, 5% on our Hα flux measurements, 18% on the LyC measurement, and 12.5% on the Lyα leakage measurement. The result of these simulations is the same for both laws, and a 15% uncertainty in the escape fraction is predicted. This uncertainty is added on top of the two most extreme cases in the bottom right panel of Figure 23 to arrive at our final estimate of the escape fraction, shown in Figure 24. The shaded area represents the maximal uncertainty interval, constructed as above, and the error bars represent the standard deviation at each calculated model-age of the MW, SMC, and Calzetti et al. (2000) (RV = 4.85) extinction laws when the calculation resulting in the bottom right panel of Figure 23 is run a large amount of times with the uncertainties in all of the ingoing fluxes and parameters are applied randomly in the calculations. However, to be safe we will use the larger error indicated by the shaded area as our final estimate for the uncertainty in the absolute escape fraction of Tol 1247-232, which is

$$f_{esc}^{LyC} = 4.9 \pm^{1.2}_{1.1} \,\% \tag{53}$$

This is the main result of this project. Note that we are finding a somewhat higher escape fraction than what was is found by Leitet et al. (2013), which is $f_{esc}^{LyC} = 2.4 \pm^{0.9}_{0.8} \,\%$. However, this is not very surprising, since we are using a recalculated flux measurement at 900 Å, which is somewhat higher than the one used by Leitet et al. (2013). If we adopt $F_{900} = 4.4 \times 10^{-15}$ erg s^{-1} cm^{-2} Å^{-1} to match the previous estimate we find that our average escape fraction drops to 4.3%, which makes our measurements compatible when

the full error intervals of both measurements are considered. However, the usage of the empirical Gordon et al. (2009) extinction law for the Milky Way to correct the LyC flux should be a more correct treatment than what is used in Leitet et al. (2013), who adopt an extinction law measured for the SMC to correct for the Galactic foreground extinction. Thus we conclude that the escape fraction in Tol 1247-232 very likely is somewhat higher than previously reported by Leitet et al. (2013). Note that this result and all of the calculations outlined here assume that the LyC leakage is caused by young and massive stars in the galaxy, and not by some other source, such as a strongly ionizing AGN. The presence of an AGN in Tol 1247-232 is investigated in the following section with the help of [OIII] and Hβ extinction corrected imaging.

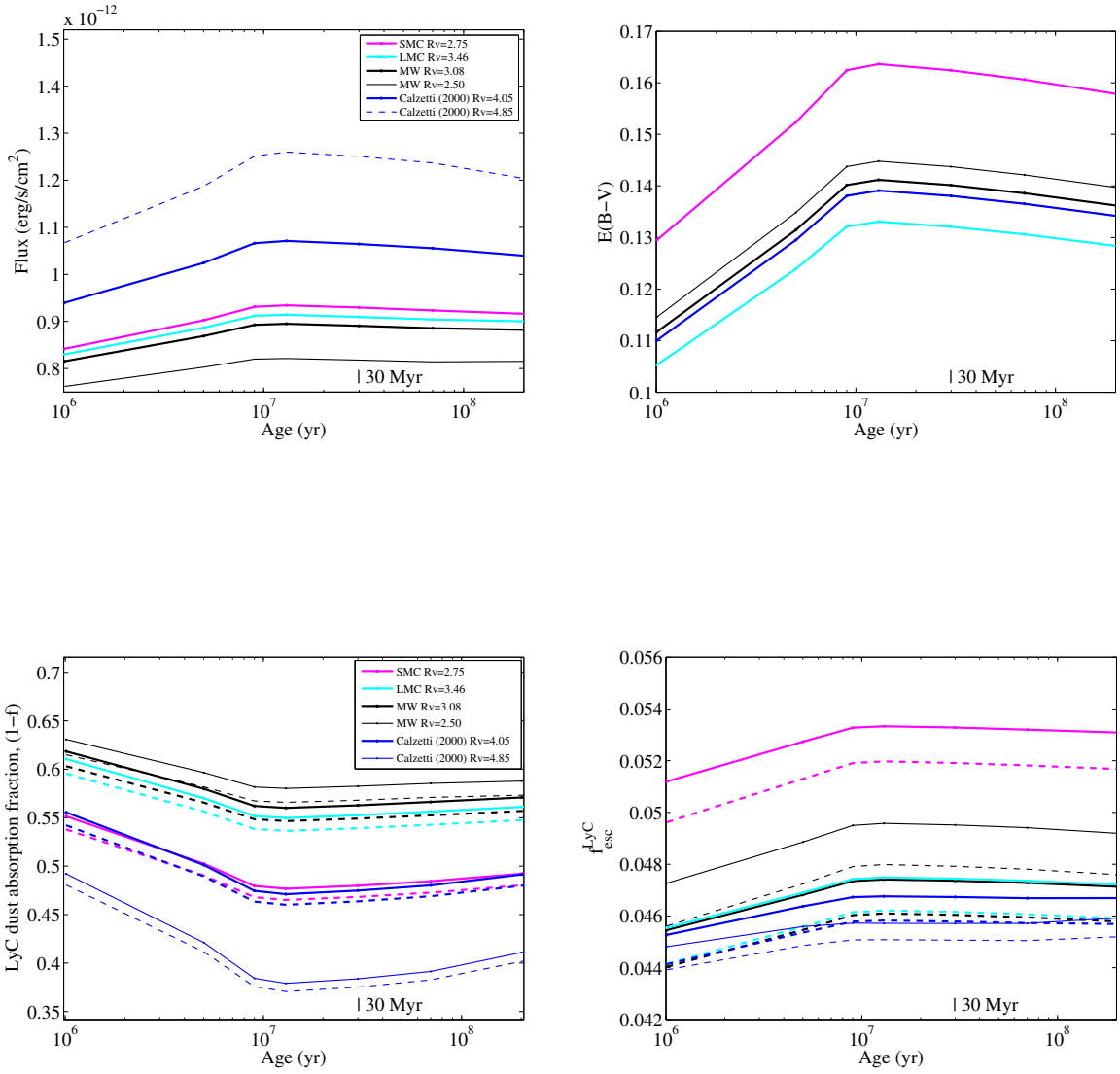

Fig. 23.— The absolute LyC escape fraction and dust absorption fraction of Tol 1247-232, calculated using the data in Table 1 and our extinction corrected Hα fluxes shown in Figure 21. The solid lines in the figures represent the dust-free channel scenario ($\alpha = 0$), and the dotted lines represents calculations for $\alpha = 1$ where the presence of dust is allowed in the hydrogen-sparse channels where the LyC photons are assumed to escape. The top left panel shows the extinction corrected Hα flux. The top right panel shows the colour excess $E(B-V)$ that goes into the calculation of the dust absorption. The bottom left panel shows the LyC dust absorption fraction, and the bottom right panel shows the absolute escape fraction. The individual panels are further discussed in Section 7.3.

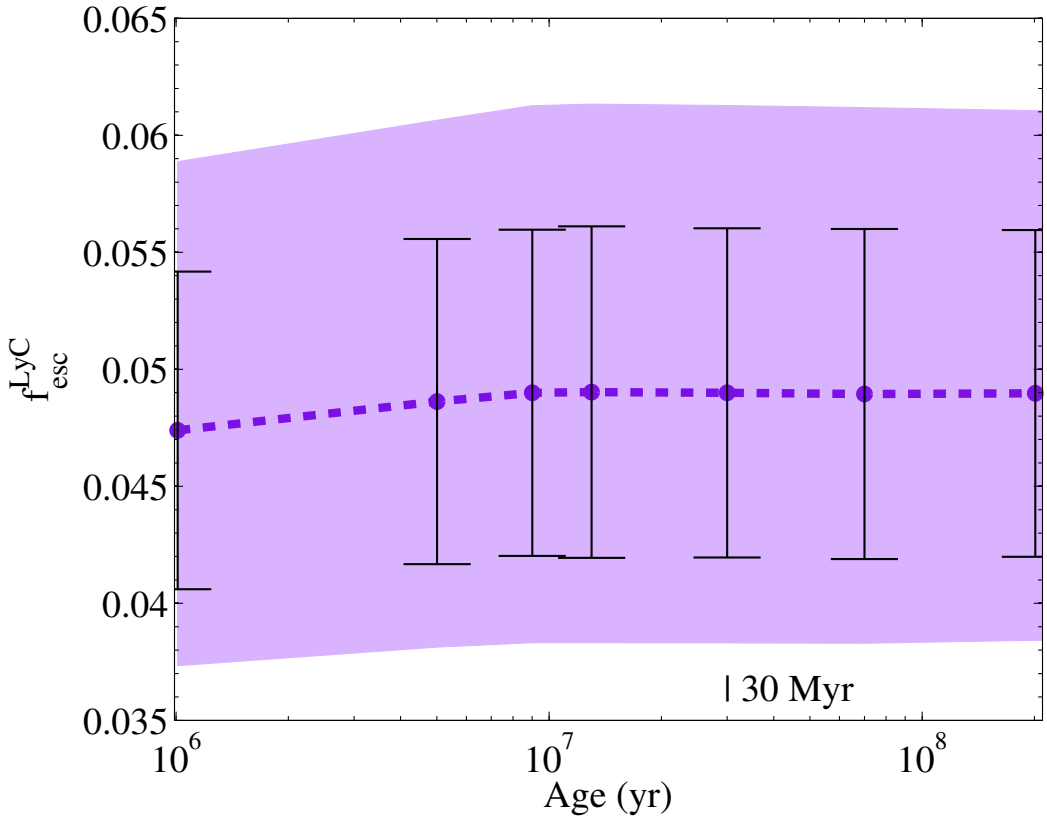

Fig. 24.— The absolute LyC escape fraction of Tol 1247-232 including estimated errors. The dashed line is the average of the highest (SMC) and lowest (Calzetti et al. (2000) with $R_V = 4.85$) f_{esc}^{LyC} results from the bottom right panel of Figure 23. The errorbars represent the standard deviation of f_{esc}^{LyC}in each modelled age, calculated from the SMC, LMC and Calzetti et al. (2000) ($R_V = 4.85$) extinction laws using a Monte Carlo simulation where all of the fluxes and parameters used for the calculations are allowed to vary randomly within their respective uncertainties. The shaded area represents the maximal uncertainty in the average calculated by directly applying the maximal estimated uncertainties for each age ($\approx 15\%$) on the lowest and highest results in the bottom right panel of Figure 23.

8. An [OIII]λ5007 emission map of Tol 1247-232

Using the [OIII]λ5007 (hereafter [OIII]) continuum subtracted line image and the continuum subtracted Hβ image we have calculated maps of log([OIII]/Hβ) in Tol 1247-232. We display an extinction corrected [OIII] map in the top panel of Figure 25. Note that since the [OIII] and Hβ lines are close in wavelength, the effect of the extinction correction is small. However, we find that there is an average decrease of around 0.05 in the individual log([OIII]/Hβ) values. The bottom panel of Figure 25 shows the average log([OIII]/Hβ) ratio as a function of modelled age. For ages between 10 Myr to 100 Myr the average is approximately given by log([OIII]/Hβ)=0.72. This agrees with previous estimates based on the emission line data by Terlevich et al. (1991).

The [OIII] emission line is a measure of the ionization level in the galaxy. Strongly ionizing sources, such as an AGN are expected to give very high values of log([OIII]/Hβ). Thus, the possibility of an AGN contribution to the detected LyC flux leakage of Tol 1247-232 can be investigated using the [OIII] map. Typically the importance of the AGN contribution is discussed in terms of the Baldwin, Phillips & Terlevich, BPT (Baldwin et al. 1981) diagaram (see also Stasińska et al. (2006) for an updated review). Essentially the BPT diagram compares log([OIII]/Hβ) to the metallicity of the galaxy, typically estimated by another line ratio such as [NII]/Hα, or [SII]/Hα. The BPT diagram is useful in this context since purely star forming (SFR) galaxies, and galaxies with AGN activity is rather clearly separated in the diagram, with SFR galaxies generally having much lower ionization levels.

The average metallicity in Tol 1247-232 estimated from the extinction corrected [NII] and Hα line (Terlevich et al. 1991) gives log([NII]/Hα) ≈ -1.25. This is a very low metallicity, as expected for a BCG such as Tol 1247-232. Note that AGNs in very low metallicity objects are expected to be very unlikely, however, not impossible (Groves et al. 2006). Regardless, for the calculated average metallicity, significant AGN activity would require an average log([OIII]/Hβ) $\gtrsim 1$ for the entire galaxy. See e.g. Figure 1 in Stasińska et al. (2006). Still, Figure 25 does show some interesting structure in the [OIII]/Hb ratio image. The regions with the highest ionization level is located in the centre of the galaxy where we have the highest flux. In the [OIII] map the values reach approximately ratio of log([OIII]/Hβ) ≈ 0.85, which while high is not enough to indicate an AGN. Further, the average over the entire galaxy, calculated by comparing the total flux in [OIII] and Hβ using our resolved line images and resolved extinction map, gives log([OIII]/Hβ) ≈ 0.72 which is as already mentioned consistent with earlier results putting the galaxy in the

SFR regime in the BPT diagram.

More recent work on the BPT diagram placement of galaxies also introduces a mixed SFR/AGN regime into the diagram, see e.g. Lara-López et al. (2010). Galaxies in this regime are thought to have comparable contributions to the ionization level from the star formation and from an AGN. However, even in this updated picture we would not place Tol 1247-232 in the mixed regime. This is because for such low metallicities as what is observed in Tol 1247-232 the mixed regime is expected to overlap the pure AGN regime, which in effect means that a log([OIII]/Hβ) ratio of very close to 1 is still needed. Thus we conclude that the regions that do show very high ionization are likely not a result of an AGN, but a result of a high concentration of very young massive stars. Both Terlevich et al. (1993) and Schaerer et al. (1999) conclude that Tol 1247-232 has the properties of a Wolf-Rayet galaxy. In the presence of massive Wolf-Rayet stars it is expected that regions similar to Strömgren spheres of very high ionization is formed, which is also exactly what we observe in the central region of Tol 1247-232. Figure 25 shows several separate circular regions where the ionization gradually increases with decreasing distance to the centre of the regions. These regions are likely centred on massive clusters of young stars. We will further investigate the central high ionization region using colour maps in the visual and infrared in Section 9, where we show that the BVRIHJKs photometry of Tol 1247-232 is compatible with the above picture, with Tol 1247-232 showing similar colours as the Wolf-Rayet galaxies investigated by e.g. López-Sánchez & Esteban (2008). Finally we note that the star formation in Tol 1247-232 has previously been investigated in both X-ray and radio (Rosa-González et al. 2007; Rosa González et al. 2009), also without any indication of an AGN. In conclusion, we find that it appears unlikely that there is an AGN contribution in Tol 1247-232.

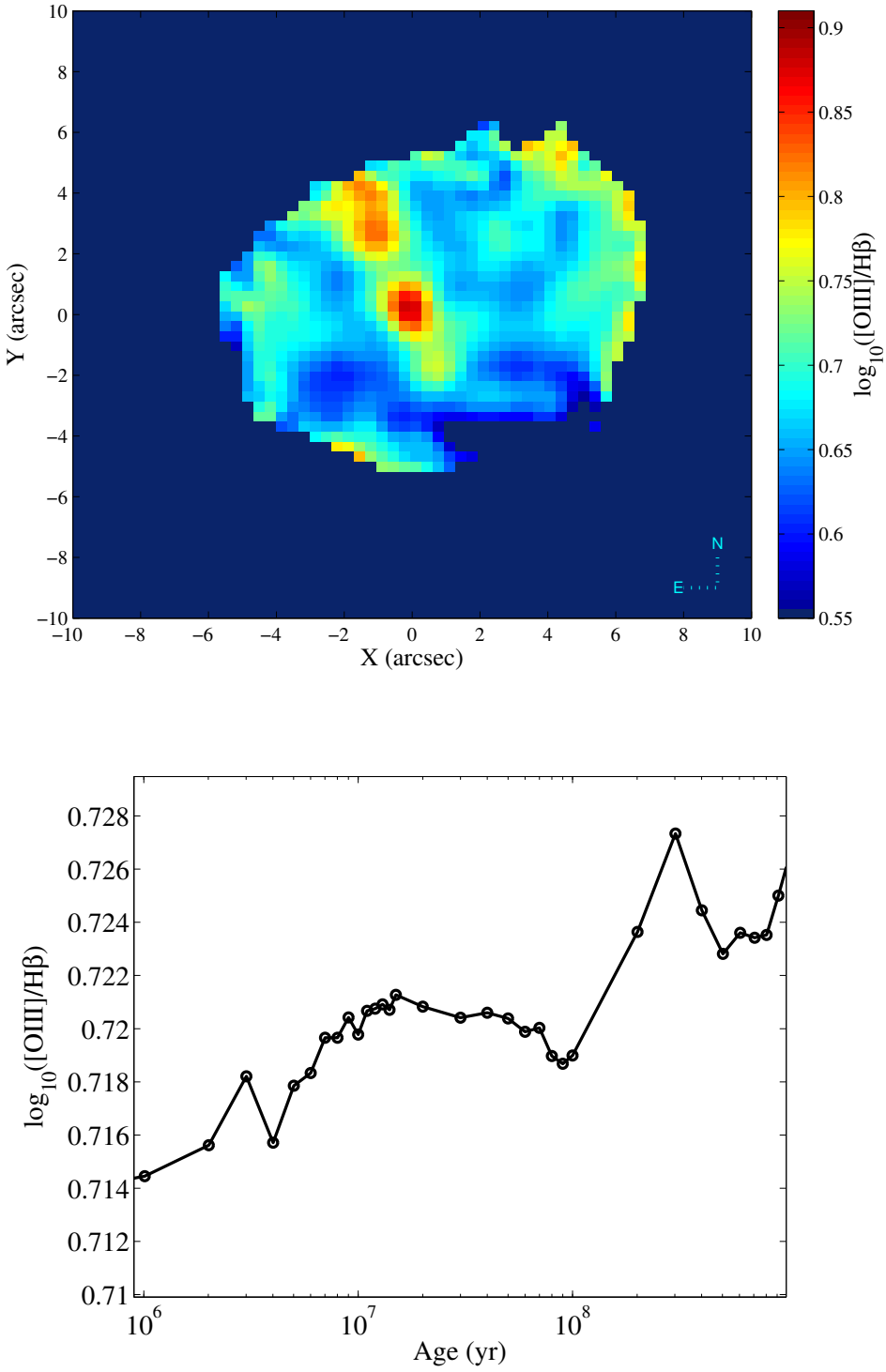

Fig. 25.— Top: A $\log_{10}$(OIII/Hβ) map of the ionization level in Tol 1247-232. The central regions show high ionization, with approximately $\log_{10}$(OIII/Hβ)=0.85. Bottom: the average $\log_{10}$(OIII/Hβ) ratio as a function of modelled age for the dominate burst of star formation. The average is approximately $\log_{10}$(OIII/Hβ)=0.72 in the 10 Myr to 100 Myr range.

9. BVRIJHKs photometry and colour maps of Tol 1247-232

We have performed broad band photometry on Tol 1247-232 using B, V, R, and I filters. The resulting integrated magnitudes are displayed in Table 2 along with previous J, H and Ks near infrared photometry of the galaxy from 2MASS. The integrated magnitudes can of course be used to calculate the integrated colours of the galaxy, which is displayed in Table 3. The uncertainties reported in Table 2 and Table 3 are estimated from the statistical uncertainties propagated through the reductions using Monte Carlo simulations, from investigating the spread in the calculated zero-points in the standard-star fields and from manually assessing the general quality of the images. The result is roughly a 5% error in the B, V and R images, and a 10% error in the I image. The higher error in the I-band image is a result of rather strong contamination on the galaxy from light from a nearby star in all of the dithered exposures in this filter. The errors in the J, H and Ks photometry are the errors reported in 2MASS.

In addition to performing photometry on our calibrated broad band images, we have constructed colour maps in B-V, V-R, V-I, V-J, J-H, J-Ks and H-Ks. These maps are presented in Figures 26, 27, 28, 34, 31, 32 and 33 respectively. In the top panels of the BVRI colour figures we show maps corrected for the Galactic foreground extinction $A_v = 0.237$ and in the bottom panels of the BVRI colour figures we show maps corrected for both the foreground extinction and the intrinsic extinction in Tol 1247-232. We correct for the intrinsic extinction using an extinction map calculated with $R_V = 3.07$ and a Balmer decrement of Hα/Hβ=2.81. The map is subsequently applied to the broad band images using the Calzetti et al. (2000) extinction law for starbursts with $R_V = 4.05$ and $E_s(B-V) = 0.44E_{HII}(B-V)$ (see Section 6.3). For the NIR colours we only display extinction corrected (Galactic and intrinsic) maps, since the effect of the extinction corrections are very small in the near infrared regime. We find that the observed visual and near-infrared colours are best described by a galaxy with a substantial contribution from very young and massive stars. The observed colours are generally compatible with the Wolf-Rayet galaxies investigated by López-Sánchez & Esteban (2008), however, an excess is observed in the Ks filter, resulting in a H-Ks colour (H-Ks≈0.7, extinction corrected) that deviates substantially from the results in López-Sánchez & Esteban (2008) (typically H-Ks=0.1 to H-Ks=0.2).

A somewhat more robust analysis of the observed colours in Tol 1247-232 can be performed with the help of spectral synthesis. For this purpose we again use a simple continuous burst model with a burst duration of 100 Myr. However, in this case the

ionization level in the model is adjusted to match the observed ionization level in the galaxy, i.e. log([OIII]/Hβ)=0.72. In this way we make a crude model of a Wolf-Rayet galaxy where the massive young Wolf-Rayet stars give rise to areas of very high ionization, as shown in Figure 25. The Yggdrasil model is again used, however we are in this case using both SB99 spectra and spectra from the Zackrisson et al. (2001) model as input. This is because the ionization level cannot as easily be matched to the observed level with SB99 based input spectra as for Zackrisson et al. (2001) based spectra. For an age of 30 Myr we measure log([OIII]/Hβ)=0.5 for the SB99 input spectra and log([OIII]/Hβ)=0.75 for the Zackrisson et al. (2001) spectra. Note that the ionization level in the Zackrisson et al. (2001) input spectra is very well matched to the observed level. Note also that the transmission profiles of the ESO NTT/EMMI BVRI and the NOT/NOTCAM HJKs filters are convolved with the modelled spectra in the Yggdrasil model to allow easy comparison with the observed colours.

We show the difference between the modelled colours and the observed integrated colours as a function of modelled age in Figure 29. The top panel shows the differences calculated with the Yggdrasil model based on SB99 spectra and the bottom panel shows the differences calculated with the Yggdrasil model based on Zackrisson et al. (2001) input spectra. Especially note that when the ionization is matched to the observed level the modelled colours are compatible with the observed colours for modelled ages that are in very good agreement with our previous result in Section 4 where we found that the Hα and Hβ emission lines in the galaxy indicate an age of 30 Myr for the dominating burst of star formation in the galaxy. When the errors in the broad band photometry are taken into account the modelled colours can be interpreted as matching the observed colours for ages as low as 35 Myr. However, the best fit is achieved for ages between 60 Myr to 80 Myr. Note that this slightly higher age is an expected result – the impact of older stars from previous star formation events is expected to be bigger for the broad band colours that are dominated by the stellar continuum emission than for the narrow band data previously investigated in Section 4.

We have also performed the spectral analysis explained above separately on only the central region in the galaxy where we observe the highest ionization levels (as shown in Figure 25) and where we subsequently expect the young and massive Wolf-Rayet stars to dominate. The results are very similar to those displayed in Figure 29 for the integrated colours, however, in this case the best match between the Yggdrasil model with the Zackrisson et al. (2001) based input spectra and the observed colours is achieved for an age of 35 Myr. This shows that the central highly ionized region appears to be especially

dominated by very young and massive stars. Note also that the observed colours are matching the model predictions surprisingly well when we consider that we are only modelling a single continuous burst of star formation, and are not taking any possible other underlying stellar populations into account. We conclude that the emission in the visual regime in Tol 1247-232 very likely is dominated by a very young population of stars with an age of less than 100 Myr. Note also that if there was a substantial AGN contribution in the galaxy we would not expect to be able to show such good agreement between the observed colours and the simple continuous burst model predictions.

We compare the observed NIR colours with the Yggdrasil model based on SB99 spectra in Figure 30. The SB99 spectra are chosen for this calculation even though the ionization level cannot be matched to the observed level with these spectra. However, we find that we are unable to match the observed NIR colours at all using the Zackrisson et al. (2001) input spectra. The observed Ks near infrared excess can be explained by the SB99 based model as contribution from extremely young stars with ages less than 10 Myr. And, we in fact find that if the errors in all of the NIR colours are taken into account the V-J, J-H and H-Ks colours are compatible with a modelled age of 10 Myr. However, this match is not very good, and the full errors in the H-Ks and V-J colours are required. We are unable to find a match between the model and the observed colours at all for older ages than 10 Myr. This is perhaps a surprising result, since one would naively expect the near infrared emission to be dominated by continuum emission from the older stars in the galaxy. It is possible that our model is too simplified to adequately match the NIR colours, since we are only modelling a single continuous burst population. However, we note that the observed J-H and H-Ks colours and colour maps are compatible with the observed colours in for example the grand-design spiral galaxies investigated by Grosbøl & Dottori (2012) who find that e.g. NGC7424 shows very similar colours with J-H=0.25 and H-Ks=0.7 for a number of clusters in the spiral arms of the galaxy where substantial star formation is happening. Thus we still find that the near infrared colours appear to be compatible with Tol 1247-232 being a starburst galaxy without an AGN.

In conclusion, we find that both the visual and near infrared colours of Tol 1247-232 are compatible with the galaxy being a starburst undergoing substantial star formation of massive Wolf-Rayet stars. This conclusion is in agreement with Terlevich et al. (1993) who find that the visual spectra of Tol 1247-232 shows features indicative of the presence of a substantial amount of Wolf-Rayet stars and with Schaerer et al. (1999) who has previously classified Tol 1247-232 as a Wolf-Rayet galaxy based on the spectral features of the galaxy. Note also that this is precisely the conditions that are shown by simulations

to be needed in a galaxy to allow LyC escape. We cannot conclusively show where the LyC escape is happening from the observed colours, but based on the colours and our constructed spectral synthesis model of a Wolf-Rayet galaxy we find that the most likely candidate region is the central region of the galaxy that shows the highest ionization level and likely the highest concentration of massive young stars.

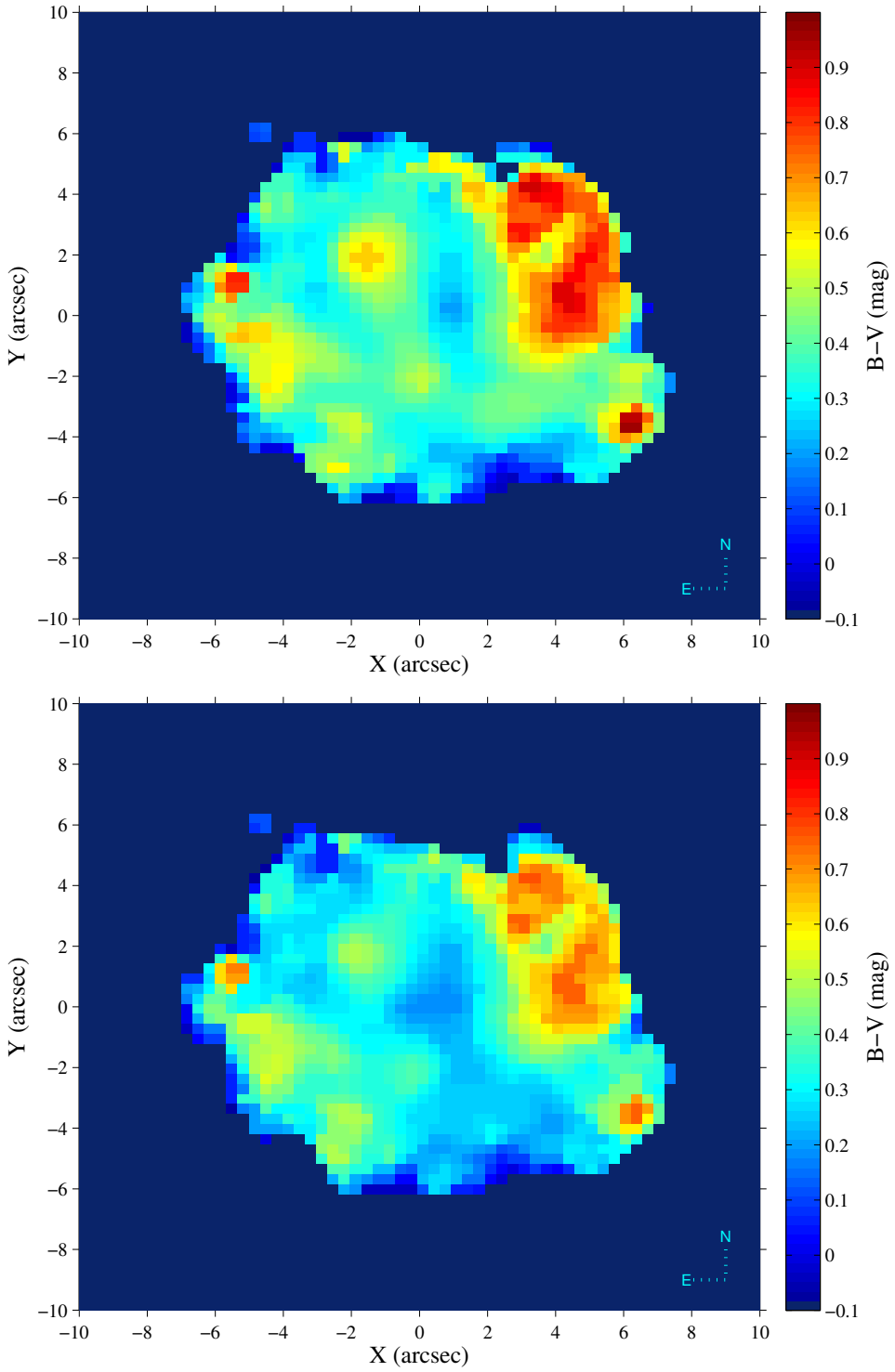

Fig. 26.— B-V magnitude colour maps of Tol 1247-232. Top: B-V colour map corrected for the Galactic foreground extinction $A_v = 0.237$ but not for the intrinsic extinction in Tol 1247-232. Bottom: B-V colour map corrected for both the Galactic foreground extinction $A_v = 0.237$ and the intrinsic extinction in Tol 1247-232 using the Calzetti et al. (2000) extinction law for starbursts with $R_V = 4.05$.

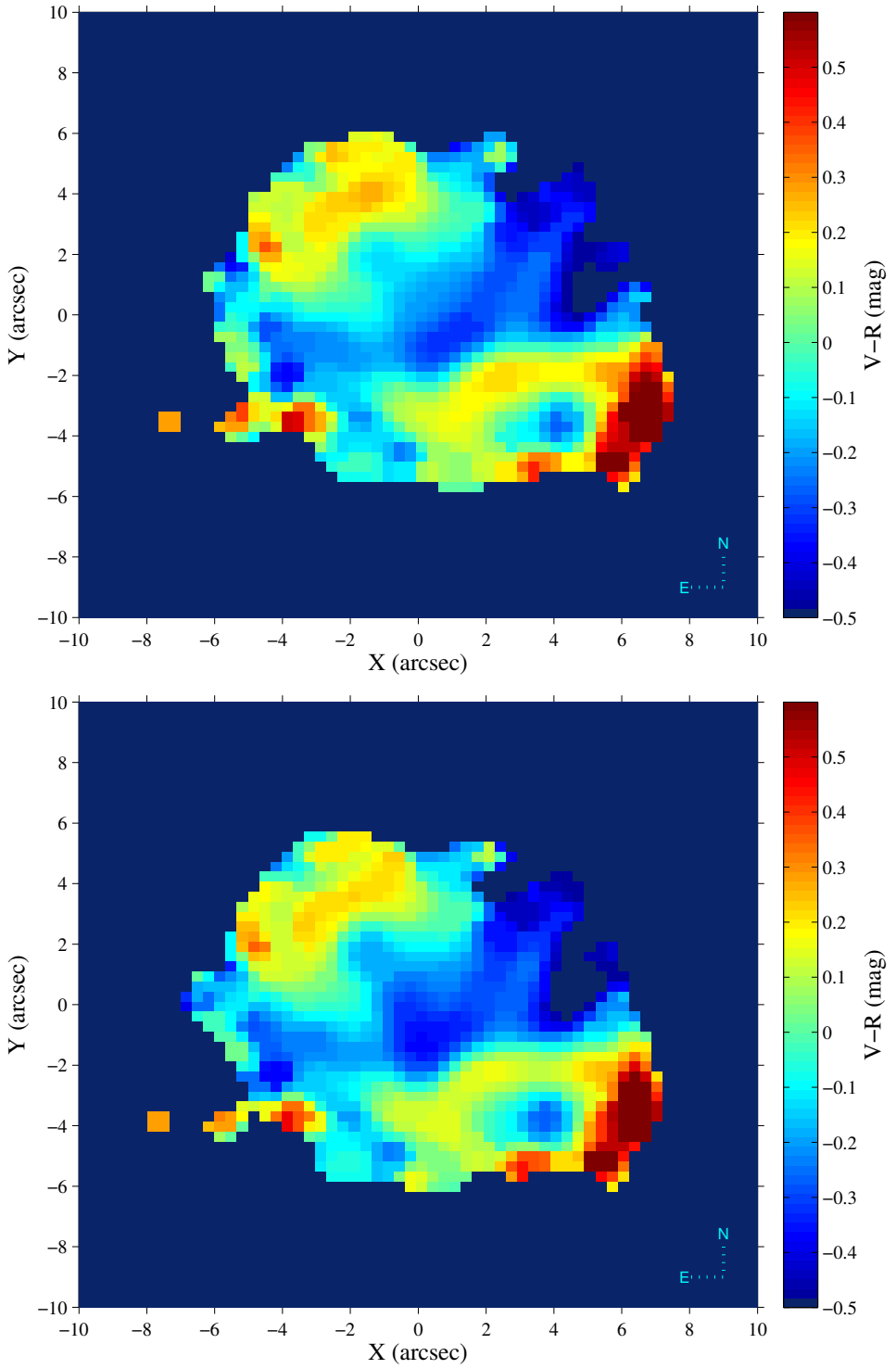

Fig. 27.— V-R magnitude colour map. Top: V-R colour map corrected for the Galactic foreground extinction $A_v = 0.237$ but not for the intrinsic extinction in Tol 1247-232. Bottom: V-R colour map corrected for both the Galactic foreground extinction $A_v = 0.237$ and the intrinsic extinction in Tol 1247-232 using the Calzetti et al. (2000) extinction law for starbursts with $R_V = 4.05$.

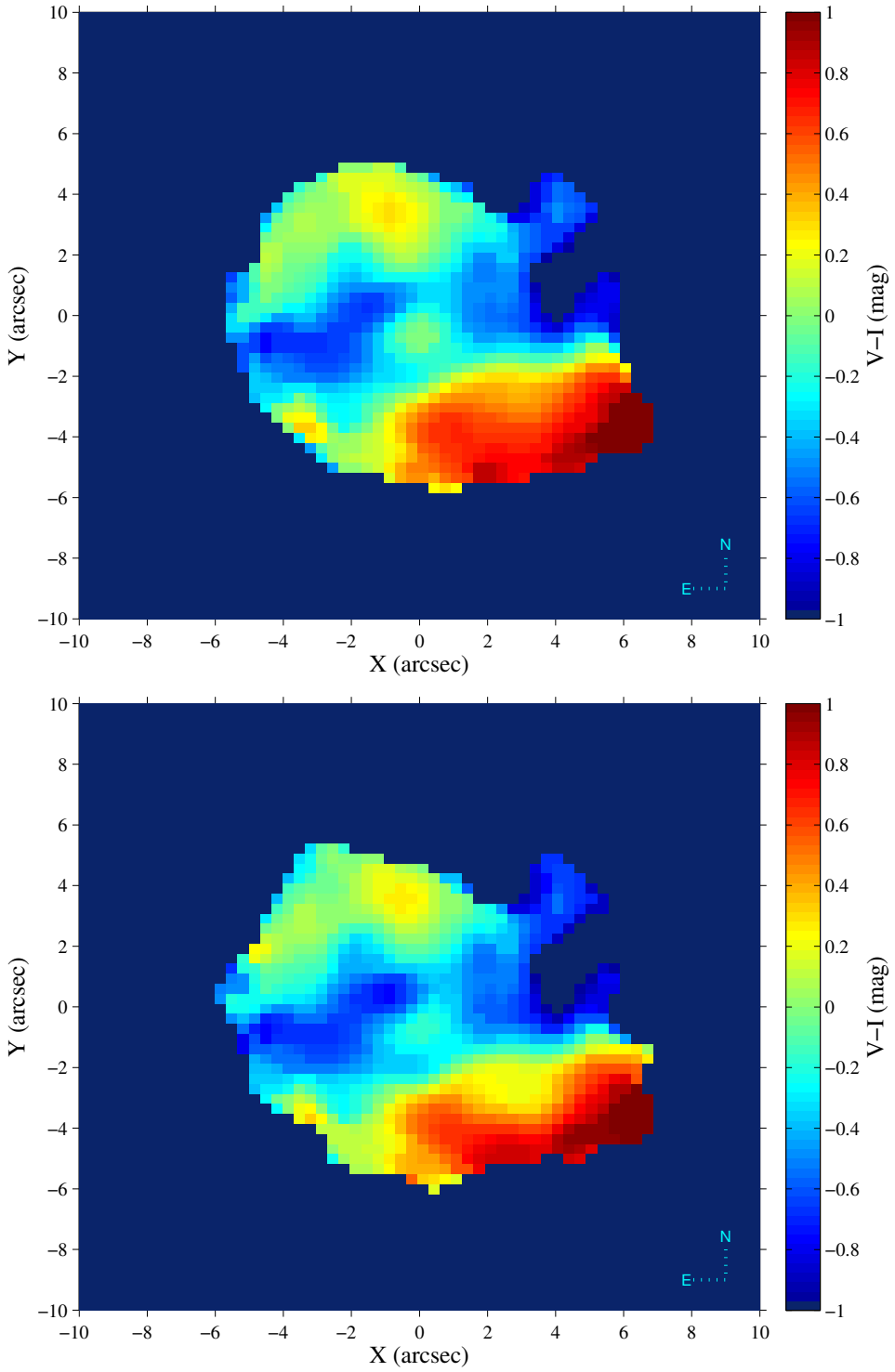

Fig. 28.— V-I magnitude colour map. Top: V-I colour map corrected for the Galactic foreground extinction $A_v = 0.237$ but not for the intrinsic extinction in Tol 1247-232. Bottom: V-I colour map corrected for both the Galactic foreground extinction $A_v = 0.237$ and the intrinsic extinction in Tol 1247-232 using the Calzetti et al. (2000) extinction law for starbursts with $R_V = 4.05$.

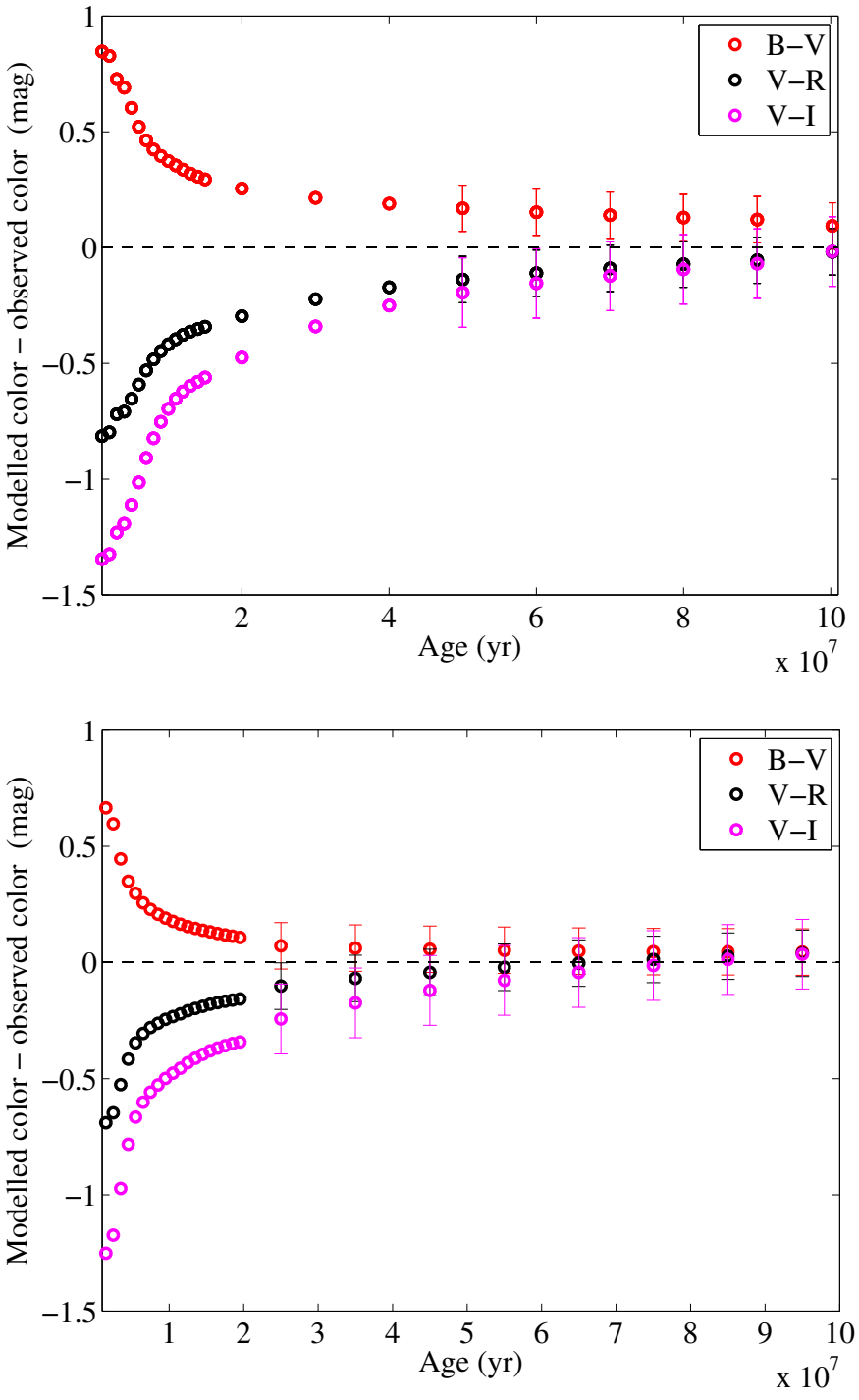

Fig. 29.— Comparison of the observed broad band colours of Tol 1247-232 to spectral synthesis models. The observed colours have been corrected for Galactic extinction and the intrinsic extinction in Tol 1247-232 using our A_V map shown in the bottom panel of Figure 16 and the starburst attenuation law by Calzetti et al. (2000) with $R_V = 4.05$. The top panel shows the differences calculated with the Yggdrasil model based on SB99 spectra and the bottom panel shows the differences calculated with the Yggdrasil model based on Zackrisson et al. (2001) input spectra. The error bars represent the uncertainties in the observed colours.

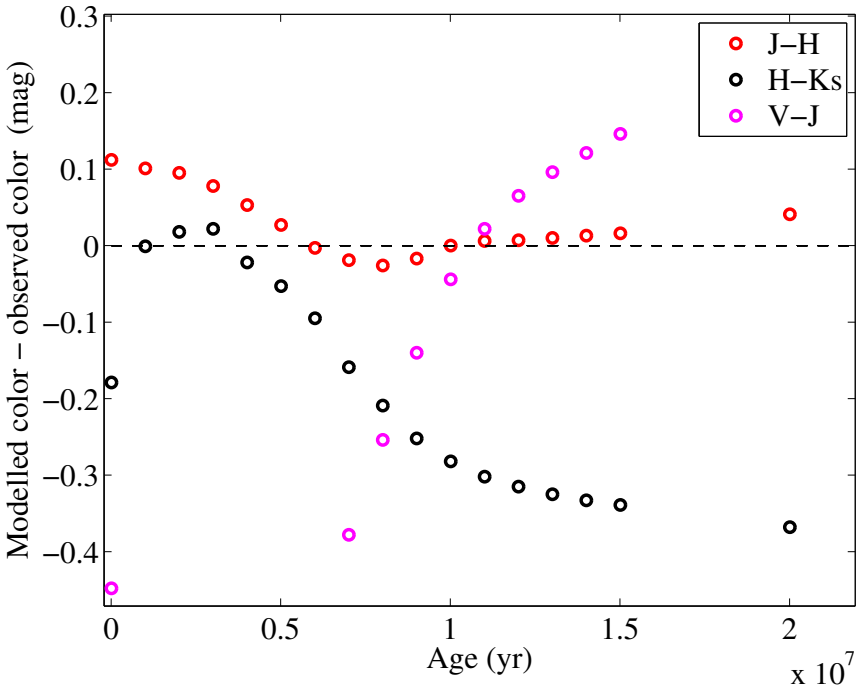

Fig. 30.— Comparison of the observed near infrared colours of Tol 1247-232 to a constant burst spectral synthesis model. The observed colours have been corrected for Galactic extinction and the intrinsic extinction in Tol 1247-232 using our A_V map shown in the bottom panel of Figure 16 and the starburst attenuation law by Calzetti et al. (2000) with $R_V = 4.05$. The Yggdrasil model was used with SB99 input spectra for this calculation. The errors in the colours are approximately 0.1 mag for V-J, 0.2 mag for J-H and 0.2 mag for H-Ks.

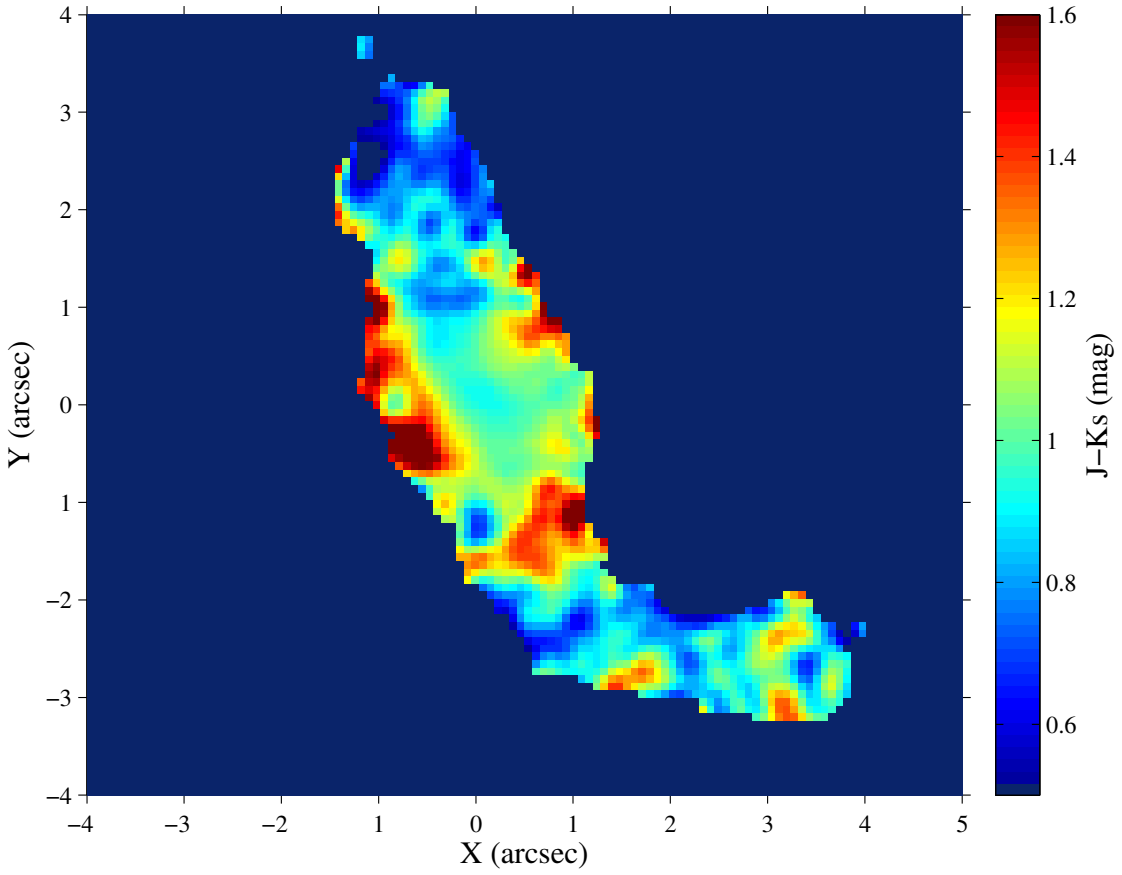

Fig. 31.— Extinction corrected J-H magnitude colour map. The map is corrected for both the Galactic foreground extinction ($A_v = 0.237$) and the intrinsic extinction in Tol 1247-232 using the Calzetti et al. (2000) starburst attenuation law with $R_V = 4.05$.

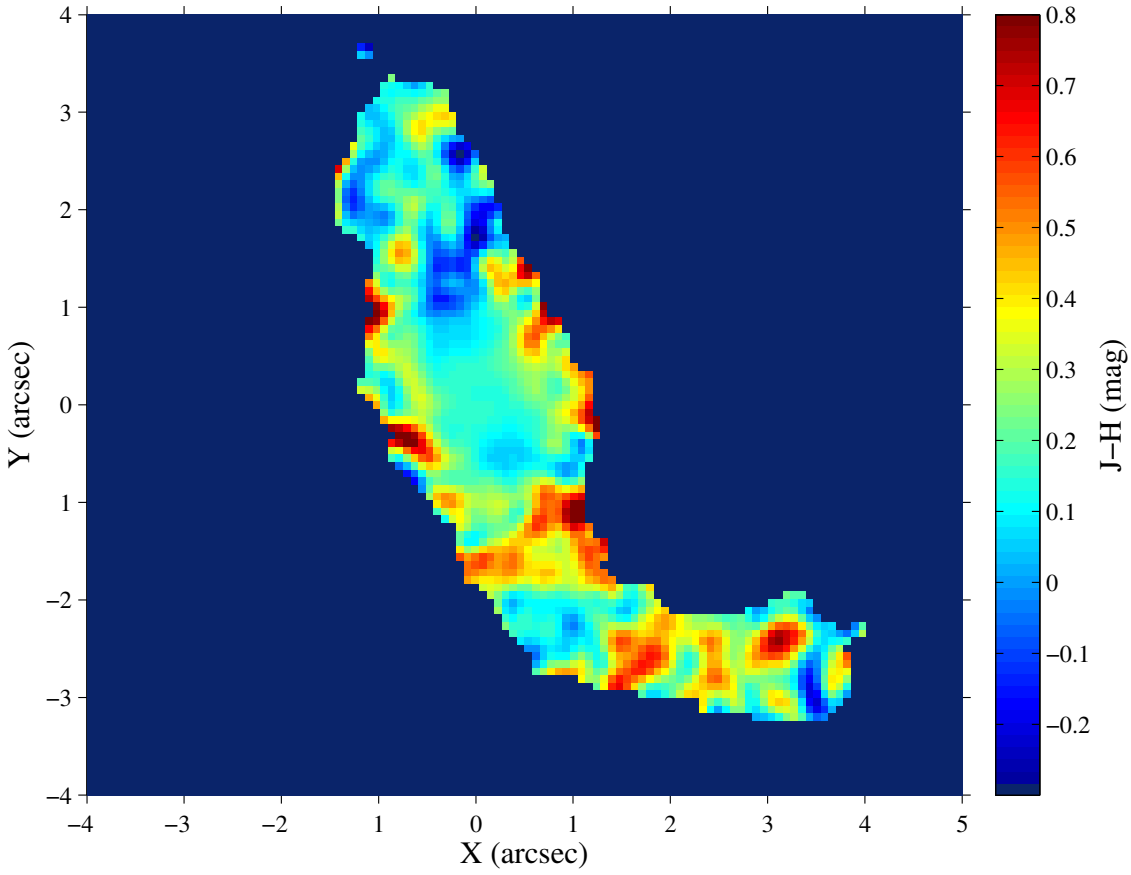

Fig. 32.— Extinction corrected J-Ks magnitude colour map. The map is corrected for both the Galactic foreground extinction ($A_v = 0.237$) and the intrinsic extinction in Tol 1247-232 using the Calzetti et al. (2000) starburst attenuation law with $R_V = 4.05$.

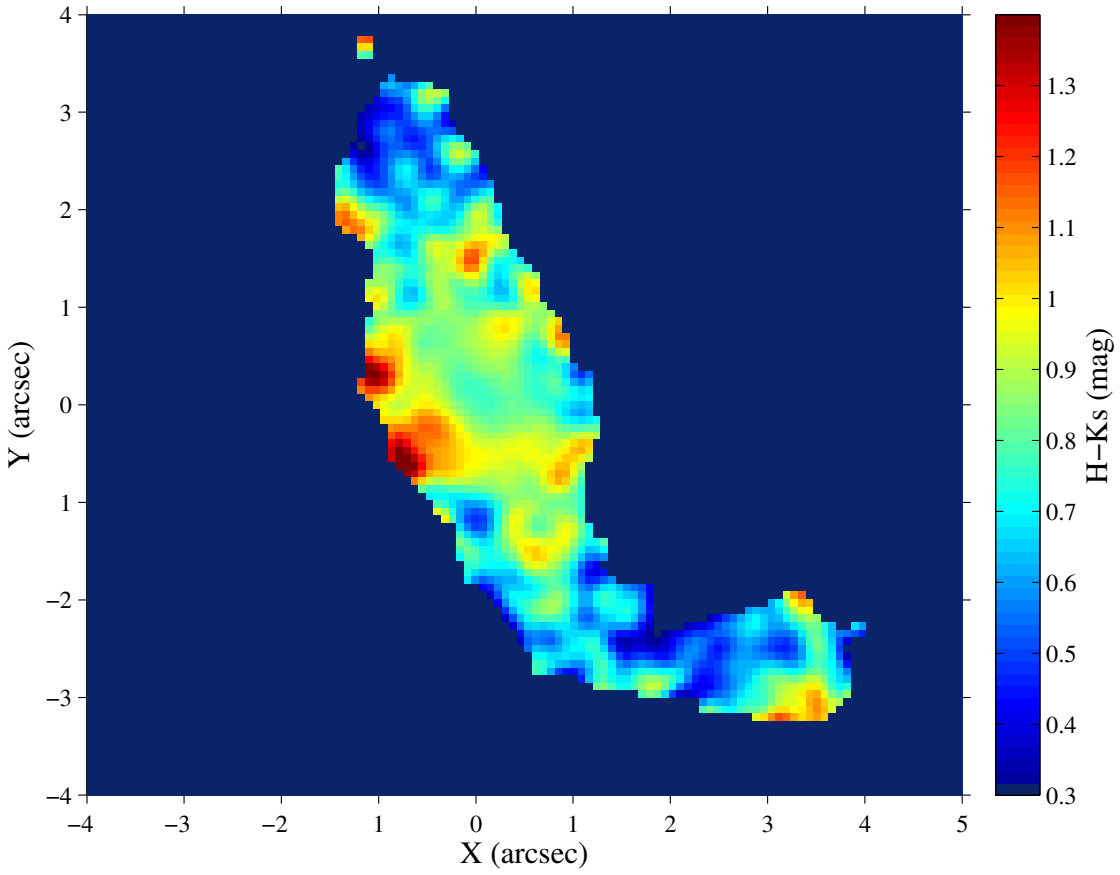

Fig. 33.— Extinction corrected H-Ks magnitude colour map. The map is corrected for both the Galactic foreground extinction ($A_v = 0.237$) and the intrinsic extinction in Tol 1247-232 using the Calzetti et al. (2000) starburst attenuation law with $R_V = 4.05$.

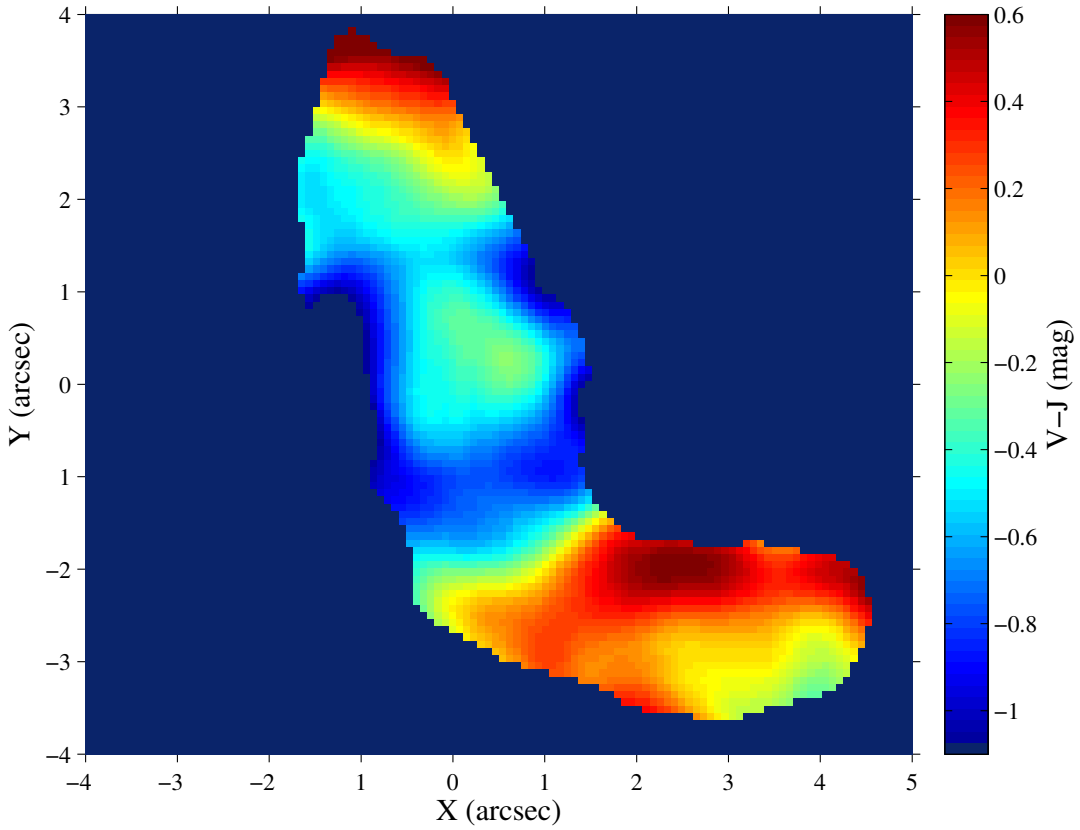

Fig. 34.— Extinction corrected V-J magnitude colour map. The map is corrected for both the Galactic foreground extinction ($A_v = 0.237$) and the intrinsic extinction in Tol 1247-232 using the Calzetti et al. (2000) starburst attenuation law with $R_V = 4.05$.

10. Conclusions

We have obtained a new estimate for the LyC escape fraction in Tol 1247-232, which is $f_{esc}^{LyC} = 4.9 \pm^{1.2}_{1.1}$ %. This estimate is somewhat higher than the escape fraction ($f_{esc}^{LyC} = 2.4 \pm^{0.9}_{0.8}$ %) previously reported by Leitet et al. (2013). Note that, while other detections of LyC leakage exists at $z \sim 3$, this result is still in stark contrast to for example the spectroscopic search for LyC leakers at $z \sim 0.7$ by Bridge et al. (2010), who find no direct detections of LyC leakage in their sample except for in a single starburst/AGN composite galaxy. We have analysed the possibility of an AGN contribution in Tol 1247-232, but find no strong indication of an AGN in either the visual or near infrared. Previous work in the X-ray and radio regimes also fail to show a measurable AGN contribution in the galaxy. Instead we find that the observed properties of Tol 1247-232 are generally in good agreement with the galaxy being a starburst galaxy with a large portion of the young massive stars being Wolf-Rayet stars. Thus, we conclude that Tol 1247-232 is a LyC leaking pure starburst galaxy, provided that the measurement of the leaking LyC photons at $\lambda = 900$ Å by Leitet et al. (2013) is correct.

We further find that the observed colours in both the visual and near infrared regimes indicate that the highest concentration of young and massive stars in Tol 1247-232 are located in the centre of the galaxy. We are unable to show where the LyC leakage is happening, but find that the most likely candidate region would again be the central region of the galaxy.

We have also shown that obtaining a resolved map of the extinction is of some importance when determining the escape fraction in galaxies based on the extinction corrected Hα line. If only an average extinction is used the extinction corrected Hα flux is underestimated by 10% in Tol 1247-232. However, the effect of this underestimate would only translate to approximately a 0.1% difference in the estimated escape fraction, i.e. a shift from 4.9% to 5.0% in f_{esc}^{LyC}. Instead we find that the uncertainty in estimating f_{esc}^{LyC} is dominated by other systematic effects. Most notably we find that dust attenuation of the intrinsically produced LyC photons is very important. However, accounting for the dust attenuation of the LyC photons is difficult, and a proper treatment depends on accurate estimates of the total infrared flux in the galaxy, the Hα line strength and any possible observed Lyα leakage. Note that accurate estimates for these quantities require knowledge about the extinction in the galaxy. In the case of Tol 1247-232 it is difficult to accurately estimate the total infrared flux since we must base our estimate on a single infrared measurement at 60 μm from IRAS. The LyC flux measured by Leitet et al.

(2013) also has a rather large uncertainty. We estimate that the absolute escape fraction is reduced by approximately 50% (from $\approx$ 10% to $\approx$ 5%) when the effect of LyC dust absorption is taken into account. However, the uncertainties, especially in the infrared flux measurement on Tol 1247-232, result in the estimate for the LyC dust absorption fraction being rather uncertain which with the large uncertainty in the leaking LyC flux measurement results in a 15% uncertainty in the escape fraction estimate. Further, we do not know what the proper choice of R_V is for the extinction corrections of the observed emission line fluxes in Tol 1247-232, and we find that if R_V is allowed to vary between $R_V = 2.5$ and $R_V = 4.85$ this results in a further 10% uncertainty in the estimated escape fraction. We also find that we are unable to properly account for the presence of dust in the channels where we assume that the LyC photons are escaping. However, simulations indicate that when measurable LyC leakage is happening, it happens through virtually hydrogen and dust-free channels. Thus, the possible presence of a small amount of dust in the channels should have a minimal effect on the escape fraction compared to the other uncertainties.

We finally conclude that for future estimates of the escape fraction in local galaxies, the first priority should be an accurate measurement of the leaking LyC photon flux, and the second priority should be to obtain proper estimates for the extinction corrected Hα line and the infrared flux of the galaxy to allow both an estimate of the intrinsic LyC photon production and the LyC dust absorption, since these two quantities are closely tied together. For galaxies at higher redshifts where substantial Lyα leakage is expected, accurate measurements of the Lyα flux should also be obtained.

Table 1: Narrow band emission line photometry and infrared flux of Tol 1247-232

Galaxy	Hα	Hβ	[OIII]	Lyα	F_{900}	IRAS 60μm	E_g(B-V)	E_i(B-V)
Apparent	523.3	145.3	723.8	120	1.3	0.507	0.076	0.14
Errors	1%	2%	1%	12.5%		10%	3%	8%
Extinction corrected	977.3	341.1	1651.7	239	4.8			
Errors	15%	15%	15%	12.5%	18%			

Note. — The Hα, Hβ, [OIII] and Lyα fluxes are given in units of 10^{-15} erg s^{-1} cm^{-2}. The LyC flux at 900 Å, F_{900}, based on the measurement by Leitet et al. (2013) is given in units of 10^{-15} erg s^{-1} cm^{-2} Å^{-1} and the IRAS 60 μm infrared flux is given in Jansky. The extinction corrected fluxes are corrected for both the Galactic foreground extinction and the intrinsic extinction. $E_g(B-V)$ is the Galactic foreground colour excess obtained from Schlafly & Finkbeiner (2011) by assuming $R_V = 3.07$ and $E_i(B-V)$ represents the intrinsic average colour excess of Tol 1247-232, again assuming $R_V = 3.07$.

Table 2: Broad band photometry of Tol 1247-232

	B	V	R	I	J	H	K_s
Apparent magnitudes	16.14	15.64	15.73	15.67	15.60	15.28	14.50
Errors (mag)	0.05	0.05	0.05	0.1	0.066	0.102	0.087
Extinction corrected magnitudes	15.34	15.03	15.24	15.29	15.39	15.16	14.43

Note. — Note that since our H, J and Ks images were calibrated against the 2MASS survey, the magnitudes and errors reported here are identical.

Table 3: Integrated colours of Tol 1247-232

	B-V	B-R	B-I	V-R	V-I	R-I	V-J	J-H	H-Ks
Apparent	0.50	0.41	0.48	-0.095	-0.026	0.069	0.04	0.32	0.78
Errors (mag)	0.1	0.1	0.15	0.1	0.15	0.15	0.12	0.17	0.19
Extinction corrected colours	0.31	0.096	0.046	-0.21	-0.26	-0.050	-0.36	0.23	0.72

REFERENCES

Atek, H., Kunth, D., Schaerer, D., et al. 2009, A&A, 506, L1

Baker, J. G. & Menzel, D. H. 1938, ApJ, 88, 52

Baldwin, J. A., Phillips, M. M., & Terlevich, R. 1981, PASP, 93, 5

Bergvall, N., Leitet, E., Zackrisson, E., & Marquart, T. 2013, A&A, 554, A38

Bergvall, N., Zackrisson, E., Andersson, B.-G., et al. 2006, A&A, 448, 513

Bolton, J. S. & Haehnelt, M. G. 2013, MNRAS, 429, 1695

Boutsia, K., Grazian, A., Giallongo, E., et al. 2011, ApJ, 736, 41

Bouwens, R. J., Illingworth, G. D., Oesch, P. A., et al. 2012, ApJ, 752, L5

Bridge, C. R., Teplitz, H. I., Siana, B., et al. 2010, ApJ, 720, 465

Buat, V., Burgarella, D., Deharveng, J., & Kunth, D. 2002, Astron.Astrophys., 393, 33

Bunker, A. J., Wilkins, S., Ellis, R. S., et al. 2010, MNRAS, 409, 855

Calzetti, D., Armus, L., Bohlin, R. C., et al. 2000, ApJ, 533, 682

Calzetti, D., Kinney, A. L., & Storchi-Bergmann, T. 1994, ApJ, 429, 582

Cartledge, S. I. B., Clayton, G. C., Gordon, K. D., et al. 2005, ApJ, 630, 355

Cowie, L. L., Barger, A. J., & Trouille, L. 2009, ApJ, 692, 1476

Deharveng, J.-M., Buat, V., Brun, V. L., et al. 2001, A&A

Finkelstein, S. L., Papovich, C., Ryan, R. E., et al. 2012, ApJ, 758, 93

Finlator, K. 2012, ArXiv e-prints, 1203.4862

Fitzpatrick, E. L. 1999, PASP, 111, 63

Gnedin, N. Y., Kravtsov, A. V., & Chen, H.-W. 2008, ApJ, 672, 765

González Delgado, R. M., Leitherer, C., & Heckman, T. M. 1999, ApJS, 125, 489

Gordon, K. D., Cartledge, S., & Clayton, G. C. 2009, ApJ, 705, 1320

Gordon, K. D., Clayton, G. C., Misselt, K. A., Landolt, A. U., & Wolff, M. J. 2003, ApJ, 594, 279

Grosbøl, P. & Dottori, H. 2012, A&A, 542, A39

Groves, B. A., Heckman, T. M., & Kauffmann, G. 2006, MNRAS, 371, 1559

Hayes, M., Ostlin, G., Atek, H., et al. 2007, MNRAS, 382, 1465

Heckman, T. M., Sembach, K. R., Meurer, G. R., et al. 2001, ApJ, 558, 56

Hirashita, H., Buat, V., & Inoue, A. K. 2003, A&A, 410, 83

Inoue, A. K. 2001, AJ, 122, 1788

Inoue, A. K., Hirashita, H., & Kamaya, H. 2000, PASJ, 52, 539

Inoue, A. K., Hirashita, H., & Kamaya, H. 2001, ApJ, 555, 613

Inoue, A. K. & Iwata, I. 2008, MNRAS, 387, 1681

Iwata, I., Inoue, A. K., Matsuda, Y., et al. 2009, Astrophys.J., 692, 1287

Kreckel, K., Groves, B., Schinnerer, E., et al. 2013, ArXiv e-prints, 1305.2923

Lara-López, M. A., Bongiovanni, A., Cepa, J., et al. 2010, A&A, 519, A31

Leitet, E., Bergvall, N., Hayes, M., Linné, S., & Zackrisson, E. 2013, A&A, 553, A106

Leitet, E., Bergvall, N., Piskunov, N., & Andersson, B.-G. 2011, A&A, 532, A107

Leitherer, C., Schaerer, D., Goldader, J. D., et al. 1999, ApJS, 123, 3

López-Sánchez, Á. R. & Esteban, C. 2008, A&A, 491, 131

Meiksin, A. 2005, MNRAS, 356, 596

Moos, H. W., Cash, W. C., Cowie, L. L., et al. 2000, ApJ, 538, L1

Osterbrock, D. E. 1974, Astrophysics of gaseous nebulae

Osterbrock, D. E. 1989, Astrophysics of gaseous nebulae and active galactic nuclei

Östlin, G., Zackrisson, E., Bergvall, N., & Rönnback, J. 2003, A&A, 408, 887

Pei, Y. C. 1992, ApJ, 395, 130

Petrosian, V., Silk, J., & Field, G. B. 1972, ApJ, 177, L69

Razoumov, A. O. & Sommer-Larsen, J. 2007, ApJ, 668, 674

Robertson, B. E., Ellis, R. S., Dunlop, J. S., McLure, R. J., & Stark, D. P. 2010, Nature, 468, 49

Rosa-González, D., Schmitt, H. R., Terlevich, E., & Terlevich, R. 2007, ApJ, 654, 226

Rosa González, D., Terlevich, E., Jiménez Bailón, E., et al. 2009, MNRAS, 399, 487

Rosa-González, D., Terlevich, E., & Terlevich, R. 2002, MNRAS, 332, 283

Schaerer, D., Contini, T., & Pindao, M. 1999, A&AS, 136, 35

Schlafly, E. F. & Finkbeiner, D. P. 2011, ApJ, 737, 103

Schlegel, D. J., Finkbeiner, D. P., & Davis, M. 1998, ApJ, 500, 525

Shapley, A. E., Steidel, C. C., Pettini, M., Adelberger, K. L., & Erb, D. K. 2006, Astrophys.J., 651, 688

Skrutskie, M. F., Cutri, R. M., Stiening, R., et al. 2006, AJ, 131, 1163

Stasińska, G., Cid Fernandes, R., Mateus, A., Sodré, L., & Asari, N. V. 2006, MNRAS, 371, 972

Strömgren, B. 1939, ApJ, 89, 526

Terlevich, E., Diaz, A. I., Terlevich, R., & Vargas, M. L. G. 1993, MNRAS, 260, 3

Terlevich, R., Melnick, J., Masegosa, J., Moles, M., & Copetti, M. V. F. 1991, A&AS, 91, 285

Tody, D. 1993, in Astronomical Society of the Pacific Conference Series, Vol. 52, Astronomical Data Analysis Software and Systems II, ed. R. J. Hanisch, R. J. V. Brissenden, & J. Barnes, 173

Vacca, W. D., Garmany, C. D., & Shull, J. M. 1996, ApJ, 460, 914

van Dokkum, P. G. 2001, Publ.Astron.Soc.Pac., 113, 1420

Vanzella, E., Siana, B., Cristiani, S., & Nonino, M. 2010, ArXiv e-prints

Warmels, R. H. 1992, in Astronomical Society of the Pacific Conference Series, Vol. 25, Astronomical Data Analysis Software and Systems I, ed. D. M. Worrall, C. Biemesderfer, & J. Barnes, 115

Weingartner, J. C. & Draine, B. T. 2001, ApJ, 548, 296

Weisskopf, V. 1931, Annalen der Physik, 401, 23

Wise, J. H. 2012, ArXiv e-prints, 1201.4820

Yajima, H., Choi, J.-H., & Nagamine, K. 2011, MNRAS, 412, 411

Zackrisson, E., Bergvall, N., Olofsson, K., & Siebert, A. 2001, A&A, 375, 814

Zackrisson, E., Rydberg, C.-E., Schaerer, D., Östlin, G., & Tuli, M. 2011, ApJ, 740, 13

Zahn, O., Reichardt, C. L., Shaw, L., et al. 2011, ArXiv e-prints